Advanced Scanning Probe Lithography and Its Parallelization

A Thesis
Presented to
The Academic Faculty

by

Xi Lu

In Partial Fulfillment
of the Requirements for the Degree
Doctor of Philosophy in the
School of Physics

Georgia Institute of Technology
May 2016

Advanced Scanning Probe Lithography and Its Parallelization

Approved by:

Dr. Elisa Riedo, Advisor
School of Physics
Georgia Institute of Technology

Dr. Dragomir Davidovic
School of Physics
Georgia Institute of Technology

Dr. Phillip N. First
School of Physics
Georgia Institute of Technology

Dr. Karl I. Jacob
School of Materials Science and
Engineering
Georgia Institute of Technology

Dr. Zhigang Jiang
School of Physics
Georgia Institute of Technology

Date Approved: January 13, 2016

To my beloved families.

ACKNOWLEDGEMENTS

Finally, I would like to thank my families. I wish to thank my parents, for being understanding and supportive. I would also give my thanks to my husband, Jian, for his love.

TABLE OF CONTENTS

LIST OF TABLES

LIST OF FIGURES

LIST OF ABBREVIATIONS

EBL	Electron Beam Lithography
AFM	Atomic Force Microscope
KPFM	Kelvin Probe Force Microscope
CSAFM	Current Sensing AFM
SPL	Scanning Probe Lithography
TCNL	Thermochemical Nanolithography
LAO	Local Anodic Oxidation
GNR	Graphene Nanoribbon
GF	Graphene Fluoride
GO	Graphene Oxide
PPV	Polyphenylene Vinylene
NV	Nitrogen-Vacancy
mw	Microwave

SUMMARY

Nanofabrication is the process of making functional structures with arbitrary patterns having nanoscale dimensions. Nanofabrication has been widely implemented in industry for improving microelectronic devices and data storage technology, to increase the component density, to lower the cost and to increase the performance. Other areas of applications include optics, cell biology and biomedicine. One of the most critical challenges in the development of next generation nanoscale devices is the rapid, parallel, precise and robust fabrication of nanostructures. In this thesis work, we demonstrate the possibility to parallelize the thermochemical nanolithography (TCNL) by creating nanoscale patterns with a tip array, containing five identical thermal cantilevers. The versatility of our technique is demonstrated by creating nanopatterns simultaneously on multiple surfaces, including graphene oxide and conjugated polymers. This work also involves the study of the reduction process of graphene fluoride through TCNL and the study of the local anodic oxidation of epitaxial graphene, to create high quality graphene nanoribbons.

CHAPTER 1

INTRODUCTION

1.1 Nanofabrication Methods Overview

Nanotechnology seeks to create and study structures with dimensions in nanometer scale [1]. The properties of such structures often differ from bulk materials. Structural features are used to develop new materials with significantly improved physical, chemical and biological properties. For example, graphene is a zero band gap material. By reducing the width of graphene nanoribbons (GNRs), a band gap could be opened, making graphene a promising material for new generation electronic devices.

Nanofabrication is about creating surface patterns and devices at the nanoscale. As shown in Fig. 1.1, the Moore's law is the prediction that the number of transistors in an integrated circuit has doubled in approximately every two years. This law has held true for almost four decades. However, conventional lithography techniques are reaching their limits. For the purpose of continuous size reducing and cost lowering, nanofabrication has been widely implemented in industry. Besides ultra-high density storage media and electronic devices, nanofabrication can also be used in many other areas, for example, biomedicine, cell biology, sensors and optics.

Two basic approaches of nanofabrication are the 'top-down' and 'bottom-up' approaches. Both approaches provide control of matter at the nanoscale. The former uses lithography methods that are adapted from traditional lithography techniques, but are capable of creating patterns in the sub-100 nm range. The latter involves control of the growth phenomena, for example, the self-assembly processes is used to form two- and three-dimensional nanostructures from molecules or colloidal particles.

1
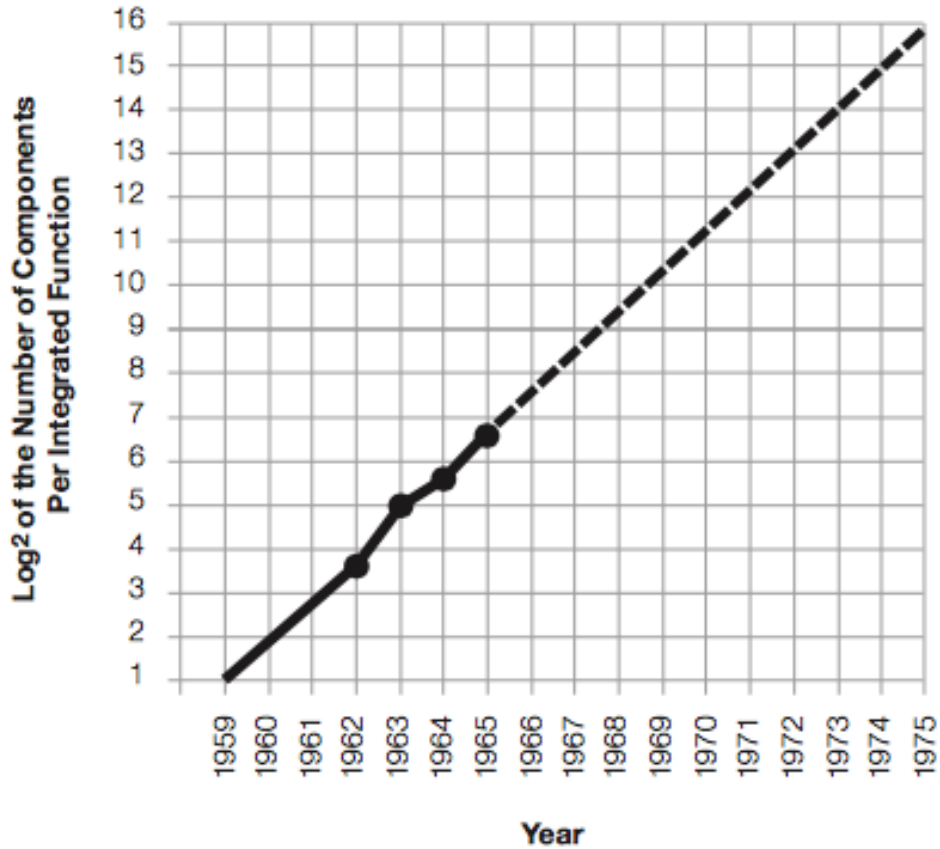
Fig. 1.1: Moore's prediction, in 1965 [2].

The 'top-down' approach includes both serial and parallel techniques. The two conventional 'top-down' techniques are photolithography and electron beam lithography. These methods have been developed to achieve high spatial resolution, but they are limited by either operational capacity or capital cost. These limitations have motivated unconventional methods, including soft lithography, self-assembly, edge lithography and scanning probe lithography. A comparison of these methods is given in Table 1.1.1.

Table 1.1.1: Comparison of different nanofabrication methods.

Fabrication methods	Minimum feature size	Methodology
Photolithography	32 nm [3]	Parallel replication of arbitrary patterns
E-beam lithography	5 nm [4]	Serial processing of arbitrary patterns
Nanoimprint lithography	25 nm [5]	Parallel replication of arbitrary patterns
Self-assembly	10-100 nm [6]	Parallel replication of defied patterns
Edge lithography	Sub-10 nm [7]	Parallel growth of line patterns
Scanning probe lithography	3 nm [8]	Direct writing of arbitrary patterns

1.1.1 Photolithography

Photons have been conventionally applied to pattern silicon wafers. The photolithography systems use a template, or mask, which is typically made by electron beam lithography. To create desired features in the wafer, the system shines ultraviolet (UV) light through the mask. Light pattern of the mask is focused and reduced in size, and projected to the wafer, which is covered with a thin layer of light-sensitive resist by spin coating. The resist's molecular structure changes after exposure to light. A variety of compounds and gases are used to etch away either the altered or unaltered resist, together with the uppermost layer of the substrate, and thus the mask pattern is transferred to the wafer. Photolithography can pattern 32-nm half pitch devices, using 193-nm wavelength UV light [3]. To further reduce the size limit, the wavelength needs to be shorter. The problem is that conventional quartz lenses absorb rather than refract light at wavelengths shorter than 193 nm. Extreme ultraviolet (EUV) systems uses EUV light with a wavelength of 13 nm, and relies on reflector mirrors rather than lenses to focus the light. However, the EUV mirrors, typically made with coatings of silicon and molybdenum,

have low reflection efficiency, and the low efficiency means long, costly exposure times to pattern wafers.

1.1.2 Electron Beam Lithography

Electron beam lithography (EBL) is a direct writing process and can achieve a higher resolution than photolithography, but its mask-less feature also means low throughput. The EBL uses a focused beam of electrons to create patterns on a surface covered with an electron-sensitive resist. Similar to photolithography, the solubility of the resist is changed after exposure to electrons, enabling selective removal of the exposed or unexposed part of the resist. Small structures are created and can be transferred to the substrate, often by the lift-off or etching.

The smallest achievable size by EBL is 5 nm [4], using pure IsoPropylic Alcohol (IPA) development [4]. Further reducing the resolution depends on the optimization of the development process and the reduction of electron beam width. The drawback of reducing the beam width is that it requires a longer reaction time to achieve the same imaging dose. Moreover, the reduction of beam width requires higher energy electrons, but electron scattering effect increases as the electron energy increases, which would affect the resolution inversely.

1.1.3 Soft Lithography

Soft lithography refers to a family of lithography techniques, using elastomer (usually polydimethylsiloxane) stamps, molds or mask to fabricate or transfer structures. Theses techniques include replica molding [9], microcontact printing [10], micromolding in capillaries [11], microtransfer molding [12], nanoimprint lithography [13] and solvent-assisted micromolding [14]. The advantage of soft lithography over conventional

photolithography and e-beam lithography is the ability to work with nonplanar substrates for large-scale patterning. It's a nonconventional lithography technique that can fabricate sub-100 nm features with relatively high throughput and low cost.

Soft lithography can fabricate single-layer structures for the study of cells. It can also fabricate micro electro mechanical systems (MEMS) and applied optical devices. Minimum feature size of 25 nm can be fabricated by nanoimprint lithography [5]. During soft lithography, the resist is usually deformed into the shape of the molds, replicating the nanopatterns of the molds. The resolution of soft lithography is not limited by the effect of light diffraction or resist interference. However, soft lithography depends on a high-resolution master, which is fabricated by conventional nanofabrication techniques. Surface sticking problem and distortion of the features within the stamps need to be improved to reach a lower resolution.

1.1.4 Self-Assembly Nanofabrication

Self-assembly nanofabrication is a bottom-up approach. It creates two or three-dimensional nanostructures by cooperative interactions of building components. The components are not limited to atoms and molecules, but span a wide range of nano- and microscopic structures. For example, lock and key colloidal particles can produce self-assembling structures by controlling the depletion interaction. Thin films of incompatible block copolymers self assemble into 10-100 nm supermolecular structures through microphase separation process [15]. Self-assembly process can create well-defined and stable nanostructures, but it's unable to produce structures with precise spatial position. It also lacks the ability to produce arbitrary patterns.

1.1.5 Edge Lithography

Edge lithography has attracted an increased interest in the past few years [15,16]. It's a nanofabrication method that either grows nanostructures directed by the edge of a feature or transfers the edge of a pattern into the substrate to form nanostructures. In both cases the edges of the original pattern define the features of the final pattern. Edge lithography is capable to create zero-, one- and two- dimensional nanostructures such as nanowells, nanowires and crossing nanowires [17]. There are four main strategies of edge lithography, step-edge decoration, fabrication of self-assembled monolayers (SAMs) [18], two-step process of undercutting and etching [19] and exposure of photoresist to light through an elastromeric phase mask in the near optical field [20].

Step-edge decoration is to deposit metal or other material (for example CaF_2) at step edges of a single crystal surface [15, 21]. This method can create nanowires with varied width and spacing with sub-10 nm feature size [7]. SAMs are the structures widely used for producing organic films with selected surface properties [22]. Disorders in SAMs grown at step-edges allow the selective functionalization in these regions. The third strategy, the two-step process, is to first to deposit a metal layer over the substrate and pattern the metal layer through photolithography or soft lithography, and then through an isotropic etching and subsequent deposition of a second layer of metal, trench patterns are formed at the edges of the original metal patterns. The following lift-off process produces a metal mask that is used to define nanostructures in the substrate. This process can generate patterns down to size 50 nm. The last strategy uses an elastromeric phase mask that is in conformal contact with the photoresist to create nanostructures at the phase edge. This strategy can produce patterns of photoresist with features as small as 90 nm in about

1 second. Edge lithography can create nanostructures in parallel with a fast fabrication speed, however, its dependence on topographical edge surfaces limits the variably of pattern structures.

1.2 Scanning Probe Nanolithography

Scanning probe nanolithography (SPL) is a collection of nanolithography techniques that pattern nanostructures with a scanning probe. It's a high-resolution lithography technique developed after the invention of scanning tunneling microscope (STM) [23] and atomic force microscope (AFM) [24] in the 1980s. Since their invention, these scanning probe microscopes (SPM) are used to directly image the surface morphology and extend the resolution limit to molecules and atoms, which is a great enhancement to conventional optical microscopes.

The advantages of SPMs are (a) it can be used in ambient conditions with a simple set-up; (b) SPMs are capable of high-resolution imaging; (c) SPMs can be used with a wide range of samples. As the needs to reduce lithography pattern size continue increasing, these advantages of SPMs made them promising candidates for low cost nanolithography. Since late 1980s, many SPM based lithography techniques are reported, including both top-down and bottom-up approaches, for example, scanning electron nanolithography [25], local anodic oxidation lithography [26-28], mechanical nanolithography [29] and dip-pen nanolithography [30-36]. SPL is capable to create arbitrary nanostructures with a minimum feature size of 3 nm [8], for applications in high-density data storage, integrated circuits, single electron devices and biochips. SPL is not limited to serial writing applications. With the parallelization of the lithography process by using multi-probe arrays, mass production could be achieved via SPL.

7

1.2.1 Low Energy Electron Beam Nanolithography

The first scanning probe patterning experiment was the scanning electron beam lithography, in the late 1980s [25]. By emitting low energy electrons from the tip of a STM probe, high resolution patterns were created on a electron sensitive surface, placed in separation of a few nanometers from the tip. The sharp tip eliminates the electron beam width, while low energy reduces electron scattering effect. Patterns with 20 nm line widths are produced using STM probe lithography [29].

1.2.2 Local Anodic Oxidation Lithography

Local anodic oxidation (LAO) lithography is another scanning probe nanofabrication method. LAO lithography uses a biased conductive scanning probe to locally modify the surface chemistry through anodic oxidation. STMs and AFMs allow precise control over the movement of the probe, while applying a negative bias from the probe tip to the sample. The applied bias supplies efficient energy to disassociate water molecules in ambient condition, and the sample get oxidized as an anode. Varying the applied bias and ambient humidity controls the pattern linewidth. LAO lithography has been successfully applied to various samples including silicon [26], graphene [27] and metal films [28]. LAO lithography is a one step process for the fabrication of arbitrary patterns.

1.2.3 Mechanical Nanolithography

Mechanical nanolithography, also known as nanomechanical machining or nanomechanical plowing, is a nanofabrication method that uses scanning probes to machine with nanometer precision [29]. During mechanical nanolithography, an AFM tip scratches the sample surface while a suitable normal load is applied. Structures are

formed due to plastic deformations and/or wear of the substrate. The scratching speed, the scratching feed and the load control the depths of the grooves within the structures. Mechanical nanolithography can be applied to a wide range of substrates, including polymers [38, 39], metals [40], semiconductors [41] and insulators [8]. A variety of pattern structures can be fabricated, including concave/convex patterns, nanodots and nanolines.

Mechanical nanolithography has potential applications in manufacturing nanoscale lens arrays, nanogratings and nanomolds. Patterns with a linewidth down to 3 nm were fabricated on an atomically flat mica surface through mechanical nanolithography [8]. Mechanical nanolithography can produce high resolution patterns with relatively simple operations. However, wear of the substrate can cause tip contaminations and deformations, which limit the application of mechanical nanolithography for reliable productions. If wear occurs, debris will be generated and will affect the quality of the devices. Using a diamond or diamond-coated tip can help reduce the tip contaminations, since such tips have a greater hardness than tips made with other materials.

1.2.4 Dip-Pen Nanolithography and Its Parallelization

Dip-pen nanolithography (DPN) is a direct writing method, in which an AFM tip is used to write arbitrary patterns on the substrate in a manner analogous to that of a dip pen [30]. The schematic of DPN is shown in Fig. 1.2. During DPN, molecules are transferred from an AFM tip to a solid substrate of interest through capillary transport. The advantage of DPN over other nanolithography techniques is the capability to selectively place different types of molecules to the same site of a nanostructure, allowing the selective modification of the chemical functionality of the surface in nanoscale.

9
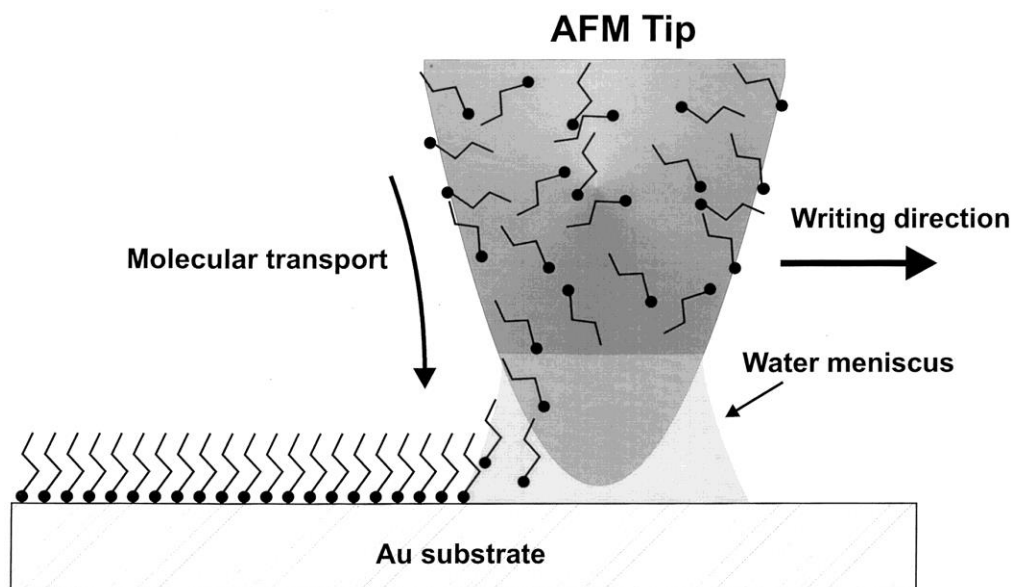
Fig. 1.2: Schematic of DPN. Water meniscus forms at the tip-sample interface. The lithography resolution is limited by the size of the meniscus, which is controlled by humidity [30].

DPN is a versatile technique and can be applied to a wide range of molecular inks, including proteins [32], DNA [33], metal salts [34] and colloidal particles [35]. Various substrates, including metal, insulator and semiconductor thin films [31], can be chosen to be the 'paper'. Alkanethiol patterns with a 15-nanometer linewidth resolution were written on a gold thin film [36]. The patterning speed of DPN is limited by the capillary transport rate, which is determined by the size of water meniscus between the tip and the substrate. The serial feature of DPN also limits its throughput.

To extend DPN's application to mass production, the parallelization of DPN has been developed. A high-throughput parallel DPN system has been reported, and it is composed of eight pens for patterning [42]. Since the linewidth and patterning speed are

10

independent of the normal force applied to the tips, only one of the eight tips has feedback on it to control the patterning position. Eight nanostructures (with a 40-nanometer linewidth resolution) were created simultaneously with a 1-octadecanethiol (ODT) coated cantilever array. The number of pens is not limited to eight. A linear array of 32 pens was able to pattern in parallel, with a 60-nanometer linewidth resolution using SAM as the ink [43]. In the future, it can be increased to hundreds and even thousands of pens for large-scale nanofabrication.

1.3 Thermal Probes and High-Density Data Storage

Scanning thermal microscopy is a noncontact surface profiling technique, using a thermal probe that can function as both heater and thermometer [44]. The thermal probe usually consists of a thermocouple sensor and a heater. For thermal probes with resistively heated tips, the tip area get heated when current flow through the probes, up to over 1000 Celsius. Surface profile can be obtained by scanning the heated thermal probe above but close to the sample surface. The heat conduction in the air between the tip and the sample is sensitive to the tip to sample distance, and the change in the heat conduction is monitored while scanning. Scanning thermal microscopy provides heat-related information such as surface temperature and thermal conductivity. This information is essential for the study of charge transport in silicon devices and thermal transport in optoelectronic devices. Scanning thermal microscopy is also used for biological cell profiling and the surface characterization of materials.

There are several different ways for the fabrication of thermal probes. The first kind of thermal probes consist dissimilar inner and outer conductors, separated by an insulator layer in all areas except the end of the tip. A thermocouple junction is thus formed at the

end of the tip. The junction produces a temperature-dependent voltage, which is detectable at the other end of the probe via the conductors. This kind of thermal probes can detect temperature changes in less than 0.1 millidegree [44]. Another kind of thermal probe is the bolometer-type thermal probe [45], which uses an embedded thin film metal resistor as the temperature sensor. The bolometer-type thermal probe consists two layers of polyimide with the metal resistor film sandwiched in-between. The metal resistor has a temperature coefficient resistance of 2963 ppm/K. The resistor is thin at the tip area and thick at other areas. During the scan, a current passes through the resistor and causes joule heating at the tip. The resistance, which contains the information of local thermal conductivity of the sample surface, is monitored and used to construct the scanned image. The third type of thermal cantilever is made by embedding resistive heater into micro-machined silicon cantilever, which can be heated up to 1000 Celsius [46]. Those silicon thermal probes can be applied to thermal-mechanical nanolithography and have been used to write different shaped pits on polymer substrates such as polycarbonate and polymethyl methacrylate (PMMA).

1.3.1 Thermal-Mechanical Nanolithography

In 1992, heated AFM probes have been used to perform thermal-mechanical writing of polymer surfaces for high-density data storage applications [47]. An infrared laser is focused on an AFM tip while the tip is in contact with the PMMA substrate. The tip, which is heated by the laser beam, softens the PMMA in the contact region with the tip. The heated tip applies pressure to the softened PMMA and creates a pit. Pits sizes ranged from several hundred angstroms to one micrometer were created, with a writing speed of at least 100 kHz. The applied pressure, the laser power and the width of the laser pulse

control the size of the pits. The difficulty to align the external laser is the main drawback of laser-heated cantilevers.

To replace laser heated cantilevers, resistively heated thermal cantilevers and soft cantilevers with integrated piezoresistive sensors are used to write and read data marks respectively. The ultimate goal is to write and read without a laser. The writing cantilevers are made with sharp tips with a tip radius below 300 A. The sharp tips help to reduce the dimension of the data marks while writing. When heated tips are in contact with the substrate, the heat softens the substrate in the contact area. Elastic deformation occurs when the sharp tip presses into the softened surface. Separate cantilevers with integrated piezoresistive sensors are used for data reading. As the reading cantilever scans over the stored data marks, a current passes through the piezoresistive sensor and senses the surface topography. Thin cantilevers with a thickness of 1 um are used for the reading. Thin cantilevers are preferable because they are softer than thick cantilevers, thus the tip wear and sample contaminations are reduced during data reading. The reading speed is up to 120 mm/s [48].

1.3.2 Parallel Thermal-Mechanical Nanolithography

The serial nature of SPL technologies is the fundamental limit of the throughput and rate, thus rendering them less suitable for high density data storage applications than the parallel processes. By introducing the probe arrays, parallel patterning can be achieved with SPL. The probe arrays are made with multiple probes that write multiple patterns simultaneously. The first type of the probe array is fabricated by integrating thermal-mechanical AFM cantilevers into a two dimensional chip [49]. The integrated cantilevers are identical and have read/write storage functionality. The parallel operation of the AFM

cantilever array offers an efficient way for data reading and recording. In 2002, arrays made with 32 x 32 heated AFM cantilevers were fabricated for the IBM's Millipede storage approach [49]. The millipede concept is shown in Fig. 1.3 (a). The arrays were used to create nanometer-sized bit indentations into polymer surfaces. Two years later, 64 x 64 cantilevers were integrated into the array [50], as shown in Fig. 1.3 (b). This newly designed array can perform both recording and reading at 840 Gb/in^2 [51].

The probe-based data storage using thermal cantilever arrays is a new approach for storing data at high density and speed. This technique is completely different from other storage methods such as magnetic hard disks, optical disks and memory chips. The probe-based data storage technique is a promising approach to ultrahigh density data recording.

(a)

(b)
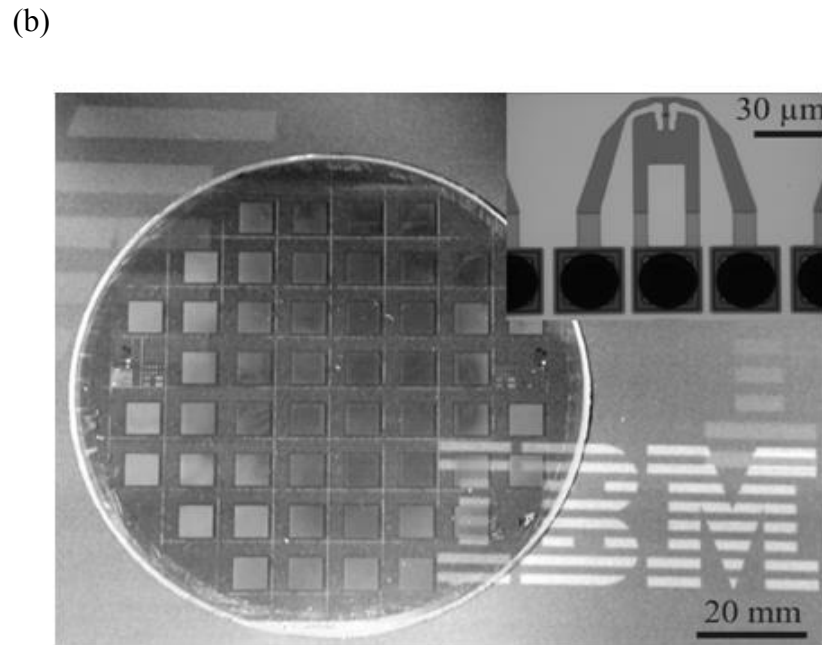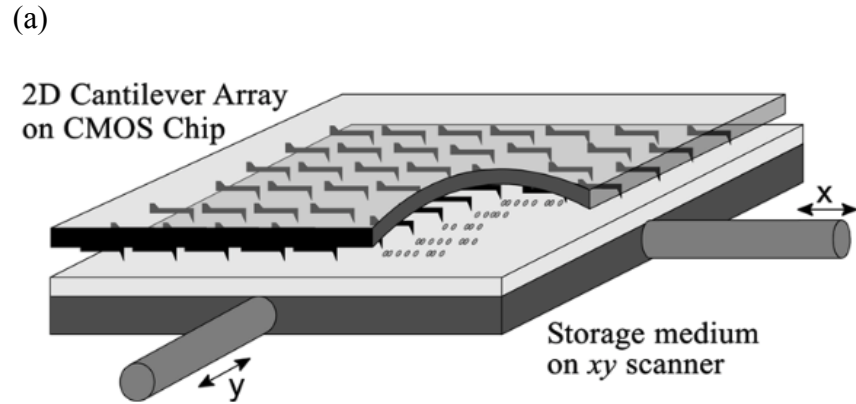
Fig. 1.3: Millipede cantilever array. (a) The millipede concept. (b) Glass wafer of cantilever arrays. Each square contains 4096 cantilevers. The inset shows the cantilever structure bonded on the glass wafer [49, 50].

1.4 Fabrication Methods of Graphene Nanoribbons (GNRs)

GNRs would be the essential components for graphene based electronic devices. Multiple methods are reported to fabricate GNRs such as electron beam lithography [52], fabrication of GNRs using a nanowire etch mask [53], sonication of exfoliated graphene [54] and unzipping of graphene nanotubes [55]. These methods can be used for generating narrow GNRs, however, each method has one or more drawbacks such as low yield, rough edges, contamination and difficulty to produce long ribbons.

1.4.1 Electron Beam Lithography

Graphene ribbons can be fabricated from exfoliated graphene on SiO_2/Si substrate. Negative tone e-beam resist, hydrogen silsesquioxane (HSQ), is spin-coated onto graphene samples and patterned to form an etch mask defining nanoribbons. Unprotected graphene is etched away by oxygen plasma, leaving the GNRs covered by HSQ patterns (Fig. 1.4, left, a). This method is reported to produce GNRs with widths ranging from 10-100 nm and lengths of 1-2 um [52]. SEM images of GNR devices with uniform length and varying width is shown in Fig. 1.4 (left, b), and devices of uniform width and varying length is shown in Fig. 1.4 (left, c). Difficulties of removing the resist and rough edges are the main drawbacks of this method. GNRs obtained from the e-beam lithography approach usually have a line edge roughness of 1-3 nm, which can adversely impact their electronic properties.

1.4.2 Nanowire Etch Mask Method

Smooth-edged nanowires with sub-5 nm sizes can be obtained using various chemical approaches [56, 57]. These nanowires can be used as a physical mask to protect underlying graphene from oxygen plasma etching, and GNRs with widths from 6 to 30

nm can be obtained. Silicon nanowires used as the mask are grown by the Au nanocluster mediated vapor-liquid-solid growth approach. To introduce capillary force between the nanowires and graphene sheets for a close contact, graphene flake samples are dipped into isopropyl alcohol (IPA) and blow dried with nitrogen. After locating the nanowires with an AFM, oxygen plasma is used to selectively etch away the unprotected graphene. The nanowires can be removed by a brief sonication, leaving the GNRs exposed. The widths of the resulting GNRs are mainly determined by mask width (nanowire diameter) so that GNRs with variable widths down to the sub-10 nm regime can be obtained using different diameter nanowire etching masks. However, this method does not provide robust means to place GNRs with precision.

1.4.3 Chemically Derived GNRs by Sonication

By using a commercially available graphite material (Grafguard 160-50N, Graftech Incorporated, Cleveland, OH), GNRs can be chemically derived by sonication. The graphite is exfoliated by brief (60 s) heating to 1000 °C in forming gas (3% hydrogen in argon). The resulting exfoliated graphite was dispersed in a 1,2-dichloroethane (DCE) solution of poly(m-phenylenevinylene-co-2,5-dioctoxy-p-phenylenevinylene) (PmPV) and a homogeneous suspension was formed after sonication for 30 minutes. Large pieces of materials can be removed from the supernatant by centrifugation. The left supernatant can be deposited on substrates and numerous GNRs are observed by AFM. The GNRs shown smooth edges, and ribbons with widths below 10 nanometers were produced. However, this method has its drawbacks due the lack of an efficient way to separate single layered GNRs and multiple layered GNRs and difficulties for the size control.

1.4.4 Unzipping of Graphene Nanotubes

Oxidized graphene nanoribbons can be produced by an oxidative process that cuts and unravels graphene nanotubes [55], similar to 'unzipping'. The ribbons are prepared by suspending multiwalled carbon nanotubes in concentrated sulphuric acid followed by treatment with 500 wt% $KMnO_4$ for 1 h at room temperature (22 °C) and 1 h at 55–70 °C. The opening of the nanotubes are observed to occur along a line, providing straight-edged nanoribbons. Subsequent chemical reduction of the nanoribbons restores the electrical conductivity. This process and resulting nanoribbons are shown in Fig. 1.4, right. The advantage of this method is that it has a nearly 100% yield of nanoribbon structures. The same unzipping process also applies to single-walled carbon nanotubes (SWCNTs), but the entanglement of GNRs from SWCNTs makes it difficult to produce narrow ribbons. Another drawback of this method is the lack of precise control of the nanoribbon width and length.
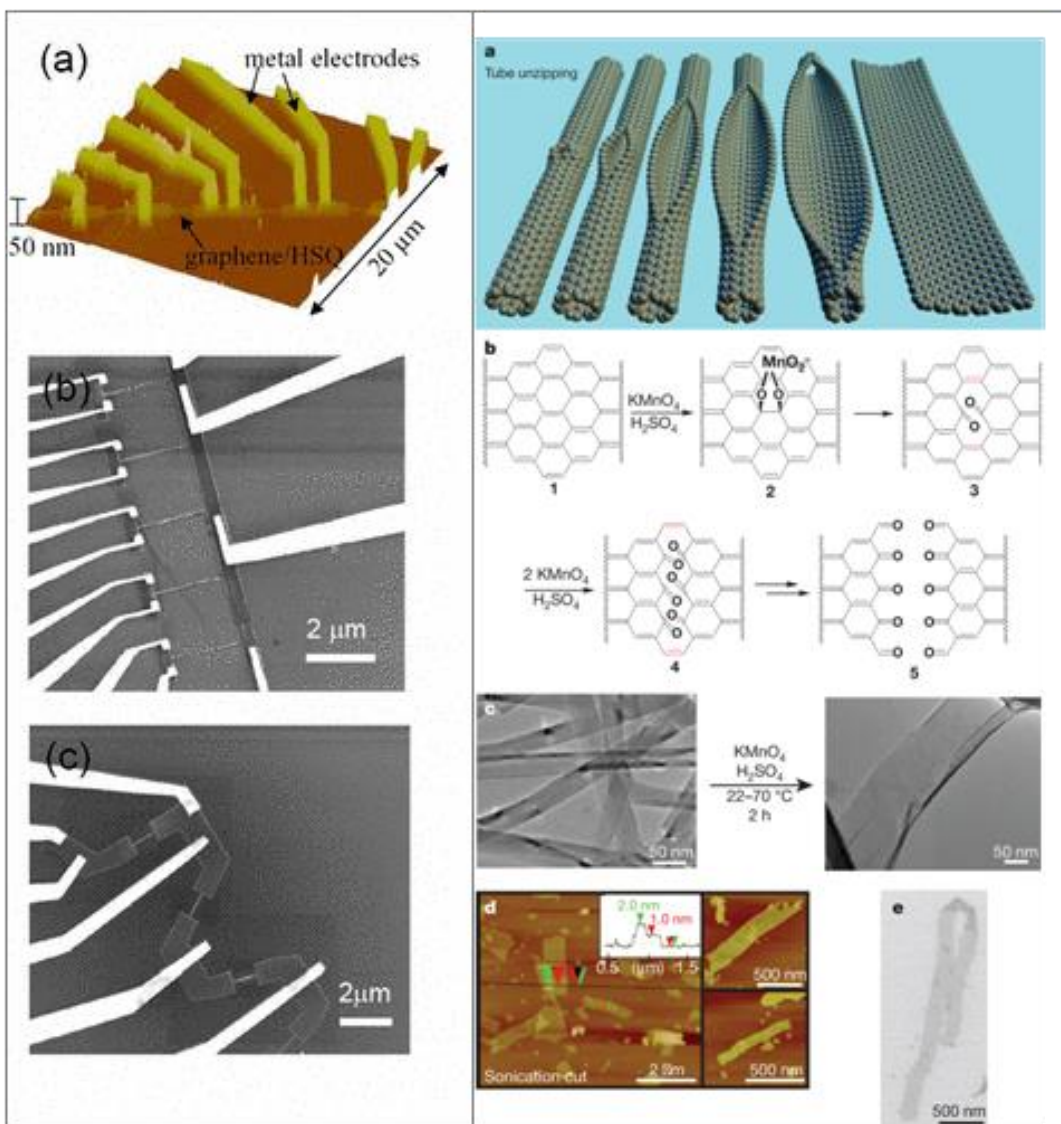
Fig. 1.4: GNRs created by EBL (left) and unzipping of GNTs (right). Left, (a) AFM image of GNRs covered by a protective HSQ etch mask. (b) and (c) are GNRs with varying width and length [52]. Right, (a), representation of the gradual unzipping of one wall of a carbon nanotube to form a nanoribbon. Oxygenated sites are not shown. (b), the proposed chemical mechanism of nanotube unzipping. (c), TEM images depicting the transformation of MWCNTs to oxidized nanoribbons. (d), AFM images of partly stacked multiple short fragment of nanoribbons. (e), SEM image of a folded nanoribbon on a silicon surface [55].

CHAPTER 2

MATERIALS AND CHARACTERIZATIONS

2.1 Materials

2.1.1 Graphene

Carbon is the basic element of all organic chemistry and forms a large variety of compounds. As a result of the flexibility of its bonding, carbon has many allotropes of which the best known are diamond and graphite, which are three-dimensional carbon allotropes. Fullerenes are zero-dimensional allotropes of carbon discovered in 1985 [57]. They are spherical molecules composed entirely of carbon. Carbon nanotubes, one-dimensional allotropes of carbon, are carbon atoms in cylindrical structures. These carbon allotropes are different in structures and physical properties. Graphene, a two-dimensional (2D) allotrope of carbon, is carbon atoms arranged on honeycomb structure, one atom thin, and it can be viewed as a single layer of graphite. Graphite can be viewed as a stack of graphene by van der Waals force. Although graphite is widely used in pencils, graphene is isolated in 2004 [58, 59], 440 years after the invention of pencils. This relatively late discovery of graphene is due to the assumptions that single layer graphene does not exist in the free space and the lack of a method to separate graphene from graphite debris.

Graphene attracts great attention for its remarkable material properties and the candidacy for the next generation electronics [58, 60-62]. The electron mobility in single layer graphene is above 200,000 $cm^2v^{-1}s^{-1}$, which is significantly higher than semiconductors that are widely used. Therefore, graphene is a desirable material for high speed applications. For the size reduction purpose, graphene nanoribbons (GNRs) would

20

be the ideal building blocks for all carbon devices [62]. However, the property that graphene is a zero band gap material and remains highly conductive even at the charge neutrality point, makes it unsuitable for traditional semiconductor applications. The difficulty to manufacture graphene nanoribbons with smooth edges also limits the performance of graphene based devices. By chemically modifying graphene, a band gap can be opened. These methods include oxidation using modified Hummers method [63], adding organic functional group to the graphene lattice [64] and fluorination by exposing graphene to xenon difluoride (XeF_2) gas [65]. The oxidized or fluorinated graphene can be reduced while heated. With Thermochemical Nanolithography (TCNL), arbitrary patterns of reduced graphene can be created on insulating surfaces, without affecting the structure of carbon lattice.

Three common methods are used for the preparation of graphene samples in the literature, including exfoliation, chemical vapor deposition and epitaxial growth of graphene. Exfoliated graphene can be prepared by mechanical exfoliation of graphite using adhesive tape. The exfoliation method is also used to prepare other 2D materials, such as hexagonal boron nitride and molybdenum disulfide. Graphene prepared by exfoliation has shown ultrahigh mobility (above 200,000 $cm^2v^{-1}s^{-1}$). However, the size of exfoliated graphene can hardly excess 100 um, which limits its application for electronic devices.

Chemical vapor deposition method can produce relatively large area of graphene samples. Ni and Cu are common substrates for CVD graphene. During the CVD process, the substrate is first annealed in hydrogen atmosphere and then a mixture of H_2/CH_4 is introduced into the system. Graphene layers form on the substrate until the system is

21

cooled down. The advantage of CVD graphene is that it can be transferred to other substrate after the deposition, such as SiO_2/Si substrate and glass substrate. However, the domain gain boundaries in CVD graphene make electron mobility limited to around 2000 $cm^2v^{-1}s^{-1}$.

It has been known since 1975 that graphite layers form on SiC substrate by heat treatment at about 1000 °C [66]. Epitaxial graphene (EG) layers form as a result of sublimation of Si from SiC substrate. Recent experiment results showed that EG has similar electronic properties to isolated graphene. The electron mobility of EG is comparable to that of exfoliated graphene. SiC wafers are commercially available, which makes large scale production of EG possible.

EG is used in the study of anodic oxidation. EG is grown and provided by Prof. de Heer's group (Georgia Institute of Technology). The details of its synthesis and characterization can be found in the literature [56]. Raman spectroscopy measurement was taken to characterize the EG sample using a confocal Raman system (see Section). Figure 2.1 shows the Raman spectrum of EG grown on SiC, using a 532 nm wavelength excitation laser. The Raman spectrum shows two main graphene bands, the G band at ~1580 cm^{-1} and the 2D band at ~2580 cm^{-1}. A third band appears at ~1325 cm^{-1} is the D band, and is used to identify defects. The D band is very small in this case, indicating low defect densities in the sample. The Raman spectrum of the substrate, SiC, is superimposed on the spectrum of graphene, with a strong intensity in the range from 1500 cm^{-1} to 2000 cm^{-1}.
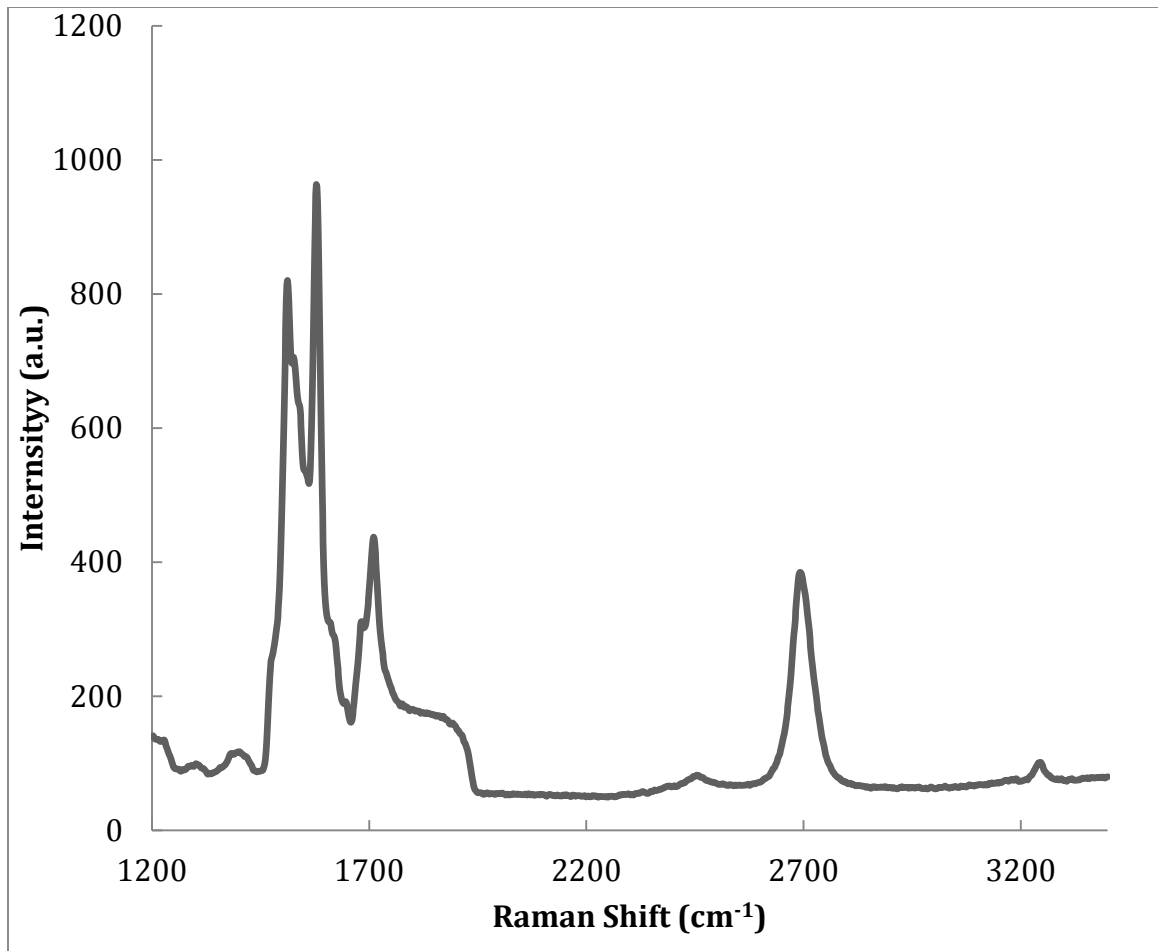
Fig. 2.1: Raman Spectrum with a 532 nm excitation laser wavelength of epitaxial graphene (EG) grown on SiC.

2.1.2 Graphene Oxide

Graphene can be oxidized using Hummers method [63]. The Raman spectrum of Graphene epitaxial graphene oxide (GO) is shown in Fig. 2.2. Unlike pure graphene, which has a very small D band, GO has a relatively large D band at ~1325 cm^{-1}. This is caused by adding oxygen atoms into the graphene lattice and introducing disordered structures of graphene.

Graphene becomes insulating after oxidation due to the saturated sp3 carbon atoms bound to oxygen. GO will reduce to graphene while heated and reduced graphene oxide (rGO) shows a tunable band gap from 2 to 0.02 eV depending on the reduction level [68], and rGO ribbons with different widths can be created by TCNL [93]. Figure 2.3 shows the current and topography images of a zigzag pattern created by TCNL. Direct writing of electronic devices on GO by catalytic lithography is also reported [70]. However, rGO still contains residual oxygen that is sp^3 bonded to carbon atoms even after thermal annealing at 1500 K [70]. The residual oxygen atoms disrupt the flow of charge carriers, which makes it difficult to recover the ballistic transport properties as observed in pure graphene.
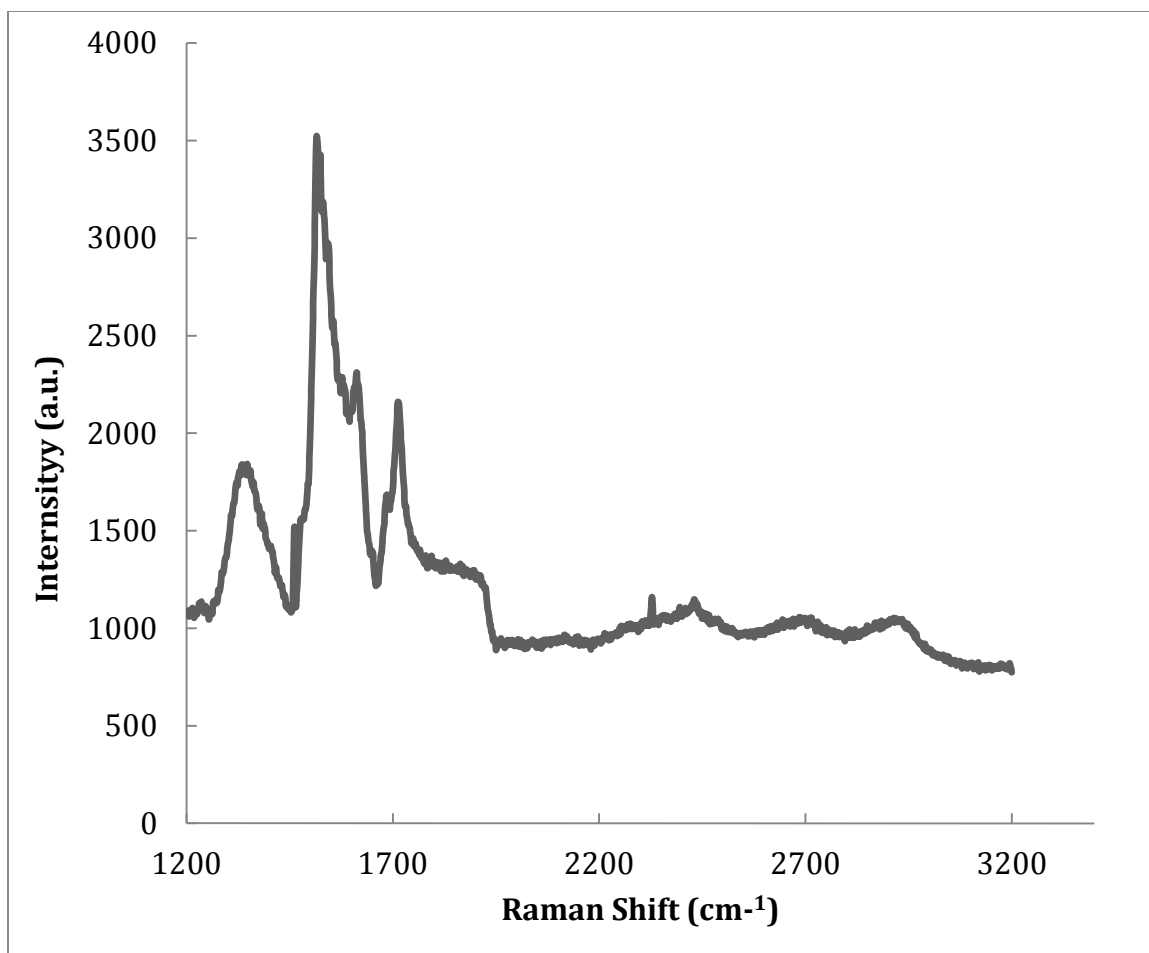
Fig. 2.2: Raman Spectrum with a 532 nm excitation laser wavelength of epitaxial graphene oxide (EGO).
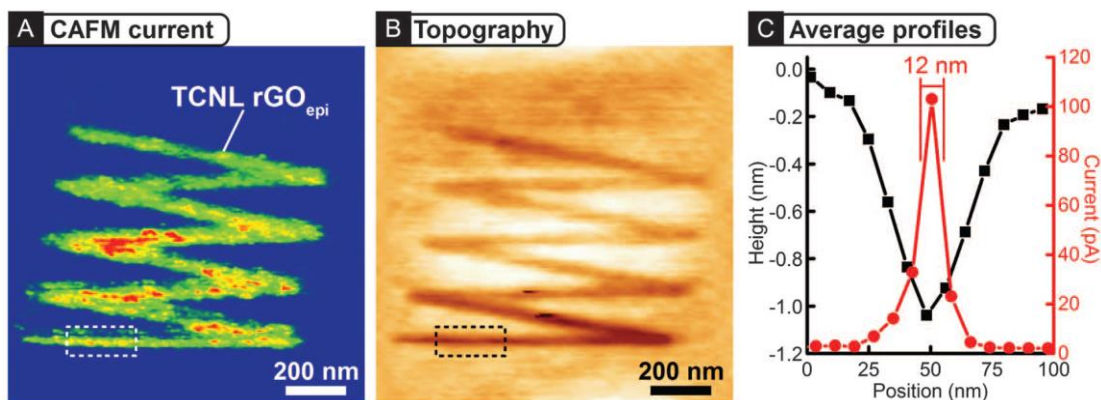
Fig. 2.3: Local thermal reduction of a GO film: current and topographical images. (A) Room temperature AFM current image (taken with a bias voltage of 2.5 V between tip and substrate) of a zigzag-shaped nanoribbon fabricated by TCNL on GO at heater temperature ~1060 °C with a linear speed of 0.2 mm s^{-1} and a load of 120 nN. (B) Corresponding topography image taken simultaneously with (A). (C) Averaged profiles of current and height of the cross sections that are indicated as dashed lines in (A) and (B) [69].

Prof. Sordan's group (Politecnico di Milano) prepared the sample used in the experiments [71]. GO film (thickness ~ 50 nm) was prepared by drop casting colloidal GO dispersion on a Si chip and leaving it to dry at 70°C. Stable colloidal GO dispersions were produced by modified Hummers method. Briefly, graphite flakes (0.3 g, Sigma Aldrich), $NaNO_3$ (0.6 g, Sigma Aldrich), and H_2SO_4 (23 mL, 98%, Sigma Aldrich) were stirred for 15 minutes. $KMnO_4$ (3 g, Sigma Aldrich) was then slowly added and the mixture was stirred for 6 hours at 30°C. Subsequently, 40 mL of deionized (DI) H_2O was added to stop the oxidation reaction, leading to a rapid rise of temperature (~ 70°C). After 30 minutes at this temperature, 100 mL of DI H_2O and 3 mL of H_2O_2 solution (30%) were added to dissolve the insoluble manganese species, turning the color of the mixture to yellow.

Once the reaction was terminated, the oxidized portion was separated and cleaned from unoxidized graphite and other residual species. The cleaning was performed by

centrifugation of the obtained suspension at 7800 rpm for 30 minutes in order to remove both the acidic content and ions. The solid content was collected and redispersed with DI H_2O. This operation was repeated in sequence until the pH of the supernatant raised close to neutrality. At that point, the exfoliation of graphite oxide was performed by prolonged and vigorous shaking, forming a brownish colloidal suspension of GO flakes. Finally, solid unoxidized graphite was removed by mild centrifugation (~ 2000 rpm for 20 minutes). The subsequent collection of the purified supernatant resulted in stable aqueous GO suspensions.

2.1.3 Graphene Fluoride

To improve the quality of GNRs created by TCNL, we seek to replace GO with some other functionalized graphene that can fully reduce to graphene. Recent research has shown a nearly complete reduction of graphene fluoride (GF) to graphene with hydrazine [72]. GF can be obtained by exposing graphene to XeF_2 gas in a commercially available etcher system. The sheet resistivity of reduced graphene fluoride (rGF) ribbons could be lowered to ~22.9 kOhm/□, only 10 times larger than the starting resistivity of CVD graphene. The reduction amount is related to the resistance of the rGF ribbon and could be controlled by changing TCNL parameters such as the tip moving speed, load and heater temperature.

One remarkable advantage of creating GNRs by performing TCNL on GF is that the GNRs are chemically insulated within a large insulating film. Chemical isolation helps to exclude unstable edge effects from cutting, which adversely affect the qualities of GNRs. Another advantage is the potential for rewritable electronics [72] since the reduced GF can be easily fluorinated again.

Fluorinated CVD graphene samples are used for our experiments. The GF samples are prepared and provided by Dr. Sheehan's group (Naval Research Laboratory). The details of the sample preparation are described in Ref. [65]

2.1.4 Polyphenylene Vinylene Precursor Polymer

Polyphenylene vinylene (PPV) is a conjugate polymer with great physical properties. PPV films have a stable structure and are highly photo-luminescence. These properties made PPV a great material for photo-emitting devices and photovoltaic devices [73]. PPV thin films can be used to make a large-scale light-emitting diode (LED) with a high efficiency emission of the green-yellow part from the light spectrum.

PPV thin films with good quality can be conveniently made. A common method is to use a water-soluble sulfonium salt precursor to produce PPV. The precursor can be drop-cast on different substrates. The precursor converts to PPV when heated to 250 ℃. The reaction from the precursor film (poly(p-xylene tetrahydrothiophenium chloride)) (PXT) to polyphenylene vinylene (PPV) is shown Fig. 2.4.
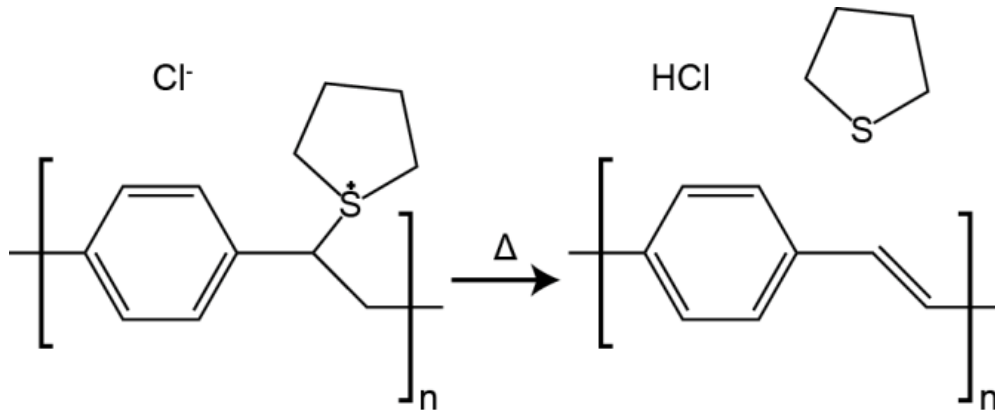
Fig. 2.4: PXT to PPV reaction [71].

28

For the experiment described in chapter 3, PPV precursor films were deposited on silicon substrates [71]. Silicon was cut into 1×1 in^2 samples; they were scrubbed and rinsed with ethanol. The samples were then Piranha cleaned (3:1 sulfuric acid to hydrogen peroxide) for about 30 minutes. The samples were placed in a water bath for 30 minutes, and subsequently rinsed with ethanol and nitrogen dried. For most samples, the PPV precursor was spun cast at rates between 300 and 600 rpm and an acceleration of 330 (0.5 mL at a concentration of 0.25%). The samples were air dried to remove any remaining precursor solvent. For the Raman measurements, the samples were drop cast instead of spin casting.

2.2 Raman Spectroscopy

Raman spectroscopy is a spectroscopic technique that is useful for chemical analysis and material structure characterization. The Raman effect was predicted by Smekal in 1923 [74] and observed in experiment by Raman in 1928 [75]. Raman discovered that when light traverses a transparent material, a small amount of the reflected light changes in wavelength. When photons from a laser or a monochromatic light source interact with the material, such as molecular vibrations and phonons, inelastic scattering, or Raman scattering occurs. Raman scattering shifts the energy of the photon up or down, resulting a decreased or increased photon wavelength. The amount of inelastic scattering is very small (typically the 10^{-8} the intensity of the incident light source), which makes the observation of the Raman effect extremely difficult.

Besides Raman scattering, the majority of incident photons are scattered through an elastic scattering, called the Rayleigh scattering. The Rayleigh scattering does not change

the energy of the incident photon, and thus the wavelength of photon is not changed after Rayleigh scattering.

The Raman effect can be explained by classic theory, regarding the scattering molecule as a collection of atoms undergoing simple harmonic oscillations, without taking account of the energy quantization. The Raman effect is due to the interaction of the electric field of the incident radiation with the scattering molecule. When a molecule is inside an electric field, its electrons are displaced from the nuclei and form an electric dipole moment. The induced dipole moment is given by

$$p = \alpha E \tag{2.1}$$

The constant α is the polarizability of the molecule, determined by the ease with which the shape of the electron clouds can be changed. E is the electric field of the incident radiation. The time-varying expression for E is given by

$$E = E_0 \cos 2\pi t v_0 \tag{2.2}$$

where E_0 is the constant magnitude of the incident radiation, v_0 is its the frequency. Consider a diatomic molecule doing simple harmonic oscillation at small amplitude, with a frequency of v_v. The time-varying coordinate l_v along the oscillation axis is given by

$$l_v = l_0 \cos 2\pi t v_v \tag{2.3}$$

For a small-amplitude oscillation, the time-varying polarizability constant α is given by

$$\alpha = \alpha_0 + \frac{\partial \alpha}{\partial l_v}\bigg|_{l_0} l_v \tag{2.4}$$

Substitute Eq. (2.3) into Eq. (2.4), α can be expressed as

$$\alpha = \alpha_0 + \frac{\partial \alpha}{\partial l_v}\bigg|_{l_0} l_0 \cos 2\pi t v_v \tag{2.5}$$

Inserting the polarizability constant in Eq. (2.5) into Eq. (2.1), the induced dipole moment is

$$p = \alpha_0 E_0 \cos 2\pi t v_0 + \left.\frac{\partial \alpha}{\partial l_v}\right|_{l_0} l_0 \cos 2\pi t v_v E_0 \cos 2\pi t v_0 \qquad (2.6)$$

Equation (2.6) can be rewritten as

$$p = \alpha_0 E_0 \cos 2\pi t v_0 + \frac{\left.\frac{\partial \alpha}{\partial l_v}\right|_{l_0} l_0 E_0}{2} \cos 2\pi t (v_0 + v_v) + \frac{\left.\frac{\partial \alpha}{\partial l_v}\right|_{l_0} l_0 E_0}{2} \cos 2\pi t (v_0 - v_v)$$

$$(2.7)$$

The first term in Eq. (2.7) describes the Rayleigh scattering, while the other terms describe the Stokes and the anti-Stokes Raman scattering respectively. From Eq. (2.7), if the molecular oscillation is Raman active, the polarizability must change in the oscillation. Equation (2.7) also indicates that for the Rayleigh scattering, the scattered photons have a frequency of v_0, the same as the incident photons. For Raman scattering, light will be scattered with a frequency of $v_0 \pm v_v$. These three types of scattering are shown in Fig. (2.1), with quantized vibrational energy

$$E_n = hv(n + \tfrac{1}{2}) \qquad (2.8)$$

For a non-linear molecule, there are 3N-6 vibration modes and for a linear molecule, there are 3N-5 vibration modes. N is the number of atoms in the molecule. When the energy of the incident photons is smaller than the energy required to excite electronic transitions, virtual energy levels are used in Fig. 2.5 to demonstrate the scattering process.

In this research, Raman spectroscopy is used for the characterization of PPV patterns created by TCNL. A Horiba Lab LabRAM HR800 micro Raman system coupled with an Olympus BX41 inverted optical microscope was used for the spectroscopy measurement. The confocal Raman spectroscope has high spatial resolution in

micrometer scale. Laser diodes with 785 nm and 532 nm wavelengths are used, with a

max power of 20 mW. Figure 2.1 and 2.2 are the Raman spectra of epitaxial graphene

and graphene oxide samples.
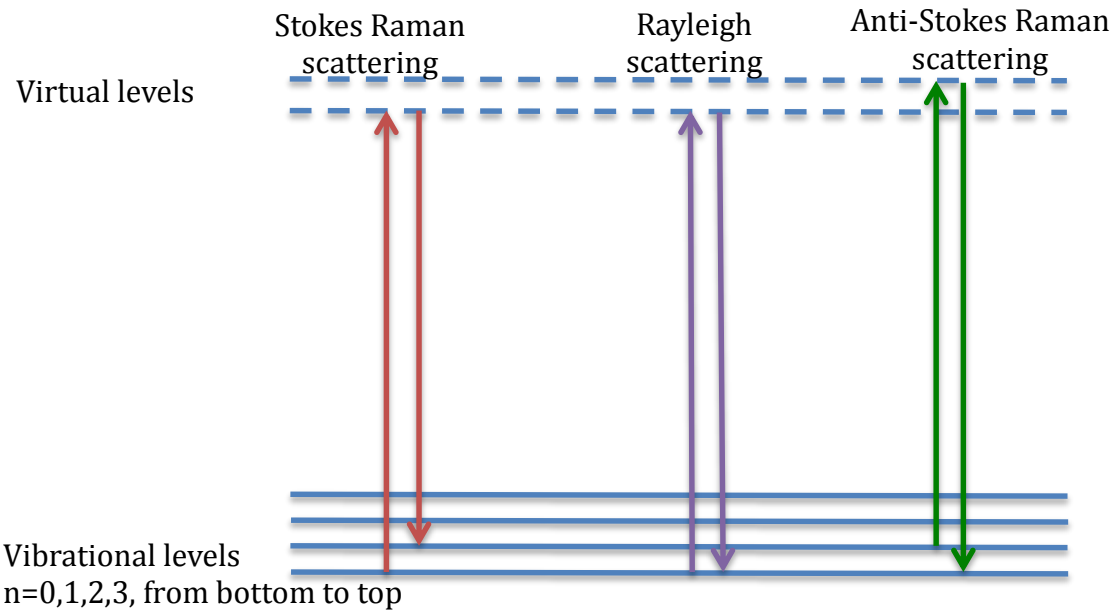
Fig. 2.5: Energy diagram of Stokes Raman scattering, Rayleigh scattering and anti-Stokes Raman scattering.

Fig. 2.6: XY Piezo stage with an open center (from PI P-713 Piezo Scanner datasheet).

A PI P-713 XY piezo stage is configured to the Raman system for the mapping. Figure 2.6 is a photo of the stage. During Raman mapping, the sample is placed at the center of the stage, for the Raman laser to pass through the open center of the stage. The travel range of the stage is 15×15 micron. Both the X and the Y axes are controlled through a single RS232 cable. The Raman mapping is useful for the detection of patterns created by TCNL and to analyze adjacent areas with different atomic constitutions/structures. The mapping spectra of PPV and PPV precursor are shown in Fig. 2.7.

(a)

(b)
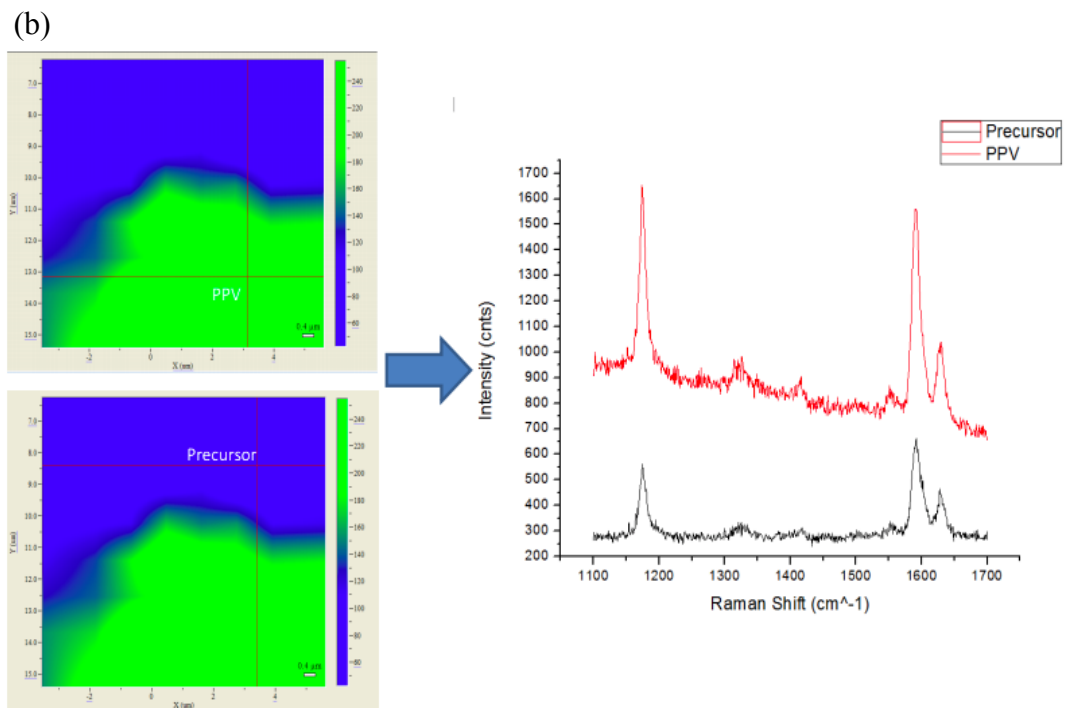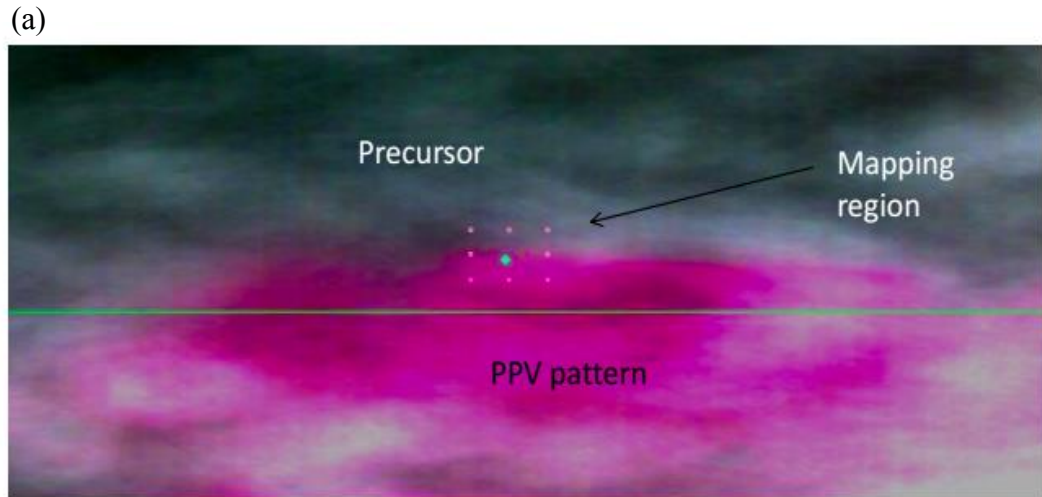
Fig. 2.7: Raman mapping measurement of the PPV pattern and the precursor. (a), camera view of the measured area. Mapping measurement was performed on the spots marked by the 3 by 3 array. (b), Raman spectra of the PPV pattern (red) and the precursor (yellow). The mapping measurement result is shown on the left, showing the precursor (blue) and the PPV (green).

2.3 Atomic Force Microscope Characterization

Atomic Force Microscopy (AFM) is a scanning probe microscopy that can resolve features with atomic resolution, for both conductive and non-conductive samples. AFM provides three-dimensional information and makes it possible to image in-situ, in fluid and under controlled environments. AFM is a useful tool for the study of materials properties and has a great application in materials science, electrochemistry, polymer science, biophysics and nanotechnology.

The working principles of an AFM are shown in Fig. 2.8. A sharp tip at the free end of a cantilever approaches to the sample surface and interacts with the surface, causing the cantilever to bend. A laser spot is aligned with the end of the cantilever and the laser is reflected from the cantilever onto a photodiode. The photodiode is position sensitive and consists four sections, A, B, C and D. The bending of the cantilever causes the signal from the photodiode to change, and the resulting signal is the Deflection, which contains the topography information of the sample.

Figure 2.9 demonstrates the tip-sample interaction during the cantilever approach and retraction. As the tip comes closer to the sample surface, the deflection signal drops significantly when the tip comes into contact with the surface, this is due to strong capillary and adhesive forces, holding the tip down to the surface. As the cantilever presses harder into the surface, the deflection signal starts increase, due to cantilever bending. In the contact region, the total force that the tip exerts on the sample is the addition of the capillary force, the adhesive force and van der Waals force.
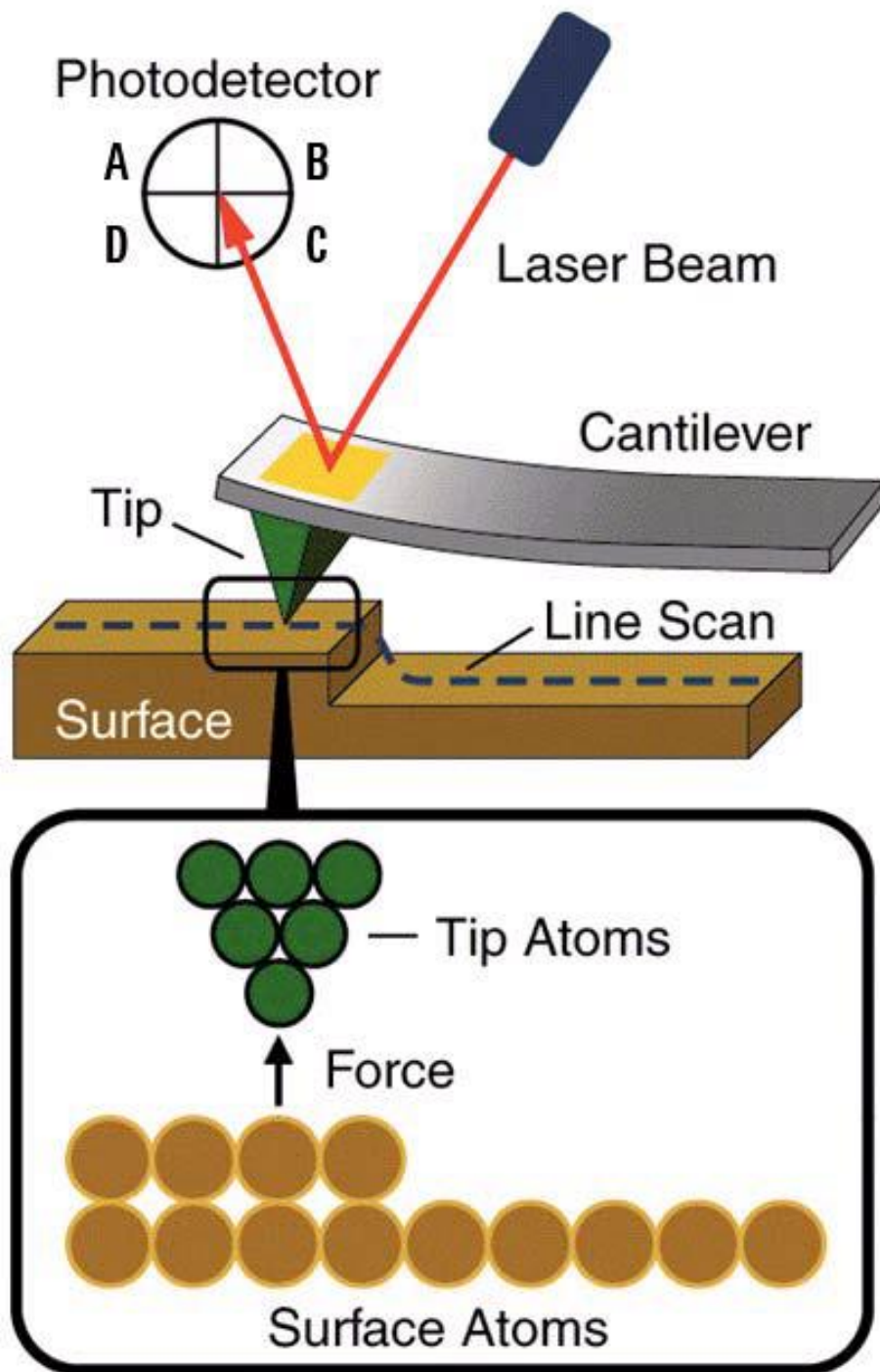
Fig. 2.8: AFM working principles (Agilent 5500 manual).
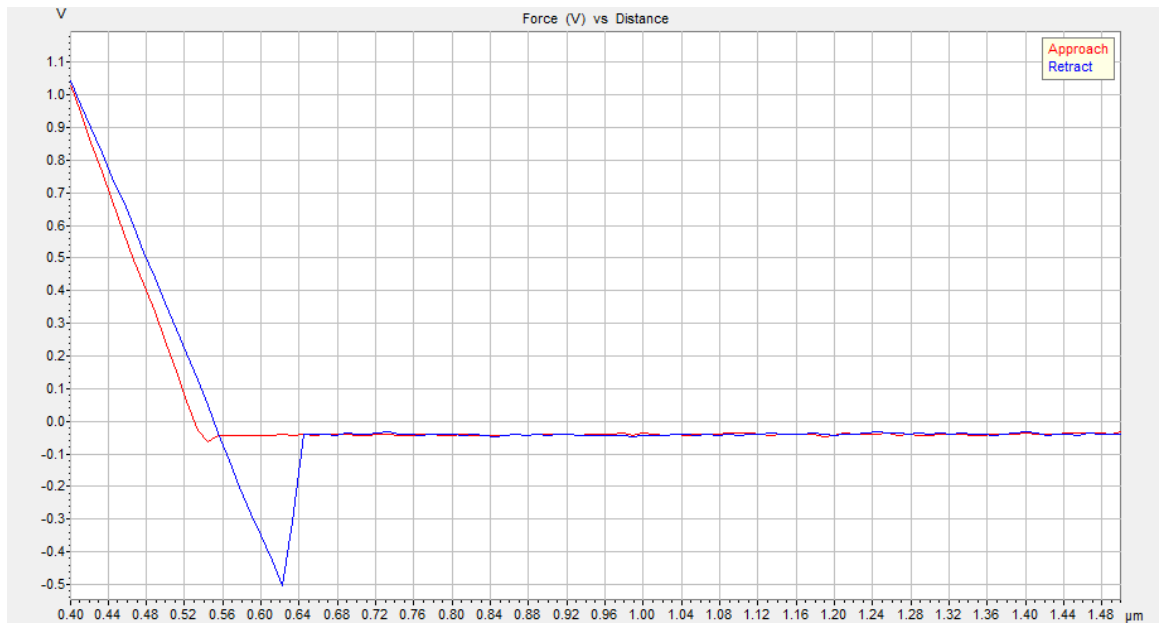
Fig. 2.9: Force vs Distance curves during the cantilever approach and retraction.

2.3.1 Topography Microscopy

Topography microscopy is a contact mode AFM microscopy. Topography image is constructed from the deflection signal recorded during the AFM scan. Topography changes in the sample will result in a change in the vertical bending of the cantilever, and thus change the direction of the reflected laser. The calibration profile of the AFM is used to convert the deflection signal into topography information. Topography information is useful for the analysis of the sample chemical composition and structure. For example, the topography image of a reduced graphene fluoride pattern is shown in Fig. 2.10. The reduced height in topography indicates a successful removal of the fluorine.

Friction

165.00 mV

98.00 mV

Topography

5.00 nm

0.00 nm
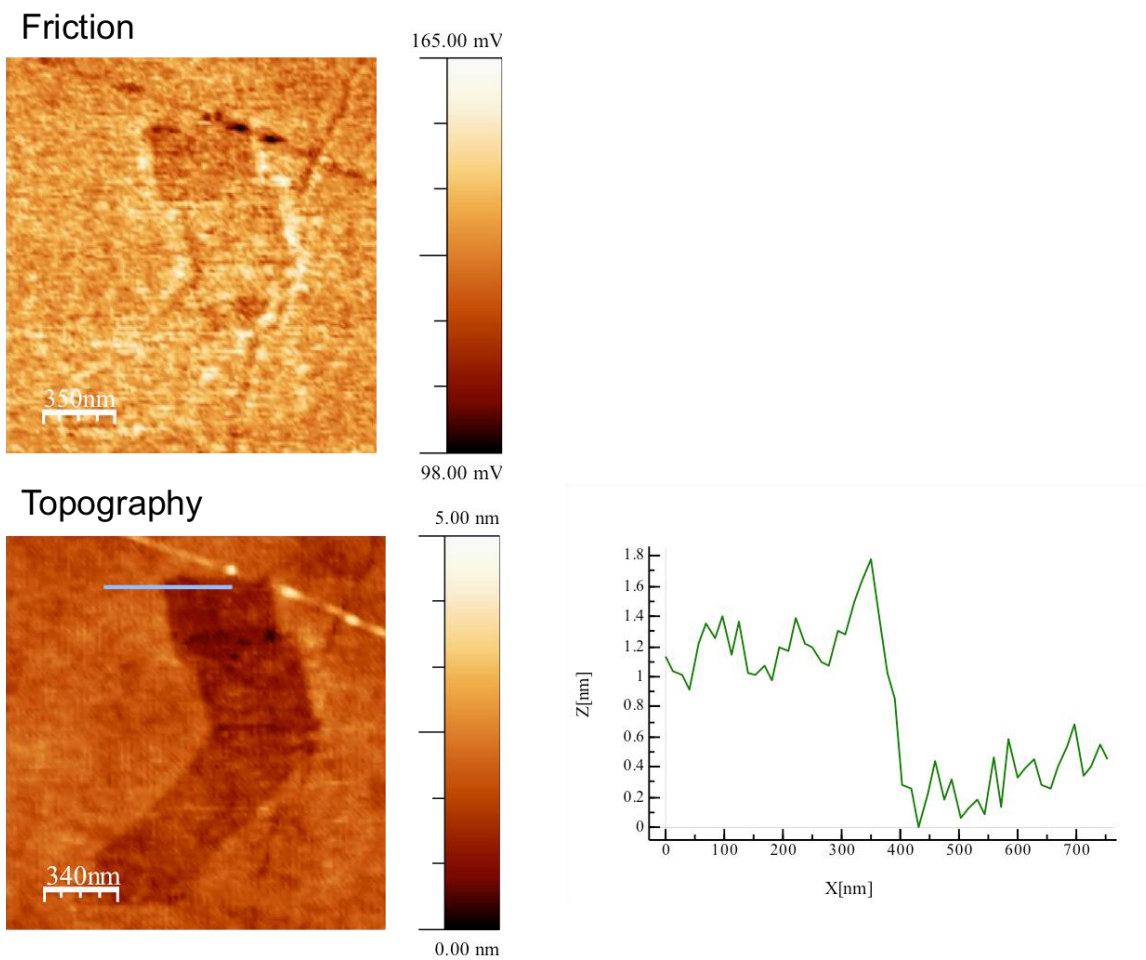
Fig. 2.10: Friction and topography measurement of a reduced graphene fluoride pattern created by TCNL. The cross-section of the topography image is shown on the right.

2.3.2 Friction Force Microscopy

For the friction force microscopy, the tip is in contact with the sample surface. During a typical scan, the cantilever twists in the scan direction due to the lateral force applied to the tip from the sample. This change of the twist will change the direction of the reflected laser and can be recorded by the photodiode as the friction signal.

Changes in the lateral force can be caused either by changes in frictional properties of the sample or by changes in topography of the sample. Thus the friction signal contains both of these two components. To separate the friction information from the topography information, the friction force is usually recorded twice, during the trace and retrace of an AFM scan. One image can be inverted and subtracted from the other one to reduce the topography effect.

Friction force microscopy is useful to identify materials similar in topography but different in frictional properties. Fig. 2.11 contains the friction and the topography images of a graphene sample on SiC substrate. Graphene ribbons are expected to form at the edge of the step features called Mesa. It is easier to identify graphene in the friction image, with the drastic contrast between graphene and the SiC substrate.
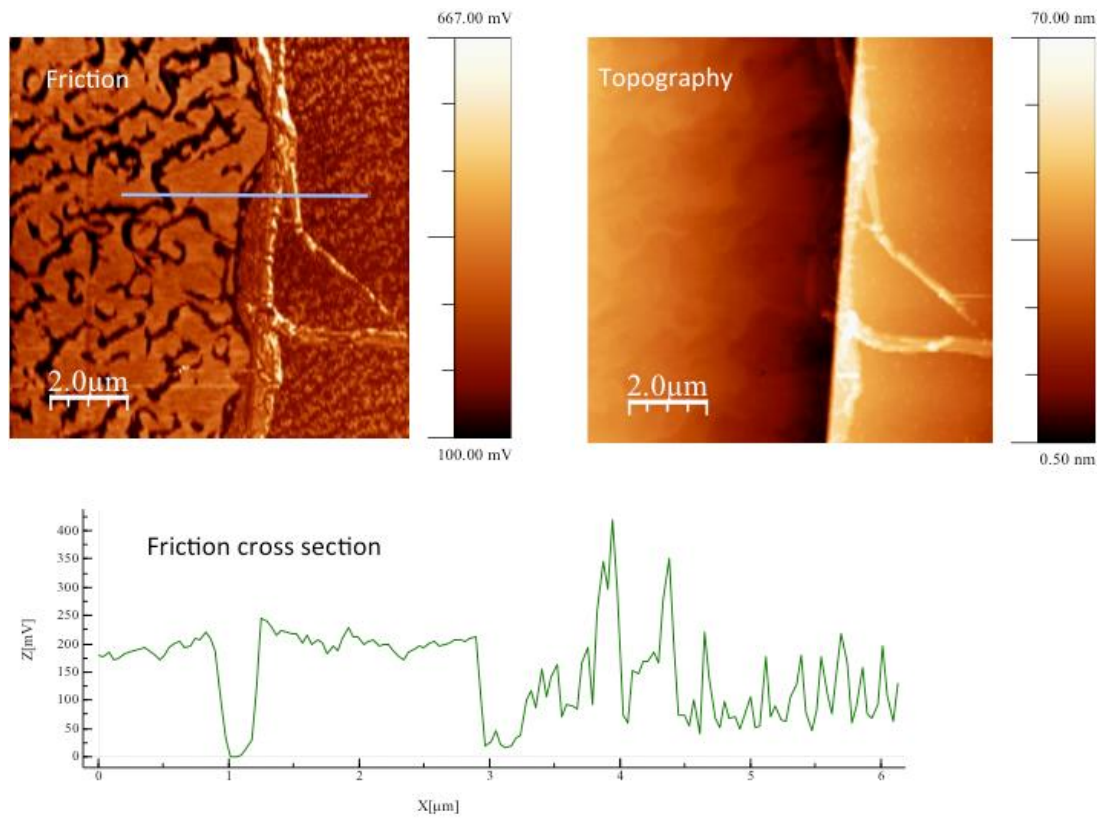
Fig. 2.11: Friction and topography measurement of a Mesa graphene sample.
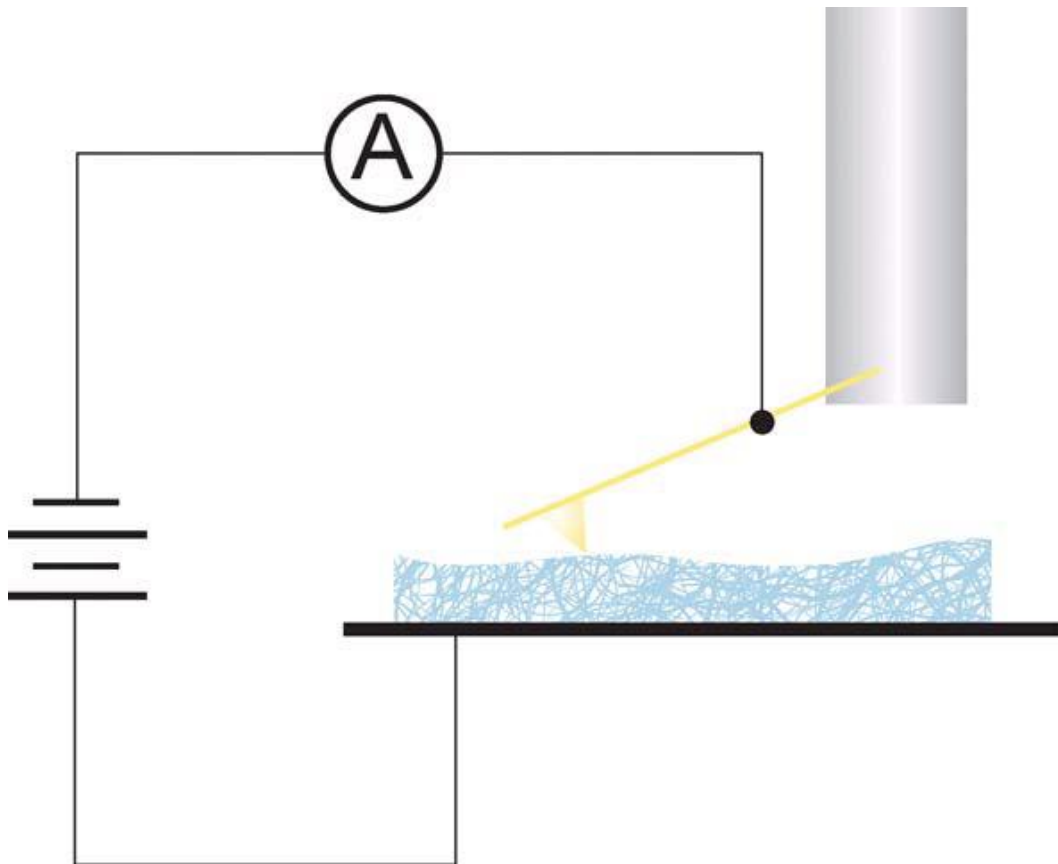
Fig. 2.12: Schematic of current sensing AFM. A cantilever with conductive coating is used for the imaging (Agilent 5500 manual).

2.3.3 Current Sensing AFM

Current sensing AFM is a powerful technique to characterize the variation of conductivity of a conducting sample [76]. During current sensing AFM, an ultra-sharp AFM cantilever, with conductive coating, probes the conductivity of the sample. Topography and friction information can usually be acquired at the same time. The schematic of current sensing AFM is shown in Fig. 2.12. A bias voltage is applied to the sample while the cantilever is kept at virtual ground. A negative or positive bias can be applied. The current flow from the tip to the sample or sample to the tip is recorded (according to the applied bias) and used to construct the conductivity image. In chapter 4.1, current sensing AFM is used to characterize conducting graphene nanoribbons created on a graphene oxide sample.

2.3.4 Kelvin Probe Force Microscopy

Kelvin probe force microscopy (KPFM) operates in a noncontact mode of AFM [77]. The work function of the sample surface can be recorded through KPFM at atomic scale. In a metal, the work function φ is defined as the energy difference between the vacuum state and the Fermi energy, which is also the minimal energy required to remove an electron from the metal to vacuum. For semiconductors, the work function can be regarded as the difference in energy between the vacuum energy level and the most loosely bounded electron. KPFM is a useful technique for the study of surface reconstruction [78], doping and band-bending of semiconductors [79].

A conductive cantilever is used for KPFM. The cantilever is a reference electrode that forms a capacitor with the sample surface, and the cantilever scans above the sample at a constant height. The cantilever oscillates but not driven at its resonance frequency ω_0,

while an AC bias V_{AC} is applied at the resonance frequency ω_0. A DC bias V_{DC} forms between the cantilever and the sample when the cantilever and the sample are close, since electrons will flow from the material with a lower work function to the material with a higher work function. The AC and DC bias will cause the cantilever to vibrate. The energy of the capacitor formed by the cantilever and the sample can be expressed as

$$E = \frac{1}{2} \cdot C(V_{DC} + V_{AC}\sin(w_0 t))^2$$

$$= \frac{1}{2} \cdot C\left[2V_{DC}V_{AC}\sin(w_0 t) - \frac{1}{2}V_{AC}{}^2\cos(2w_0 t) + V_{DC}{}^2 + \frac{1}{2}V_{AC}{}^2\right] \quad (2.9)$$

The first term in the above equation will cause the cantilever to oscillate at its resonance frequency ω_0. This oscillation can be detected through the photo detector. A null circuit is used to apply a DC potential to minimize the oscillation. This DC potential is recorded and produces an image of the work function of the sample.

CHAPTER 3

THERMOCHEMICAL NANOLITHOGRAPHY AND ITS

PARALLELIZATION INSTRUMENTATION

3.1 TCNL with a Single Cantilever

TCNL is a probe based lithography technique that uses a heated atomic force microscope (AFM) tip to activate chemical reaction precisely. The heater temperature is controllable from room temperature to approximately 1414 °C (the melting temperature of silicon). Arbitrary-shaped patterns [80-83] and chemical gradients [84] can be made through TCNL. For this research, both the single cantilevers and the cantilever arrays are fabricated and provided by Prof. King's group (University of Illinois at Urbana-Champagne). The fabrication and characterization of the single thermal cantilever and cantilever array is reported in Ref. [85] and [86].

3.1.1 Single Thermal Cantilever Instrumentation

The cantilevers used for TCNL are called thermal cantilevers and the scanning electron microscope image of a thermal cantilever is shown in Fig. 3.1 [86]. A thermal cantilever contains high-doped silicon legs and low-doped heating region close to the tip. When current passes through the cantilever, the tip area acts as a heater. The inset shows a tip curvature below 20 um and a tip height of about 2 um.
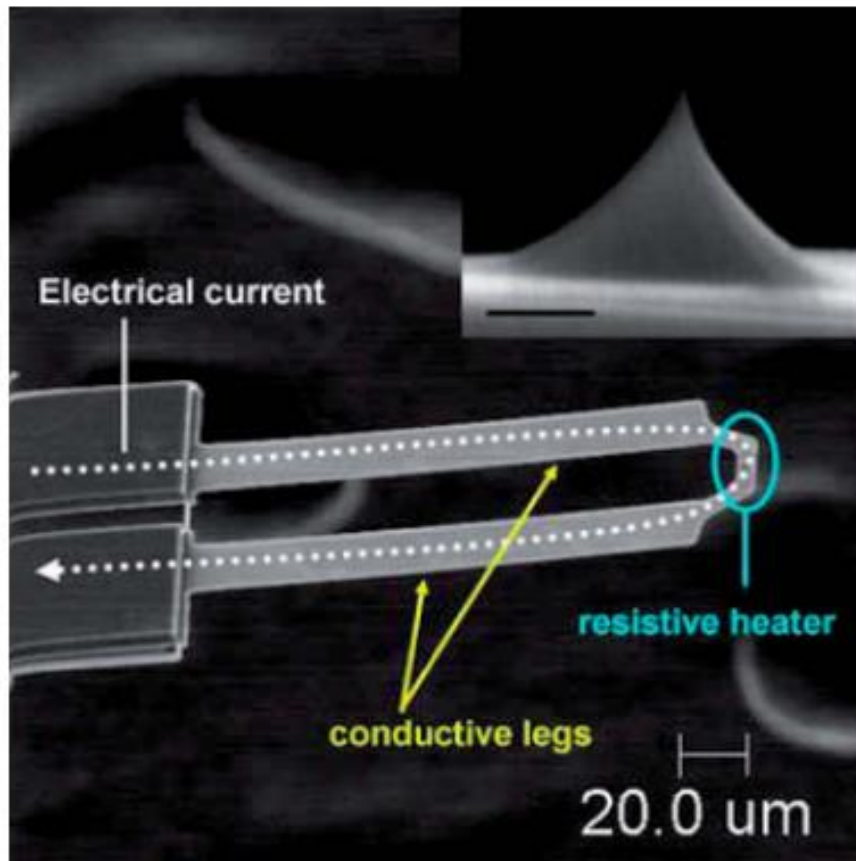
Fig. 3.1: Scanning electron microscope image of a thermal cantilever. Current travels along the high doped, conductive legs and across the low doped, heating region. The inset shows the cantilever tip with radius of curvature below 20 nm. The tip height is about 2 um. The scale bar of the inset is 300 nm [86].
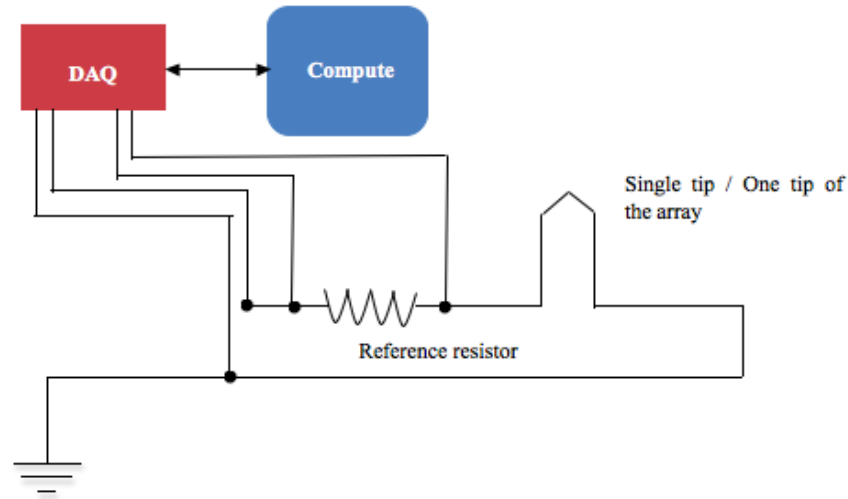
Fig. 3.2: Schematic of the TCNL instrumentation.

To perform TCNL, the thermal cantilever is attached to a magnetic tip holder, using super glue. The tip holder contains printed circuit to which the two legs of the thermal cantilever can be connected, using sliver epoxy. The tip holder is then mounted to the AFM scanner nosecone and connected to the main TCNL circuit as shown in Fig. 3.2.

In Fig. 3.2, a NI cDAQ-9178 is used to both apply and monitor the voltage in the circuit. Analog input/output modules are installed into the DAQ chassis. Up to 8 different modules can be installed into the chassis, and for our experiments two analog input modules and two analog output modules are installed. The maximum output voltage from the DAQ is 10V. To satisfy the voltage requirement for TCNL, the output voltage is amplified twice using an operational amplifier (not shown in the figure). This provides the circuit with a maximum voltage of 20V. The thermal cantilever is connected in series with a 2 kOhm resistor, which is called the reference resistor. 2 kOhm is chosen because

the thermal cantilever usually has a resistance between 1 kOhm to 5 kOhm. During the TCNL temperature calibration, the voltage across the reference resistor is monitored by the DAQ. By using a reference resister with a resistance close to the thermal cantilever's resistance, the voltage measurement will be more accurate. In the actual circuit, we divided the 2 kOhm resistor into two 1 kOhm resistors, and monitor the voltage across one resistor, such that the measured voltage will not exceed the maximum input limit of the DAQ, which is 10 V.

In order to create arbitrary shaped patterns through TCNL, Matlab programs were written to control the tip movement and tip temperature during the lithography process. A Matlab program for creating polygon patterns is attached in Appendix A. A Matlab program to transfer an arbitrary picture into a nanoscale pattern on a sample is attached in Appendix B.

3.1.2 Heater Temperature Calibration

Since the local thermochemical reactions greatly depend on the temperature, the precise control over the heater temperature is very important to this thesis research. The heater temperature is determined by performing a temperature calibration before each TCNL experiment. A Matlab program is written to perform the calibration (appendix C). A typical calibration curve is shown in Fig. 3.3.

During the calibration, the total voltage applied to the TCNL circuit can increases from 0 V to a maximum of 20 V, depending on what temperature will be used for TCNL. In Fig. 3.3, the voltage increased from 0 V to 9.5 V. The voltage across the reference resistor is V_R, and the total voltage applied is V_{tot}. The voltage across the thermal cantilever V_H is given by
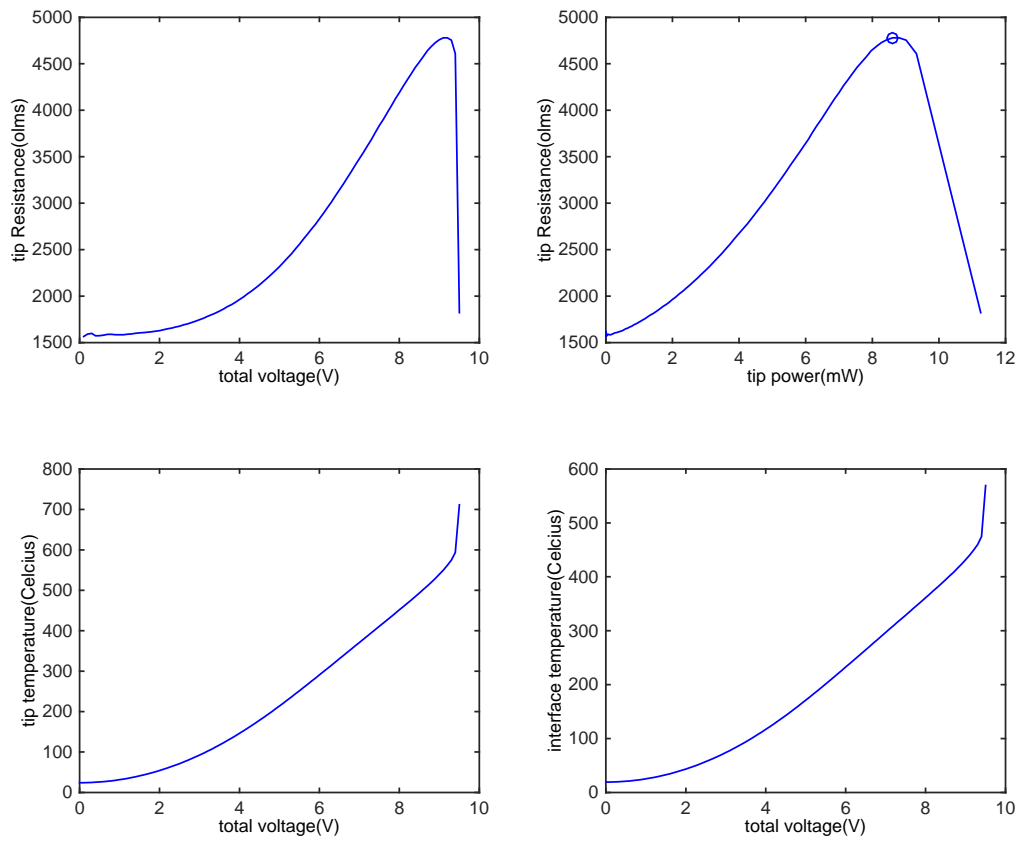
Fig. 3.3: Temperature calibration curves. The tip resistance, tip dissipated power, heater temperature and interface temperature are recorded. The maximum tip power is automatically recorded and is shown in the tip-resistance vs tip power subfigure.

$$V_H = V_{tot} - V_R \qquad (3.1)$$

The current passing through the heater I_H is given by

$$I_H = \frac{V_R}{R_R} \qquad (3.2)$$

where R_R is the reference resistor, with a value of 2 kOhm.

Combine Eq. (3.1) and (3.2), the power dissipated by the heater P_H is

$$P_H = (V_{tot} - V_R)\frac{V_R}{R_R} \qquad (3.3)$$

From the calibration curve in Fig. 2.4.2, the tip resistance R_H has a nonlinear relation with P_H. R_H is 1500 Ohm at room temperature when P_H is 0 mW. As the tip dissipated power increases, the tip resistance first increases to a peak value of 4750 Ohm when P_H is 8.6 mW, and then decreases as P_H increases. This is due to the competition between increased electron scattering and intrinsic carrier generation. As the tip dissipated power increases from 0 mW, the tip resistance increases with the dissipated power, since the carrier mobility of the doped silicon decreases with temperature, and the dissipated power causes the temperature of the doped silicon to increase. The number of intrinsic carriers in the silicon also increases with temperature. As the temperature continues to increase, the tip resistance stops increasing when the tip temperature reaches the thermal runaway temperature at approximately 550 ℃. The tip resistance decreases sharply after the thermal runaway temperature and the tip temperature increases

dramatically. Cantilevers heated at a steady state have been well studied for this thermal runaway effect [87].

Since the resistance of the cantilever may has the same value at two different temperatures, and the tip dissipated power has a unique value at a particular temperature, we use the tip dissipated power P_H to predict the heater temperature T_H. T_H can be calibrated by external thermometry measurement of the cantilever that is self-heated with power P_H. Optical thermometry has advantages over other temperature measurements because it does not require a sensor to contact the measured area. Infrared microscopy can measure the temperature of a sample from the emitted thermal radiation [88]. The size of the infrared measurement is limited by diffraction with a resolution of 3 um, which is close to the total size of the heater region in the cantilever. Raman spectroscopy has submicron spatial resolution, which makes it a preferable method for the heater temperature measurement.

In Raman spectroscopy, the temperature of the measured spot can be determined from the Stokes/anti-Stokes ratio, the Stokes peak width or the Stokes peak position. The first two methods provide absolute temperature measurement, but they require a relatively long acquisition time due to the weakness of the anti-Stokes signal and statistical fluctuations. Additionally, for silicon, measurement of the Stokes/anti-Stokes ratio loses sensitivity above 500 ℃, which is not sufficient for this thesis experiments. Measurement of the Stokes peak position can be performed quickly and accurately, but the peak position can be affected by the sample stress. The absolute frequency shift ω_{shift} and the temperature T can be described in the equation [89].

$$\omega_{shift} = \omega_0 + A\left[1 + \frac{2}{\exp\left(\frac{\hbar\omega_0}{2kT}\right) - 1}\right] + B\left[1 + \frac{3}{\exp\left(\frac{\hbar\omega_0}{2kT}\right) - 1} + \frac{3}{\left(\exp\left(\frac{\hbar\omega_0}{2kT}\right) - 1\right)^2}\right]$$

(3.4)

where ω_0, A and B are material characterization parameters for doped silicon. The relationship between the frequency shift and the temperature is nonlinear, but it can be assumed linear between room temperature up to 1000 ℃, a temperature region sufficient for most of the TCNL experiments in this thesis.
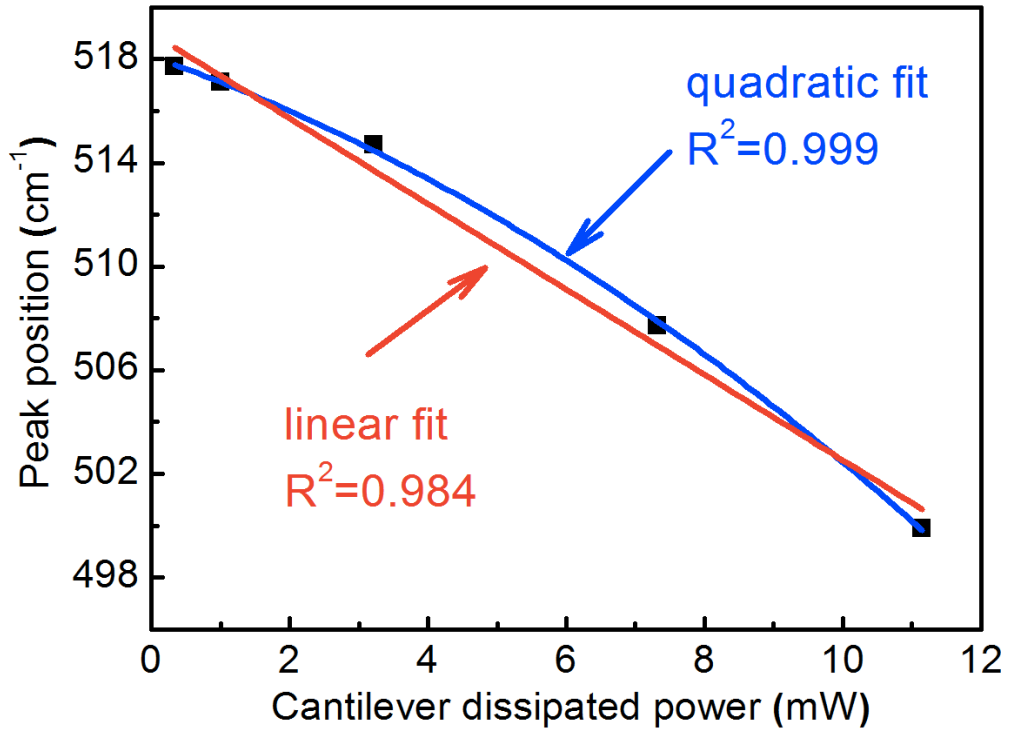
Fig. 3.4: Stokes peak position as a function of cantilever dissipated power. A linear fit could be used for the fitting of the data, although a quadratic equation would fit the data better [90].

Figure 3.4 shows the fitting of the Stokes peak position as a function of cantilever dissipated power. Since the Stokes peak position shifts almost linearly with the tip dissipated power, a linear equation can be used to calculate the heater temperature from the tip dissipated power. The heater temperature can be estimated using the equation

$$T_H = RT + \frac{T_i - RT}{P_i} P_H \qquad (3.5)$$

where RT is room temperature, T_i is the intrinsic temperature and P_i is the cantilever power at the intrinsic temperature. The temperature of the heater during lithography is thus controlled by the value of P_H.

3.1.3 Tip-Sample Interface Temperature Modeling

During the TCNL process, the tip-sample interface temperature T_{int} is of great interest because local chemical reactions are activated at this temperature and is in general different from the heater temperature T_H, as described in Eq. 3.5. T_{int} is determined by the thermal resistances of the sample R_{sample}, the tip-sample interface thermal resistance R_{int} and the sample spreading resistance R_{spread}. The schematic of TCNL tip-surface interface temperature profile is shown in Fig. 3.5. Heat can also flow directly from the heater to the sample through the ambient air between them. However, the temperature rise on the sample surface by heat transferred through air is significantly small than the temperature rise caused by the tip, since the thermal resistance of the ambient air is much larger than the sample spreading resistance. This makes TCNL a highly localized technique to modify the surface chemistry.
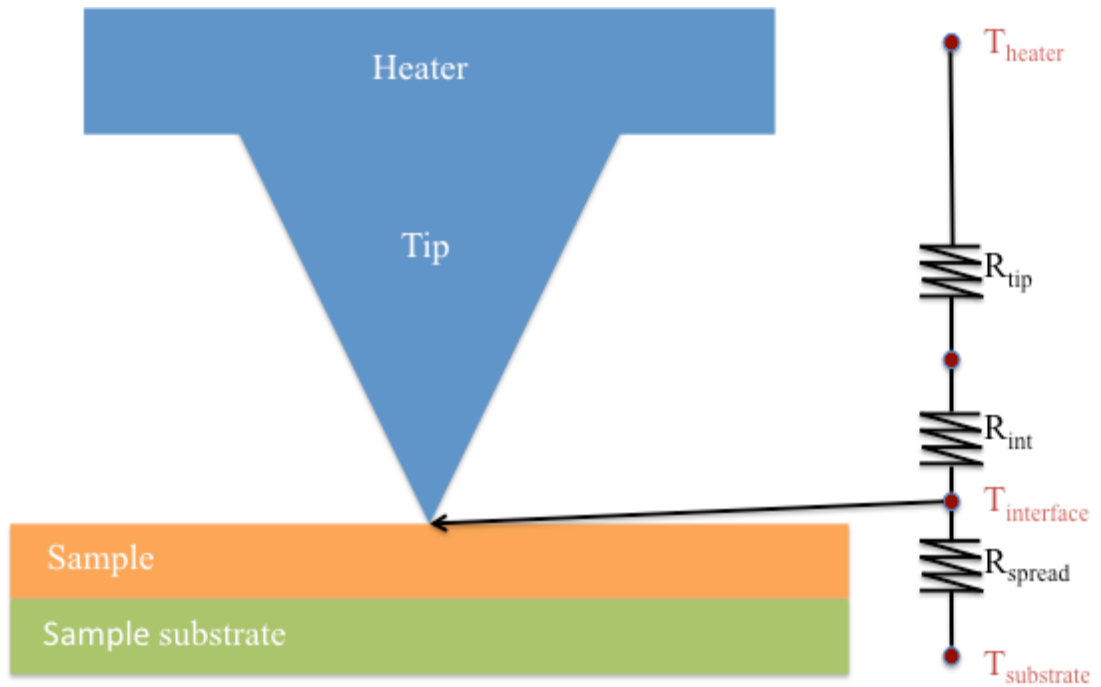
Fig. 3.5: Schematic of TCNL tip-surface interface temperature profile. The interface temperature is different than heater temperature and can be determined from the thermal resistances of the tip, the interface and the sample spreading thermal resistance.

With the method described in the literature [103, 114], we can estimate the temperature at the tip-sample interface. The thermal conductivity K is determined by the thermal conductance of the phonons within the tip, and is given by [91]:

$$K = \frac{1}{3}C \cdot v\left(\Lambda_0^{-1} + d^{-1}\right)^{-1} \tag{3.6}$$

where C is the volumetric heat capacity, v is the average phonon speed, Λ_0 is the temperature dependent phonon mean free path, and d is the structure diameter. For bulk silicon at room temperature, C v is 1.8×10^9 W/m^{2}K, Λ_0 is 260 nm.

The integral expression for the tip thermal resistance R$_{tip}$ with varying d is given by [92]:

$$R_{tip} = \int_{2rL/D}^{L} \frac{dz}{K(z)A(z)} = \frac{3}{2Cva}\left(1 - \left(\frac{2a}{D}\right)^2\right)^2 + \frac{4}{2K_{tip} \cdot a}\left(1 - \frac{2a}{D}\right) \tag{3.7}$$

where z is the height from the tip apex to the tip base, L is the tip length, D is the tip base diameter, a is the tip radius. K(z) is the height dependent thermal conductivity as shown in Eq. 3.6, A(z) is the surface area, K_{tip} is the bulk thermal conductivity of the tip. The above equation gives a thermal resistance in the order of 10^6 K/W.

At the interface, the thermal resistance occurs due to phonon scattering between the tip and sample surface. The interface thermal resistance R$_{int}$ can be estimated by [93]

$$R_{int} = \frac{r_{int}}{\pi a^2} \tag{3.8}$$

where r_{int} is the thermal boundary resistance. The expected value for R$_{int}$ is in the order of 10^7 K/W for tip radius of 5 nm.

The spreading resistance can be estimated using the equations below [94]

$$R_{spread} = \frac{1}{\pi a k_1} \int_0^\infty \frac{1 + K exp\left(-\frac{2\zeta t_1}{a}\right)}{1 - K exp\left(-\frac{2\zeta t}{a}\right)} J_1(\zeta) \sin(\zeta) \frac{d\zeta}{\zeta^2} \qquad (3.9)$$

$$K = \frac{1 - \frac{k_2}{k_1}}{1 + \frac{k_2}{k_2}} \qquad (3.10)$$

where k_1 is the thermal conductivity within the sample, k_2 is the thermal conductivity within the substrate, t_1 is the sample thickness and J_1 is the Bessel function. For different samples and substrate, the spreading resistance varies. For SiC substrate, the thermal conductivity k_2 is $\sim$ 380 WK^{-1}m^{-1} [95]. For graphene, the thermal conductivity k_1 is $\sim$ 1 WK^{-1}m^{-1} [96]. The estimated R_{spread} is in the order of 10^7 WK^{-1}m^{-1}.

After the derivation of the thermal resistances of the tip, interface and the sample/substrate, we can estimate the interface temperature T_{int}. The ration between T_{int} and the heater temperature T_{heater} is given by

$$c = \frac{T_{int}}{T_{heater}} = \frac{R_{spread}}{R_{tip} + R_{int} + R_{spread}} \qquad (6)$$

For graphene sample on SiC substrate, c is $\sim$ 10%.

3.2 TCNL with a Cantilever Array Instrumentation

We used an array of five thermal cantilevers as shown in Fig. 3.6. The array contains five cantilevers with almost identical thermal and mechanical properties. During the TCNL process, each tip from the array works as a single tip as described in Chapter 3.1. Each tip is individually addressable and therefore each tip can be heated independently from one another by controlling the electronic current that flows into each cantilever and heats the resistive tip. The design of the array and cantilevers is reported elsewhere [85].

This probe array was mounted on a commercial Agilent 5500 AFM, as shown in Fig. 3.7 and Fig. 3.8. In Fig. 3.7, the cantilever array is wire bonded to a printed circuit board (PCB), and the PCB is then connected to a customer made AFM nosecone, using two screws. A flex cable is used to connect the PCB into the lithography circuit.

The connection between the flex cable and the lithography circuits are shown in Fig. 3.8 (a). Five identical lithography circuits are used for the array and are inside the shielding box. The details of a single circuit are shown in Fig. 3.8 (b), and the schematic of the circuit is shown in Fig. 3.2. The circuit can also be used for single-tip TCNL, as described in Chapter 3.1, which just needs one circuit, instead of five. An operational amplifier chip LM324N is used to amplify the DAQ output by a magnitude of 2, to satisfy the temperature requirement for some TCNL experiments.
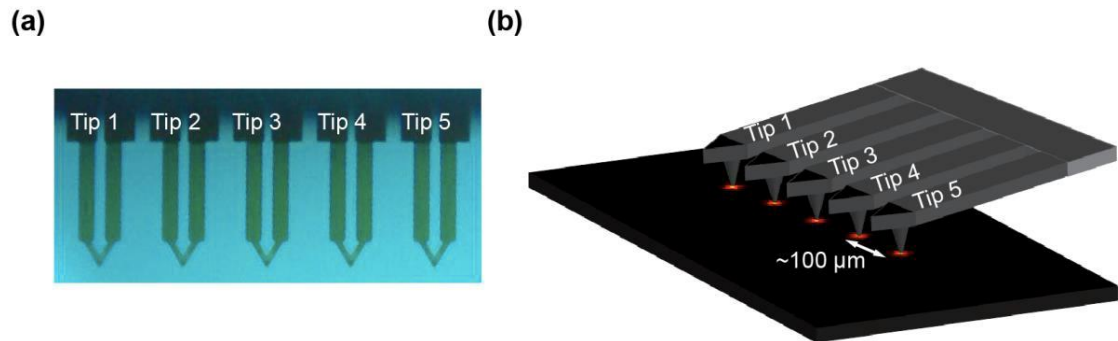
Fig. 3.6: Geometry of the array [71].
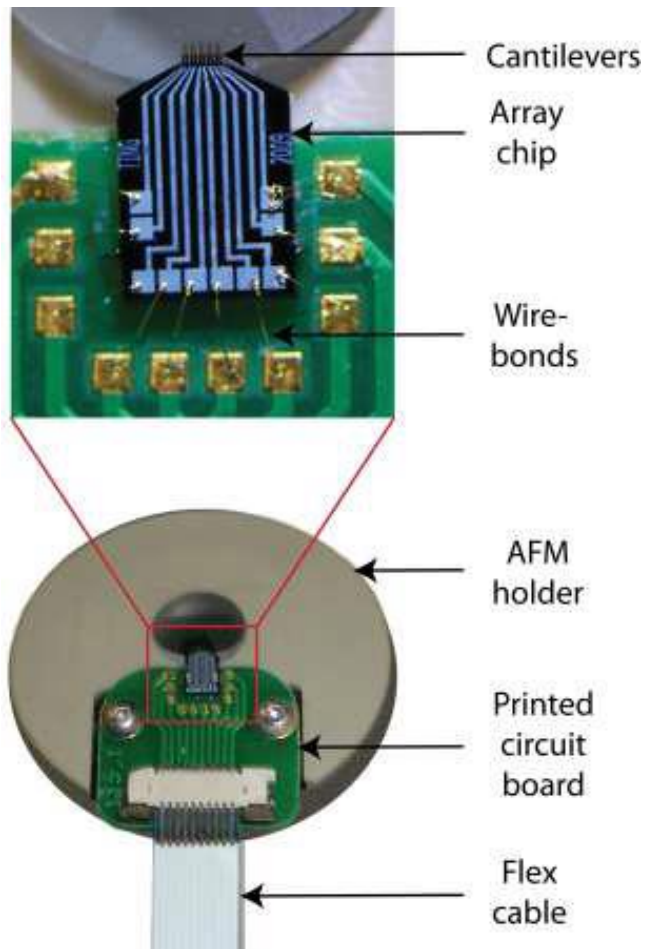
Fig. 3.7: Printed circuit board (PCB) of the array and a picture of the PCB attached to AFM holder.
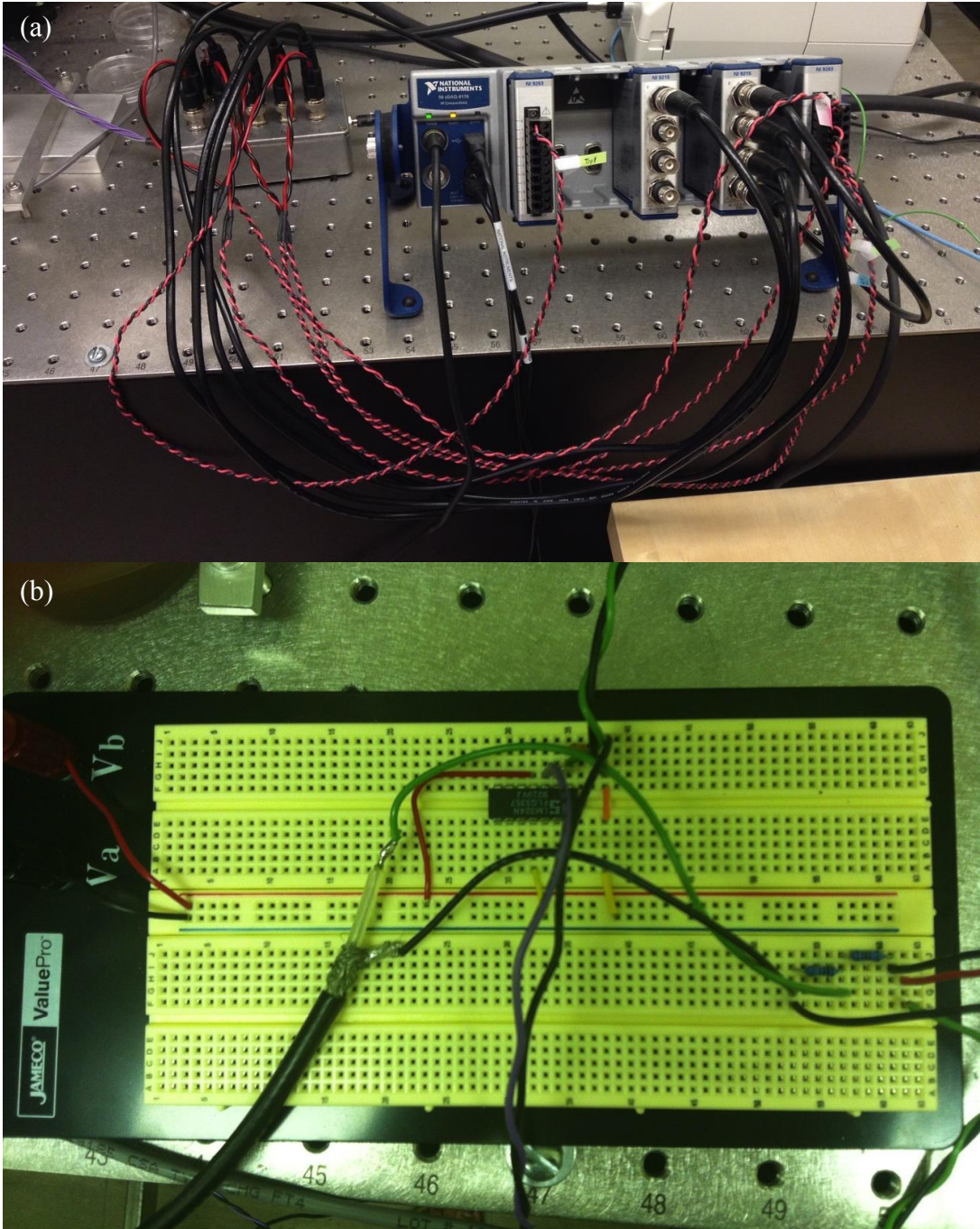
Fig. 3.8: Connection between the DAQ and array PCB. (a) The DAQ is connected to a shielding box, containing five identical circuits. The purple wires connect the shielding box to the array PCB. (b) A demonstration of just one cuicuit inside the shielding box. The cuicuit inculdes an operatonal amplifier chip and two 1 kOhm resistance.
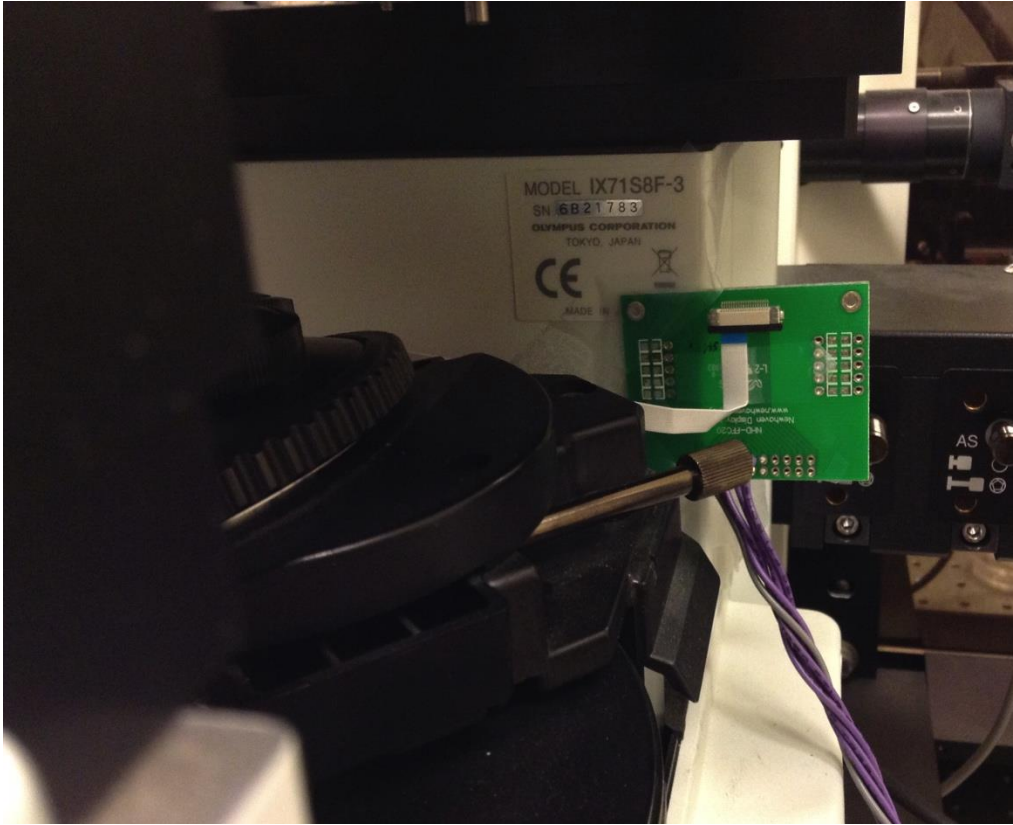
Fig. 3.9: The array PCB is fixed below the AFM scanner. The purpule wires connect the PCB to the DAQ. One side of the white cable connects to the PCB, and the other side connects to the array.

One of the key steps for TCNL with an array is to ensure that all the tips are brought into contact with the substrate simultaneously, i.e., all the tips are applying the same load. Under the hypothesis that all the cantilevers have the same spring constant, the load at each tip can be uniformed by aligning the array with the substrate and insuring that all the tips touch the sample simultaneously. This step is achieved by measuring each cantilever resistance (which depends on its temperature) as a function of the tip-sample distance, because the heat flux (and temperature) in each cantilever dramatically changes as the tip approaches, and then touches the sample. Accordingly, an optical leveling support was integrated with the AFM to tilt the substrate in order to level the tips. Figure 3.10 shows the details of the leveling process. When the array is unlevelled with the sample surface, the Resistance-Distance curve shows that the five tips touches the surface at different times. By leveling the array manually, the Resistance-Distance curve shows that the five tips touches the surface almost simultaneously.
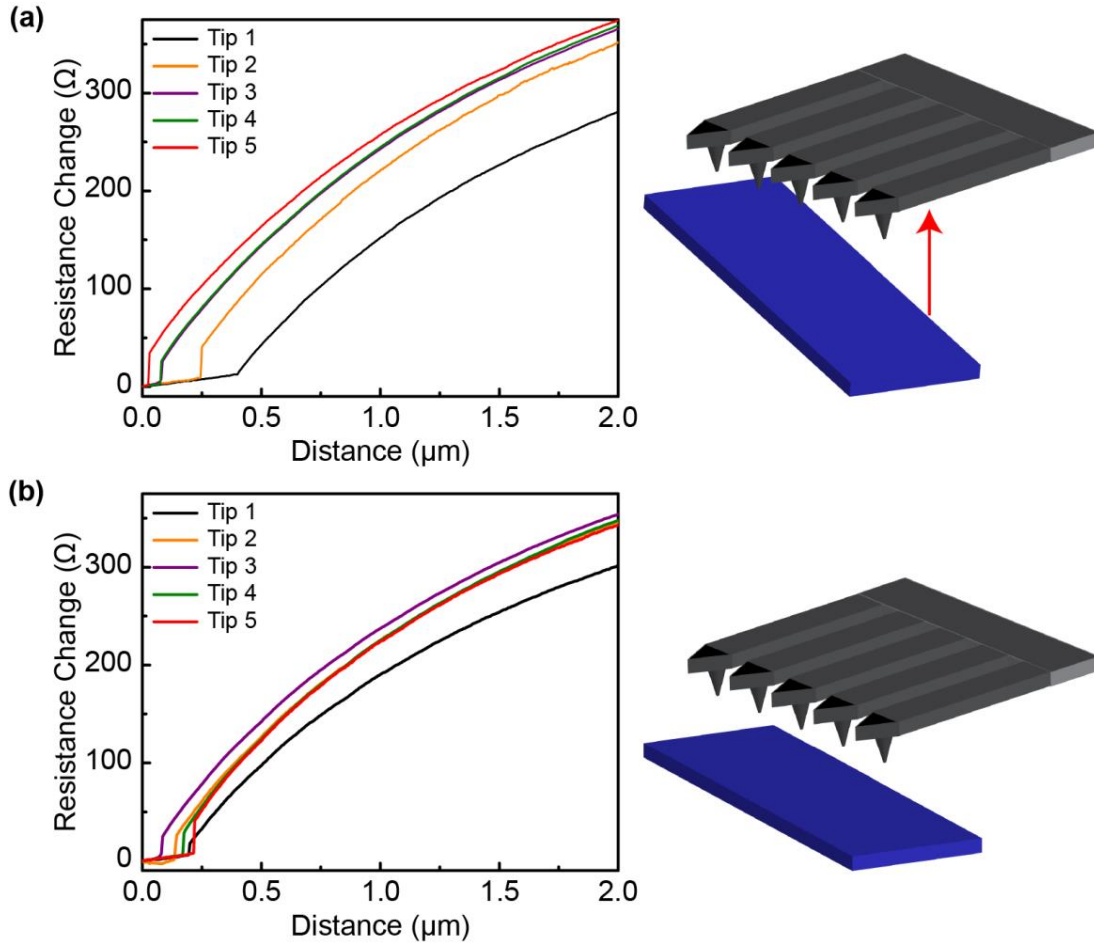
Fig. 3.10: Leveling of the array. (a) The array is unleveled with the sample surface. The Resistance-Distance curve shows that the five tips touch the surface at different times. (b) The array is levelled with the sample surface. The Risistance-Distance curve shows that the five tips touch the surface almost simultaneously [71].

CHAPTER 4

EXPERIMENTAL RESULTS

4.1 Parallelization of TCNL with a Tip Array

One of the most pressing technological challenges in the development of next generation nanoscale devices is the rapid, parallel, precise and robust fabrication of nanostructures. Here, we demonstrate the possibility to parallelize thermochemical nanolithography (TCNL) by employing five nano-tips for the fabrication of conjugated polymer nanostructures and graphene-based nanoribbons. The same array is used in situ to write and image microstructures, nanowires, and complex patterns of a conjugate luminescent semiconducting polymer, as well as conductive nanoribbons of reduced graphene oxide. Resolution down to sub-50 nm over areas of 500 mm and parallel complex 3D-patterning are demonstrated.

Figure 4.1 (a) depicts a cartoon of a thermal tip array containing five cantilevers with the corresponding nano-tips, spaced about 110 mm each other. For convenience, we label the tips 1 through 5. Each cantilever in the array [85], is joule-heated as previously reported in literature for single cantilevers [86], and it is individually addressable with a voltage bias, which is used to control the current flowing in the cantilever to achieve the joule-heating at the resistive tip. Recent experiments [85] show that these probes arrays can image surfaces with 0.6 nm vertical resolution, and can be used for thermomechanical lithography to pattern topographic variations into a fluorocarbon film.
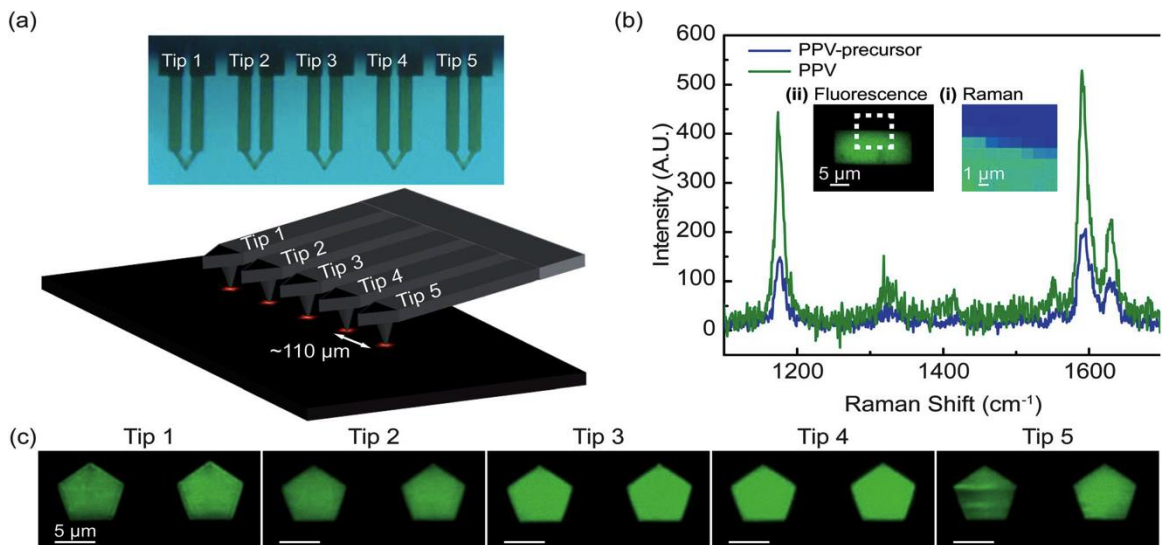
Fig. 4.1: (a) Optical Image and cartoon of the five thermal cantilevers and tips array for parallel TCNL. (b) Raman spectrum of PPV precursor (blue) and a TCNL produced pattern of PPV (green). In the inset we show the corresponding Raman image (I) and fluorescence image (II) of the precursor film and PPV pattern. (c) Fluorescence image of five PPV pentagonal double-patterns produced by the TCNL array and consisting each of two pentagons produced with two different temperatures [71].

To insure that the sample surface is parallel with the array we have used an optical leveling device onto which the sample is mounted. The conventional AFM optical feedback is present only for one cantilever, therefore we used the thermal interaction between the cantilevers and the sample to align the other cantilevers/tips in the array.

Figure 4.1 (b) and (c) show the results of a TCNL tip array to locally convert a precursor film of poly-p-xylene tetrahydrothiophenium chlorideintopoly (p-phenylene vinylene) (PPV). When heated with a hot tip, this precursor film has been shown to dissociate a side group and form PPV, a photo-luminescent semi-conducting organic polymer. We dropped-cast a PPV-precursor film on a Si substrate, we then leveled the array with the film surface and performed TCNL patterning of the film. To confirm the chemical conversion of the precursor film into PPV, we used Raman spectroscopy to detect the chemical change. Fig. 4.1b shows the Raman spectroscopy signal while mapping the precursor area (blue) and the PPV patterns (green). The Raman spectra are consistent with the chemical transformation of the precursor material in PPV. The measured changes in the Raman spectra after the precursor-PPV conversion have been described in Chapter 2. Briefly, the most distinctive characteristics of the Raman spectra after the complete conversion of the precursor film into PPV is the large intensity enhancement of the peaks at the 1178 and 1594 cm^{-1}, which can be attributed to a density increase in the polymer film due to a volume contraction.

The parallel writing capability of the TCNL array is then demonstrated in Fig. 4.1c, where we show five almost identical fluorescent images of two PPV pentagons produced with the five tips array. Each tip was used to write two PPV pentagons with two different temperatures (T1 and T2), at a linear speed per tip of 10 mm s^{-1}. The images were taken

with an epi-fluorescent microscope at an excitation of 488 and emission filter centered around 535 nm; this excitation/emission filters are consistent with the photo luminescent spectrum of PPV. As the heater temperature increases moving from the first to the second pentagon in all the five tips patterns, it is possible to observe an increase in the fluorescence intensity signal consistent with an increased amount of precursor that becomes PPV. We note that the five double-patterns are not completely identical. This is due to the fact that the tips are not perfectly aligned and therefore they are contacting the precursor film at different loads. A way to overcome and control this problem is to calibrate and control the heat provided to each tip individually, in order to guarantee the same amount of heat transferred at the tip-sample contact.

Having demonstrated the ability to convert the precursor film to PPV, we performed a series of experiments (see Fig. 4.2) to demonstrate the ability of the array to perform TCNL with nanoscale resolution. We wrote a set of PPV lines with eight increasing temperatures from left to right for each tip. For this experiment, the surfaces were spun cast instead of drop cast. Figure 4.2 (a) shows fluorescent images, each representing eight PPV wires written by each tip with increasing temperature; again we observe that as the temperature is increased (left to right) more of the precursor undergoes the transformation in PPV.
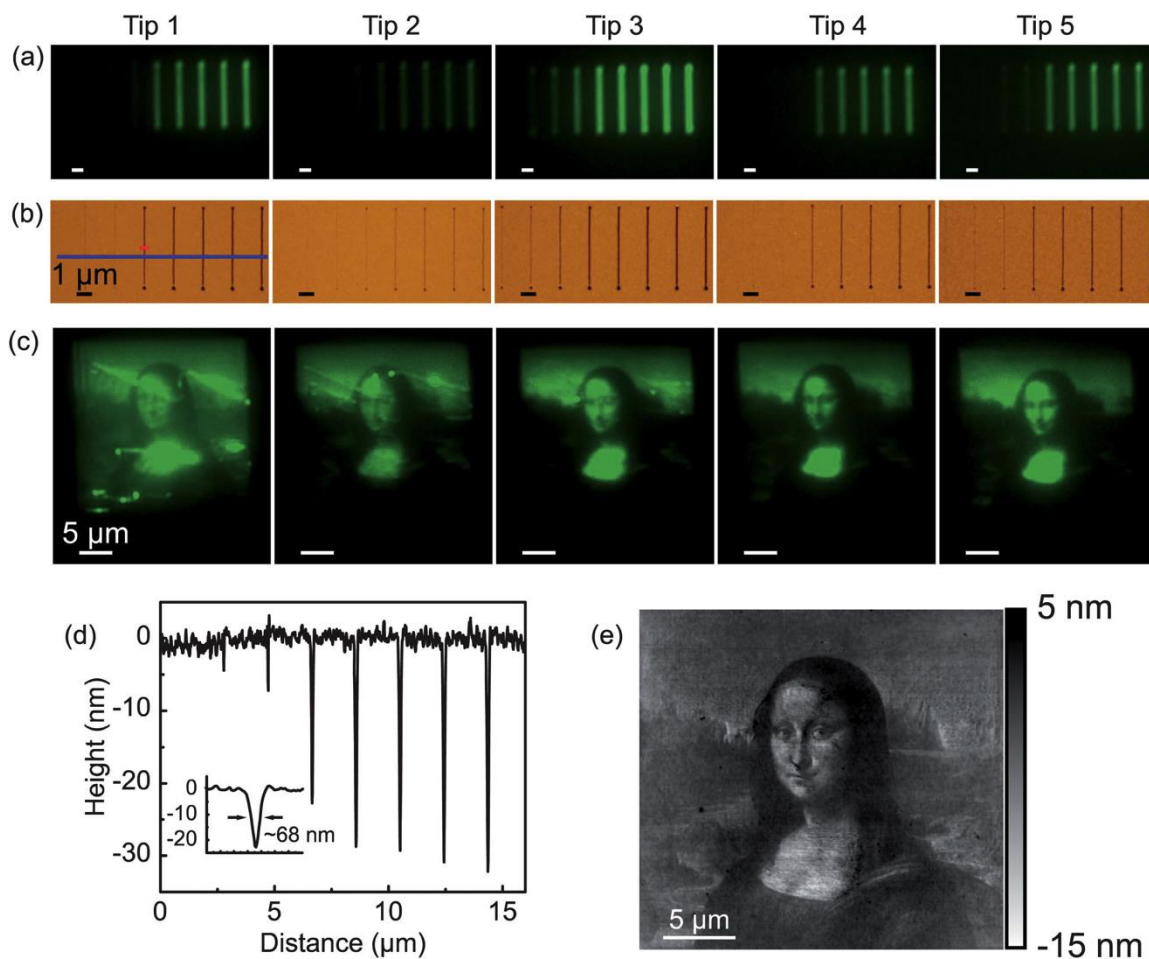
Fig. 4.2: (a) Five fluorescence images of a series of PPV nanowires written with increasing (left to right) tip temperature, and reproduced five times by using the five tips array. (b) Corresponding AFM topography image of the same PPV wires. (c) Five fluorescence images of a PPV Mona Lisa obtained by using the five tips array. The fluorescence contrast in each Mona Lisa was produced by controlling and varying the temperature of the tips during writing. (d) Topographic cross section of the PPV nanowires produced by tip 1, as shown in (b). (e) AFM topography image of one PPV Mona Lisa image [71].

Figure 4.2 (b) shows the corresponding AFM topography images for the wires produced by each tip. We show in Fig. 4.2 (c) five fluorescence images of five Mona Lisa PPV structures produced by a TCNL array on a PPV precursor films. The green color contrast has been adjusted individually for each Mona Lisa picture. As before, we remark that the parallelization is not perfect, however it can be substantially improved by programming the temperature (voltage) of each cantilever independently. To demonstrate the level of TCNL control on chemistry and topography, we show in Fig. 4.2 (d) a cross-section of the topography image of the PPV wires produced by tip 1, clearly confirming the fact that by increasing the tip temperature (left to right) more precursor material is converted in PPV and therefore the resulting indented PPV pattern/wire is deeper. The inset of Fig. 4.2 (d) shows a zoom-in of one of the lines, presenting a full width at half maximum of about 68 nm. This result shows that TCNL arrays can produce sub-100 nm lines over distances of 500 mm. The cross section in Fig. 4.2 (d) shows that by increasing the tip temperature not only more precursor undergoes a chemical change, but also the topography (depth of the indent) can be accurately controlled. This high level of topographical control is demonstrated in Fig. 4.2 (e) where we report the AFM image of a PPV Mona Lisa pattern.

Finally, the versatility of TCNL arrays is demonstrated by using the very same array used for writing PPV luminescent nanowires and complex topography patterns (Fig. 4.1 and 4.2) also to write conductive nanowires of reduced graphene oxide. The writing process is demonstrated in Fig. 4.3. Each tip creates four zig-zag patterns with an increasing voltage from 9.0 V to 10.5 V.
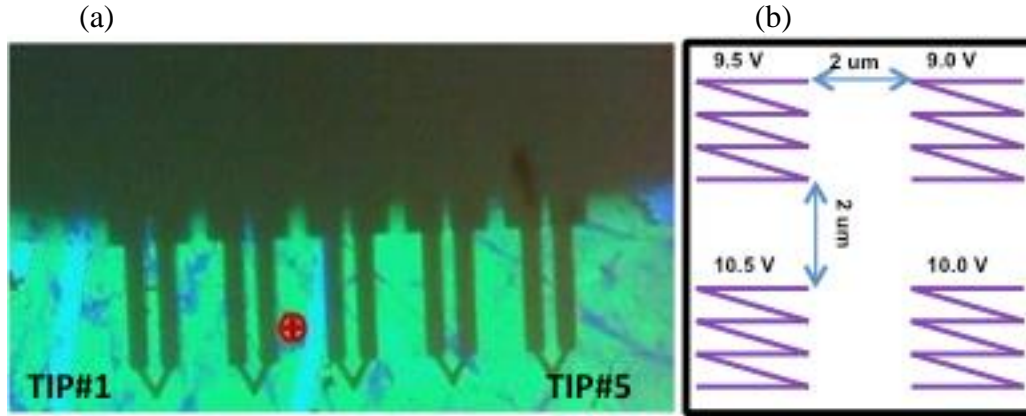
Fig. 4.3: (a) Optical view of the tip array above the GO sample. (b) A cartoon of the nanostructures that each tip made at a range of voltages, 9.0 – 10.5 V.

TCNL can locally reduce highly insulating graphene oxide (GO) to a conductive graphene-like material (here called reduced GO, rGO), as shown in Fig. 4.4. The TCNL array was therefore used to write graphene-like conductive zig-zag nanostructures in a highly insulating graphene oxide thin film deposited on silicon oxide. Schematic of the experiment is shown in Fig. 4.4 (a), where we use each of the five tips to pattern four zig-zag lines at four different temperatures, increasing from top left corner clockwise. Figure 4.4 (b) shows a current sensing-AFM (CSAFM) image of the current flowing between the AFM tip and the GO sample, where the image is focused on the patterns made by tip 1. The reduced GO zig-zag lines conduct more current; this is indicative of the higher conductivity associated with reduced graphene oxide. Figure 4.4 (c) shows Kelvin Probe Force Microscopy (KPFM) images of the patterns made by tip 1 and tip 3. These images show a change (between GO and reduced GO lines) in the surface contact potential of 20 mV. The surface contact potential is a measure of the work-function difference between the sample and the tip. The change in conductivity coupled with the change in the surface

68

contact potential is a strong indication that we have successfully reduced graphene oxide with parallel TCNL.

Figure 4.5 shows more data regarding the reduction of GO created by tip 1. We also show a high-resolution image of the zig-zag lines indicating a line half maximum width of 50 nm. The topography images of the zig-zag lines created by the other tips are shown in Fig. 4.6.
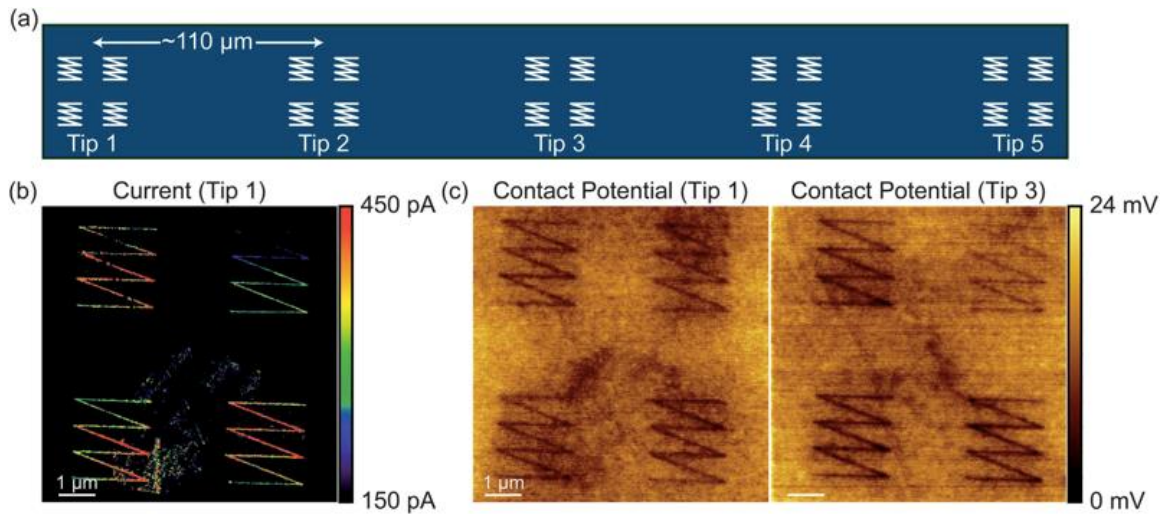
Fig. 4.4: Parallel TCNL of reduced GO nanostructures. (a) Schematic of parallel TCNL used to produce conductive rGO nanostructures in an insulating GO film. (b) Current and (c) Kelvin probe AFM contact potential difference for rGO nanostructures made by tip 1 and tip 3 [71].

(a) Topography

30.0 nm

1 um

-5.0 nm

(b) Topography

19.5 nm

~50 nm

150n
m

0.5 nm

(c) Friction

70.0 mV

1 um

15.0 mV
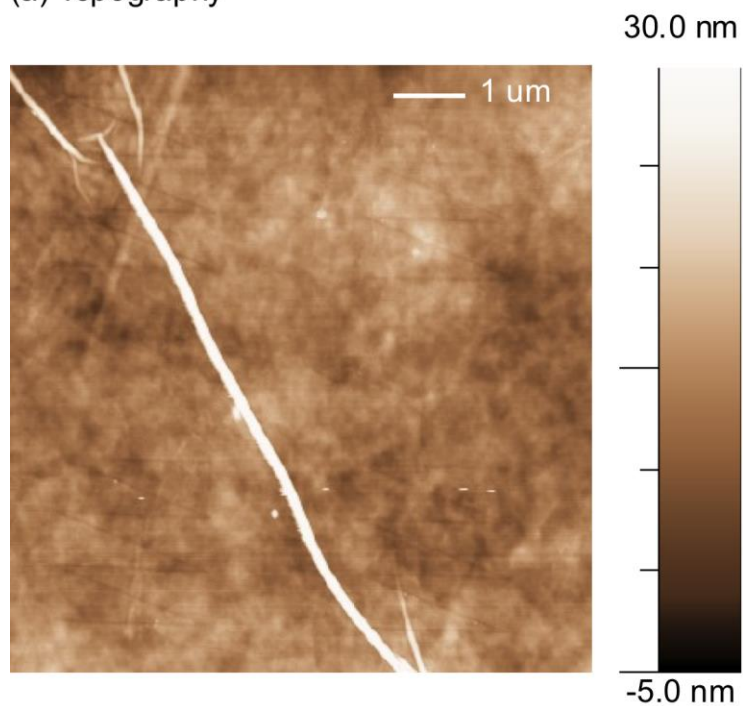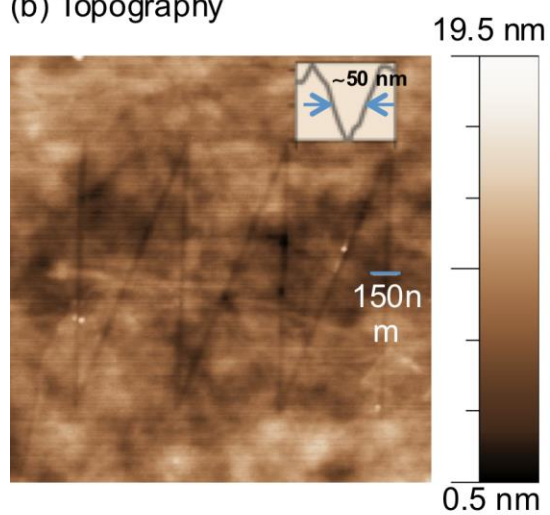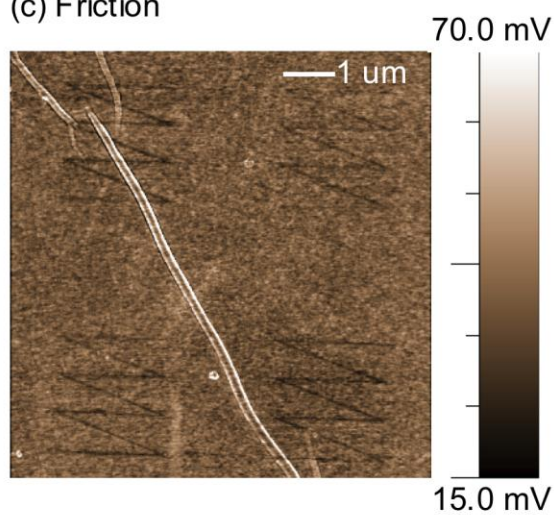
Fig. 4.5: (a) Topography of the four rGO zig-zag nanostructures made by tip 1. (b) Zoomed in topography of the bottom left nanostructure in (a). (c) Friction of the four nanostructures made by tip 1.
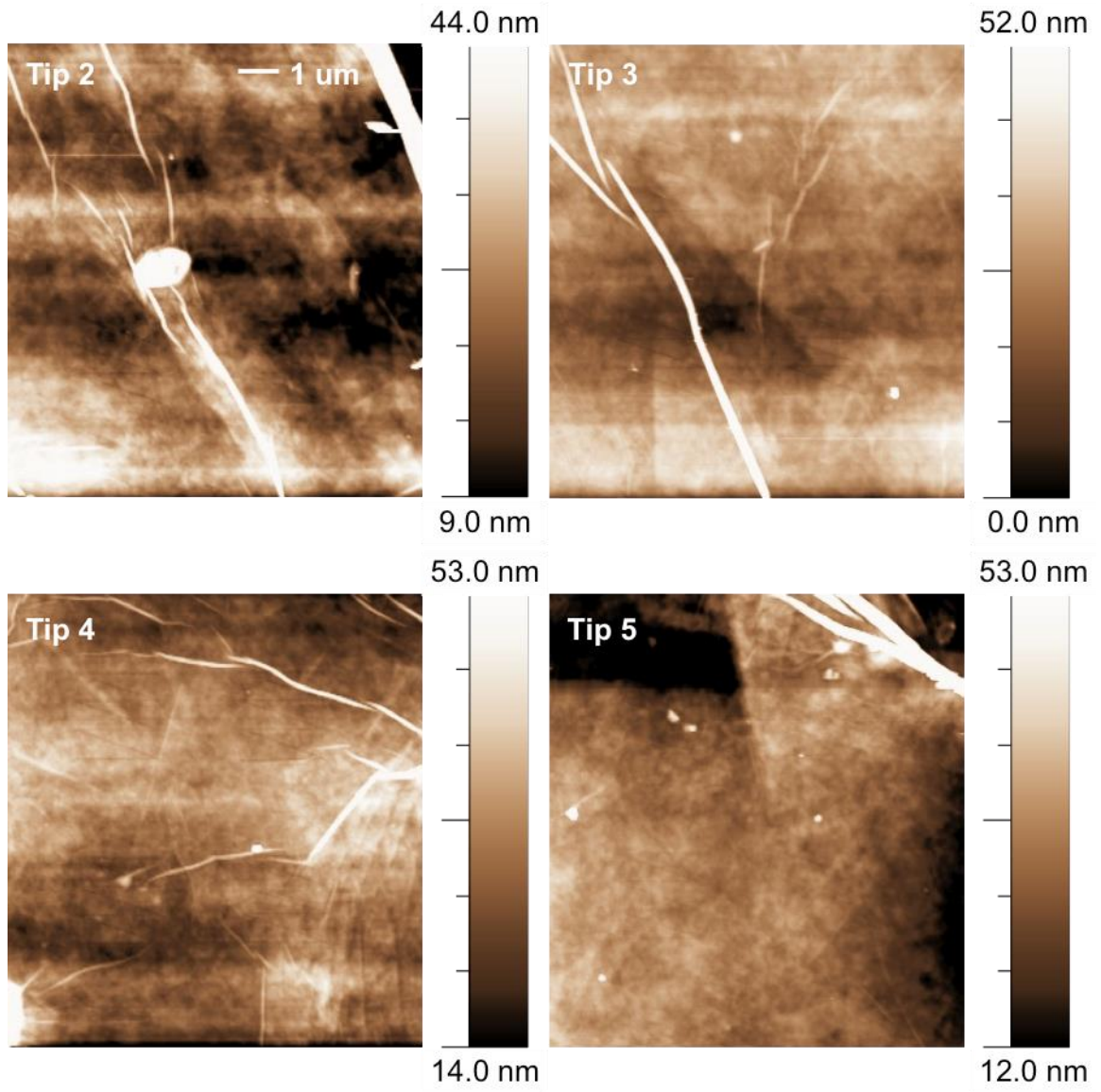
Fig. 4.6: Topography of rGO nanostructures made by tip2, 3, 4, and 5.

4.2 Reduced Graphene Fluoride

As discussed in chapter 2, rGF nanoribbons have great advantages over GNRs created by other methods, such as EBL and unzipping graphene nanotubes. However, there lacks an efficient way to predict the reduction amount from TCNL, which will affect the electronic properties of the GNRs significantly. When GF is reduced to graphene, the AFM friction images show that reduced graphene has a lower friction compared to GF, and the friction depends on TCNL parameters. In this research, we use the reduction in friction to indicate the amount of reduction in GF, and we seek to derive the activation energy for the GF reduction reaction from first order chemical kinetics equation, thus offering a valid method to predict the reduction amount.

Fluorinated CVD graphene samples are used for our experiments. During TCNL, a heated tip come into contact and GF is locally reduced. Figure 4.7 contains the AFM topography and friction images of rGF patterns created with different load. From the topography image, the height of the patterned area decreased by about 1nm after TCNL, as a result of the removal of the fluorine. In the friction image, friction decreased and the decreased amount increased as the load increased.
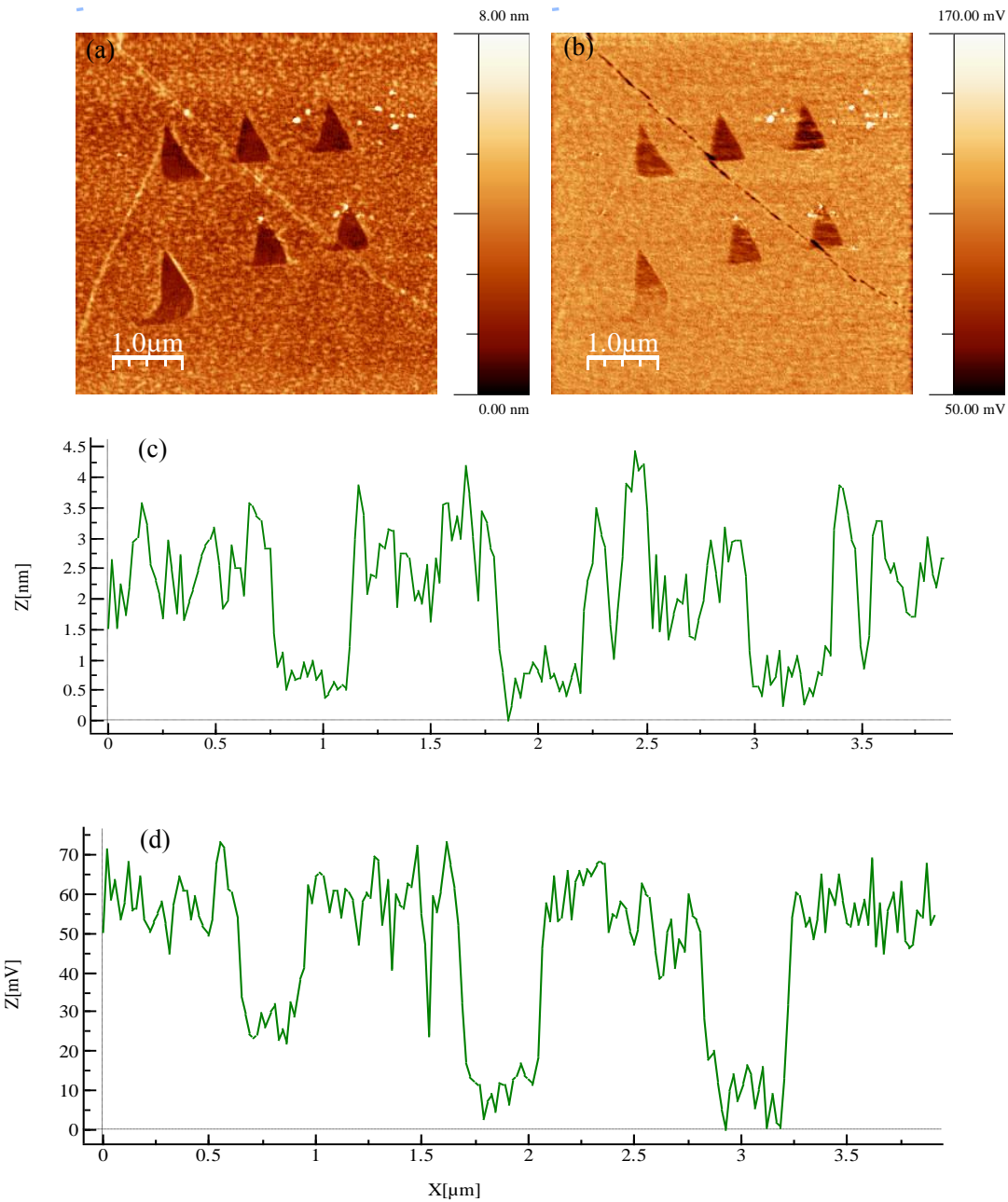
Fig. 4.7: AFM topography (a) and friction (b) images of rGF patterns. The patterns were created at a constant tip speed of 0.2 μm/s, a constant heater temperature of 950 °C and an increasing force setpoint from 0.2 V to 1.7 V with a step of 0.3 V (the bottom left has the lowest setpoint and the top right has the highest setpoint). (c) and (d) are the cross sections of (a) and (b).
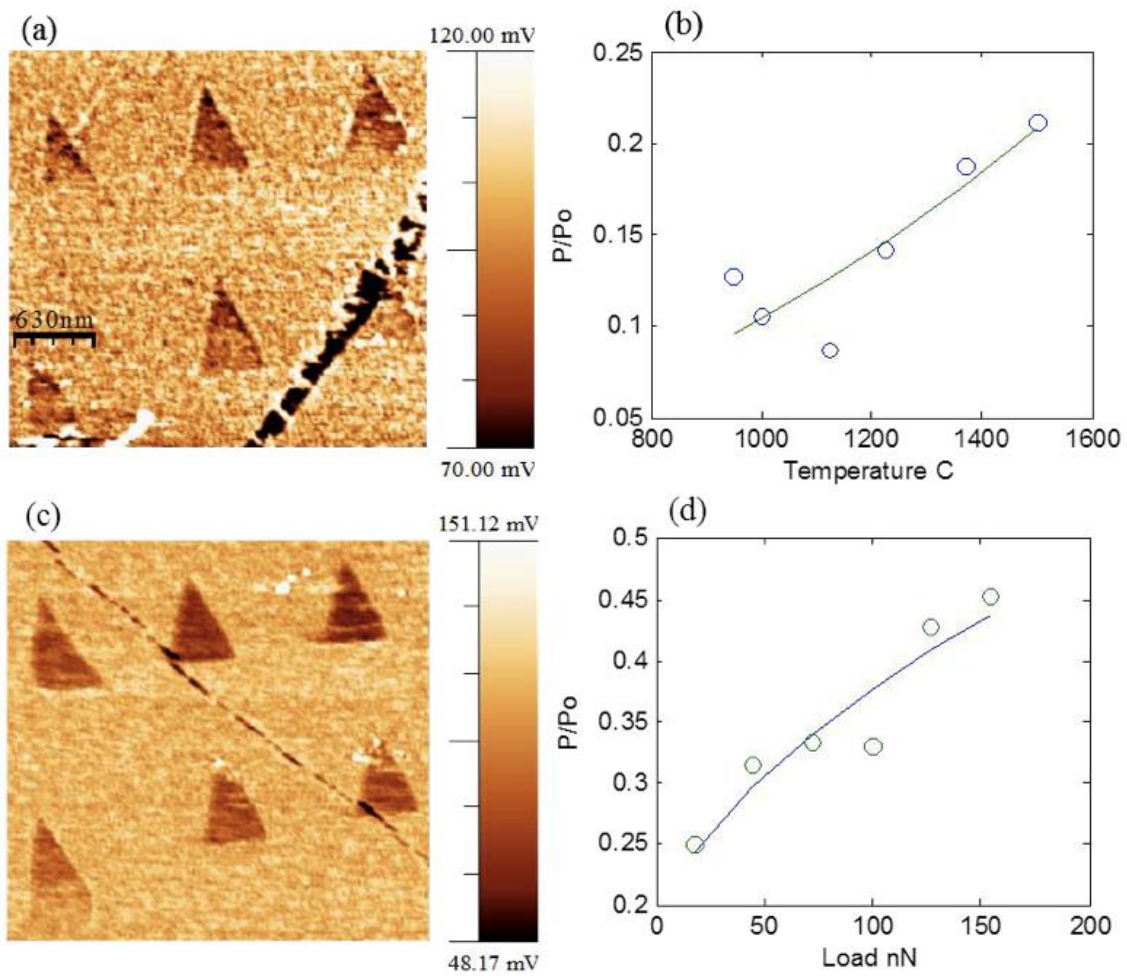
Fig. 4.8: AFM friction images of the patterns created with varying heater temperature (a) and varying load (c). (b) The fitting for friction measured in (a). (d) The fitting for friction measured in (c).

74

Figure 4.8 (a) shows the experimental results obtained when the heater temperature increases from 950 °C to 1500 °C, while the load was constant ($\sim$ 180 nN). The reduced amount in friction relates to the fluorine reduction and the reduction can be quantified by using first order chemical kinetics:

$$\frac{dP}{dt} = k(P_0 - P), \qquad k = A \cdot \exp\left(\frac{-E_A}{RT}\right) \tag{4.1}$$

where t is time, P is the concentration of recovered graphene and P_0 is the maximum possible concentration of recovered graphene, k is the rate constant and T is the temperature at interface. E_A is the activation energy for the reaction and A is the Arrhenius constant. E_A represents the energy barrier hindering the dissociation of the fluorine bonded to graphene lattice, and A is the maximum rate of reaction.

From Eq. 4.1, we obtain the concentration of recovered graphene:

$$P = P_0[1 - \exp(-k \cdot t_d)] \tag{4.2}$$

where t_d is the tip dwell time. With a tip moving speed v and tip radius of about 20 nm, the estimation of t_d is:

$$t_d = \frac{R}{v} \tag{4.3}$$

Figure 4.8 (b) is the fitting curve obtained from Eq. 4.2 and Eq. 4.3, where E_A and A are free parameters. The obtained value of E_A is 20 ± 6 kJ/mol, which is equal to 0.21 ± 0.06 eV. The obtained value of A is 865 ± 1522 s^{-1}.

The experiments shown in Fig. 4.8 (c) are performed with the load increasing from 18 nN to 154 nN, while the heater temperature remains constant (950 °C). Figure 4.8 (d) is the fitting curve and the obtained value of E_A is 11 ± 2 kJ/mol, which is equal to 0.11 ± 0.02 eV. The obtained value of A is 211.1 ± 152.7 s^{-1}.

4.3 Local Anodic Oxidation (LAO) Lithography

AFM-based local anodic lithography has been used to fabricate nanostructures on semiconductor surfaces [99, 100]. During LAO lithography, a DC bias is applied to the sample while the conductive tip is grounded. If there is a negative tip-sample bias, the sample surface is oxidized as the anode. Recent experimental results [27] have shown that graphene can be patterned by LAO lithography and the Raman data of the patterned regions are similar to those of graphene oxide prepared by modified Hummers method [63]. The oxidized graphene patterns are highly insulating compared to pristine graphene.

The properties of oxidized patterns on EG by LAO lithography greatly depend on the lithography parameters such as load, speed and DC bias applied. In this research we study how the lithography parameters affect the oxidized patterns. By optimizing the experimental parameters, we seek to create narrow stripes with width below 15 nm across graphene side wall ribbons to study the electron tunneling effect in these ribbons. Isolated GNRs can also be created through LAO lithography, through the oxidation of selected area on EG, leaving a narrow ribbon channel unoxidized.

Therefore, LAO lithography offers an alternative way to produce isolated GNRs. In our work, LAO patterns are created by applying a negative tip-sample bias with a Pt/Ir coated tip while scanning, and the patterns are characterized by taking AFM images afterwards. A Veeco Multimode AFM was used for the LAO lithography. LAO patterns show an increase in height in topography images, as a result of adding oxygen groups to the carbon lattice. An increase in friction is also observed, since graphene oxide has a higher friction than graphene. These changes are used to identify and characterize the

LAO patterns. The widths of the LAO lines greatly depend on tip moving speed, setpoint and the bias.
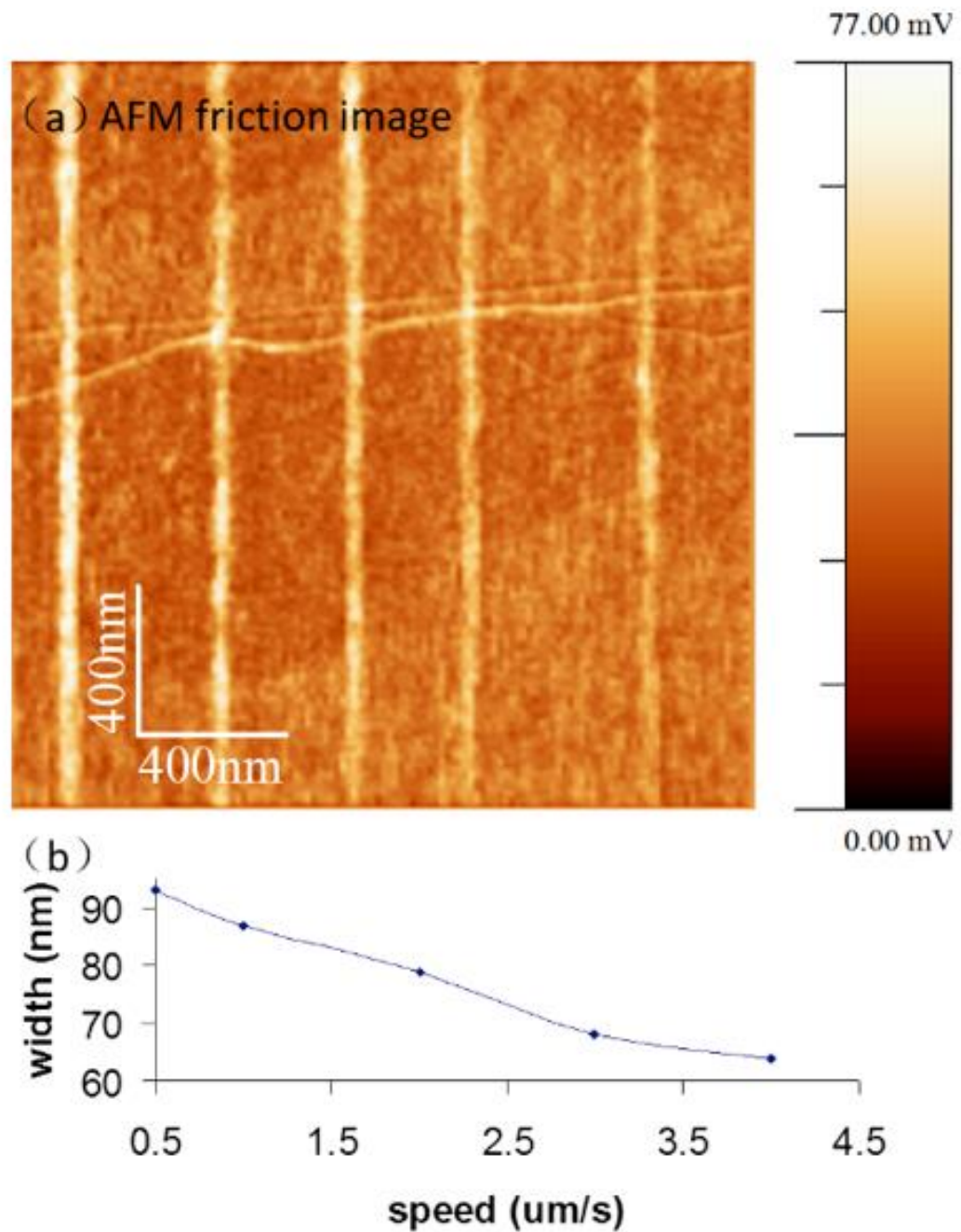
Fig. 4.9: LAO patterns with different widths. (a) Topography image of the LAO patterns. (b) Average widths of the patterns created with different speeds. During LAO lithography, the setpoint is 0.8 V and the bias is -8V constantly.

Figure 4.9 contains the AFM friction image of LAO lines with different widths. The tip-sample bias is -8V constantly, and the tip moving speed is different for each line. As shown in Fig. 4.9 (b), the average width decreased from 93 nm to 64 nm, as the scan speed increased from 0.5 μm/s to 4 μm/s.

Figure 4.10 (a) and (b) show the topography and friction images of some additional LAO patterns created on an EG sample with different experimental parameters, including lines and a solid square. By adding an LAO line close to a square pattern, an isolated graphene stipe with a width below 30 nm was created, as shown in the zoomed-in image in (b). In the zoomed in image, a GNR (the dark color part) was created between oxidized graphene (the light color part). The DC bias was -8V and the tip setpoint was 0.8 V for all the LAO patterns in (a). Figure 4.10 (c) and (d) are the zoomed-in images of LAO lines with width of 80 nm and 100 nm, corresponding to the top and bottom lines in (a), with scan speed of 7 μm/s and 1.5 μm/s respectively. For the future research, we seek to create isolated GNRs with a narrower width by reducing the separation of two LAO lines.

To study the electronic transport properties of the LAO patterns, we also performed LAO lithography on sidewall graphene ribbons. Figure 4.11 (a) and (b) show an LAO stripe with width of ~700 nm created on a sidewall ribbon. An increase in friction shows that LAO lithography has successfully oxidized the graphene ribbon. The IV curves before and after LAO lithography are shown in Fig. 4.11 (c) and (d). Before LAO lithography, the IV curve is ohmic with a resistance of 166 kΩ. The IV curve becomes nonlinear after LAO lithography and the resistance is ~2MΩ measured at 1.5 V. These results indicate that we can use LAO lithography to modify electron transport behaviors in the graphene sidewall ribbons.
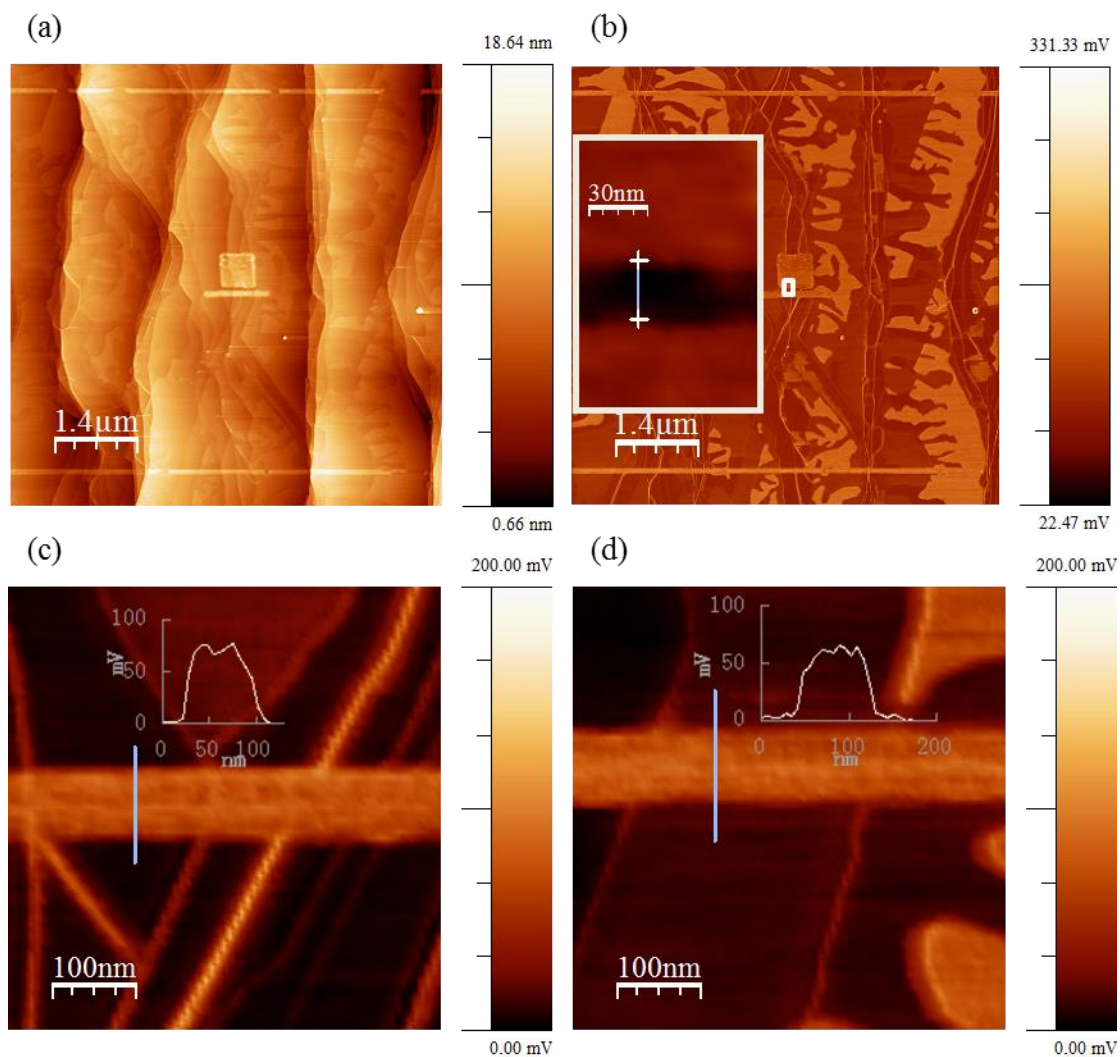
Fig. 4.10: (a) AFM topography image of LAO oxidized graphene patterns created with different lithography parameters. (b) AFM friction image of the LAO patterns. The inserted image is a zoomed-in view of the conductive channel with a width of ~30 nm. Zoomed-in view of LAO patterns with a width of ~80 nm (c) and a width of ~100 nm (d).
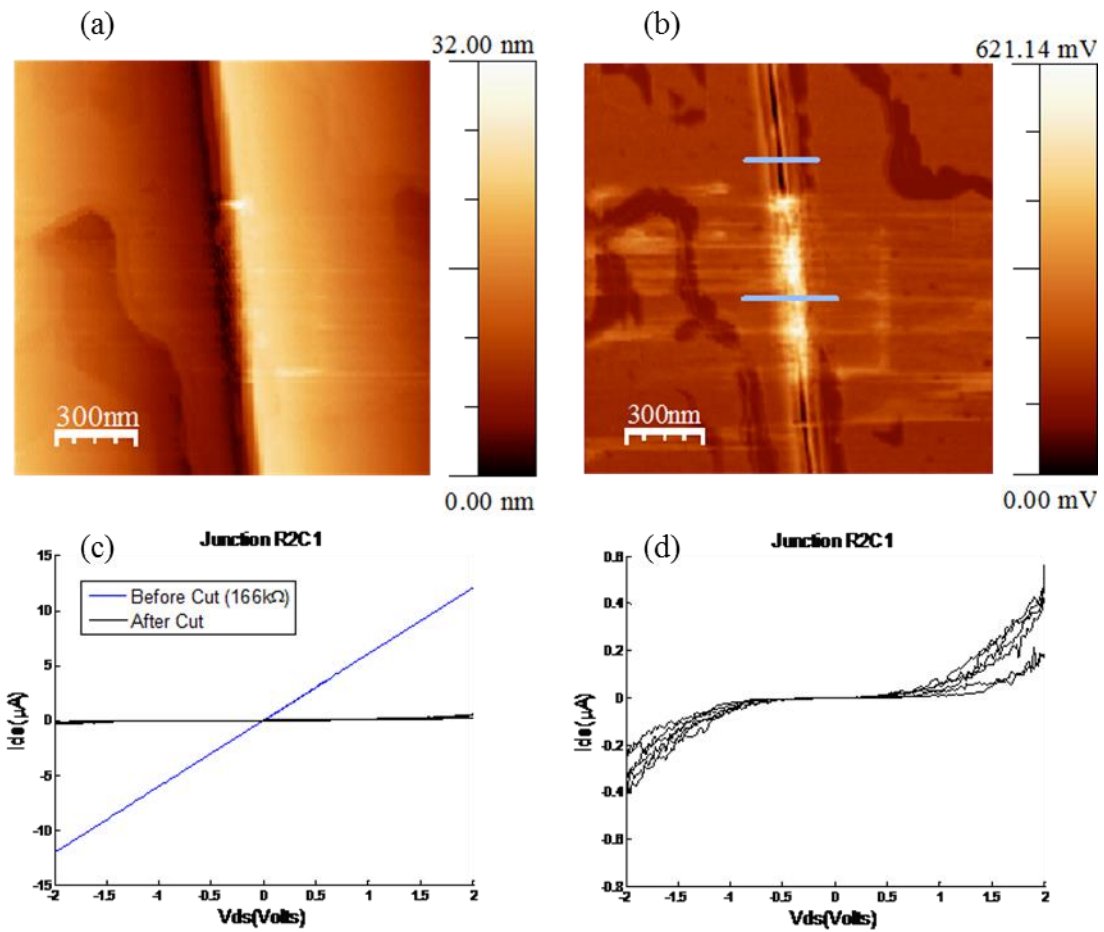
Fig. 4.11: (a) AFM topography and (b) friction images of a graphene sidewall ribbon after LAO lithography. A graphene-GO-graphene junction is formed after LAO lithography. (c) IV curves of the sidewall ribbon before (blue) and after (black) LAO lithography. (d) Rescaled IV curve after LAO lithography.

AFM current imaging was used to further characterize the LAO patterns. Figure 4.12 contains AFM current images of a graphene sidewall ribbon before and after LAO lithography with -8V tip-sample bias. A gap with width of ~15 nm is observed after lithography.
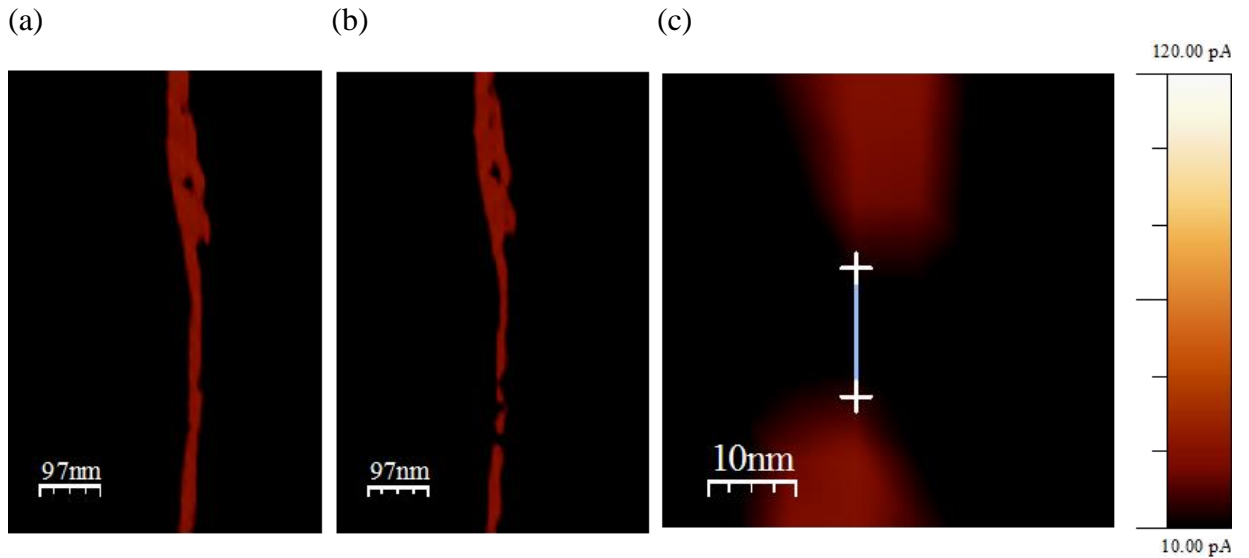
Fig. 4.12: (a) AFM current image of a graphene sidewall ribbon before LAO lithography. (b) AFM current image of the sidewall ribbon after LAO lithography. (c) Zoomed-in view of a ~15 nm wide gap.

4.4 Imaging Thermal Conductivity with Nanoscale Resolution

Using a Scanning Spin Probe

The ability to probe nanoscale heat flow in a material is often limited by lack of spatial resolution. Here, we use a diamond-nanocrystal-hosted nitrogen-vacancy center attached to the apex of a silicon thermal tip as a local temperature sensor. We apply an electrical current to heat up the tip and rely on the nitrogen vacancy to monitor the thermal changes the tip experiences as it is brought into contact with surfaces of varying thermal conductivity. By combining atomic force and confocal microscopy, we image phantom microstructures with nanoscale resolution, and attain excellent agreement between the thermal conductivity and topographic maps. Our approach promises multiple applications, from the investigation of phonon dynamics in nanostructures to the characterization of heterogeneous phase transitions and chemical reactions in various solid-state systems.

Here we articulate atomic force and confocal microscopy to demonstrate an alternate route to thermal conductivity imaging with nanoscale resolution. Our approach leverages on the unique properties of the nitrogen-vacancy (NV) center in diamond, a spin-1 defect that can be individually initialized and readout with the aid of optical and microwave (mw) pulses [99]. Thermal changes in the NV vicinity can be detected by monitoring the NV spin resonance frequency, which strongly depends on the system temperature [100-102]. In our experiments, we use a diamond-nanocrystal-hosted NV as a nanoscale probe attached to a sharp tip of a thermal probe. The thermal probe is used to warm the tip to a predefined temperature above ambient.
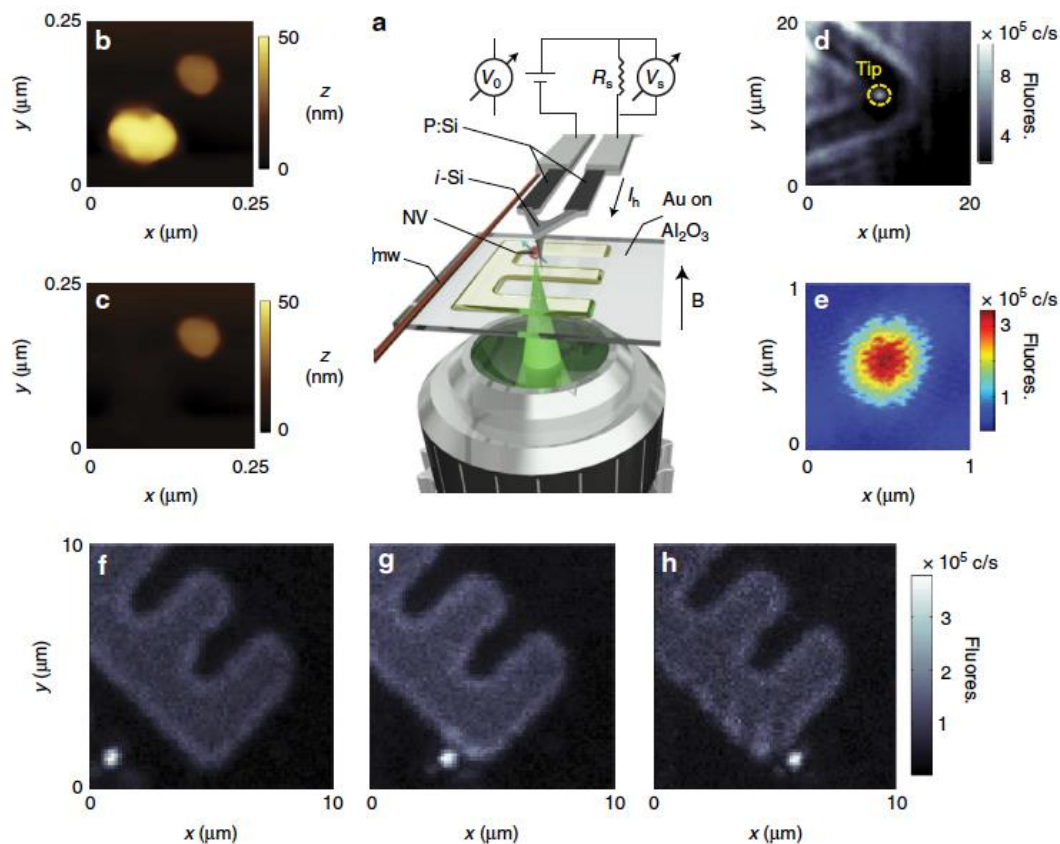
Fig. 4.13: Approach to NV-enabled thermal scanning microscopy. (a) Schematics of our experimental setup. A high-NA objective excites and collects the fluorescence emitted by a diamond-nanocrystal-hosted NV attached to a thermal cantilever. Our experiments are carried out in the presence of a magnetic field B along the direction normal to the sample. (b) AFM image of two diamond nanoparticles on a glass substrate. (c) Same as before but after firmly scanning the tip on the larger nanocrystal. Comparison with b shows the particle has been removed from the substrate. (d) Fluorescence image of the cantilever end and tip. Light from the tip-attached nanocrystal can be clearly separated from the background (yellow circle). (e) Zoomed confocal image of the NV center in d. (f–h) Sequential fluorescence images of the nanoparticle-hosted NV as the AFM scans a micro-structured surface [97].

A more detailed description of our working geometry is presented in Fig. 4.13: Our system articulates an AFM and a confocal microscope in a two-sided geometry. A thermal cantilever servers as the heater. We mount the colour center onto the tip apex by firmly scanning the AFM probe on a sample of disperse diamond nanocrystals loosely bound to a glass substrate. Van der Waals forces keep the nanoparticle securely attached to the tip surface; images of a sample diamond crystal before and after AFM grafting are shown in Fig. 4.4.1b–e. We use a high-numerical-aperture objective facing the AFM tip to excite and collect fluorescence from the nanoparticle. Figure 1f–h shows successive confocal images recording the NV center position as we displace the tip over a (semi) transparent substrate.

In our experiments, we apply a voltage difference between the arms of the cantilever to set the heater temperature T_h, which we then determine by monitoring the NV response to mw. Figure 4.14 (a) shows the optically detected electron spin resonance spectra at three different heater temperature T_h, each exhibiting the characteristic NV fluorescence dips near 2.8 MHz. The nanoparticle temperature T_t follows from the known thermal dependence of the NV resonance frequency υ_{NV} (Fig. 4.14b).

Interestingly, we find that more than one diamond particle can be attached to the AFM probe if, once loaded, the tip is brought into contact with another NV-hosting diamond crystal. This is shown in Fig. 4.14 c, where we attach up to six nanocrystals upon repeated grafting. We find that the diamond particles decorate the tip apex more or less concentrically (Fig. 4.14 c). Grafting a new particle (ND1, bright spot in the figure) pushes the rest farther deep and into the cantilever body allowing us to optically separate most NVs. Given the random orientation of each particle, we discriminate between NVs
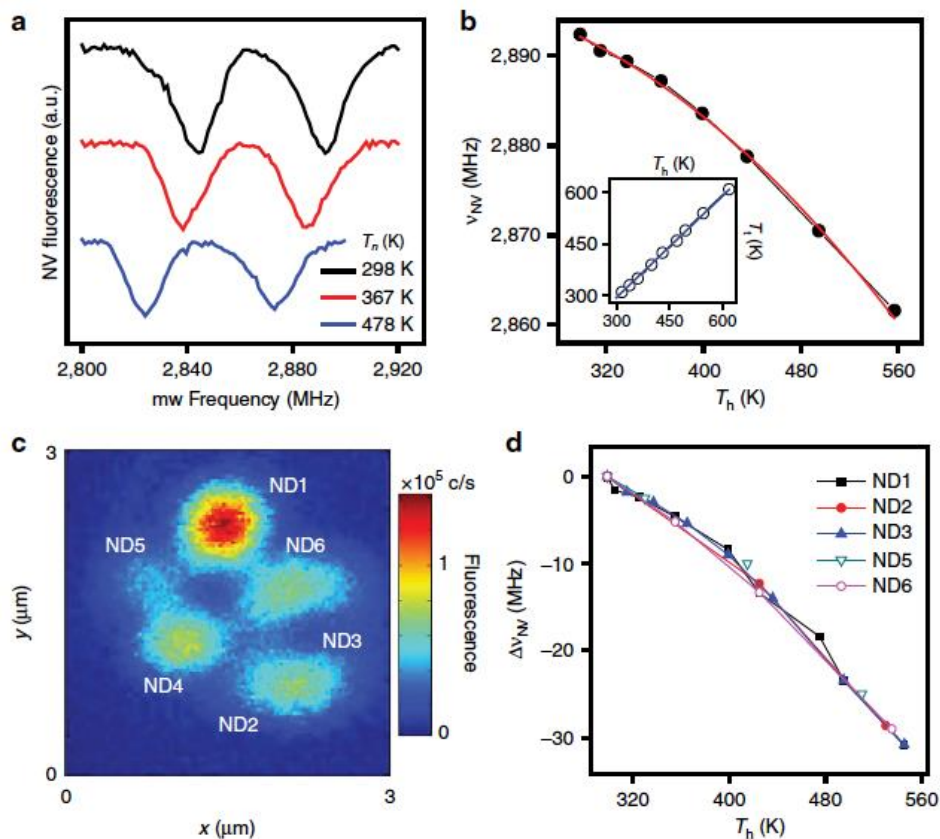
Fig. 4.14: NV-spin-assisted sensing of the AFM tip temperature. (a) Optically detected magnetic resonance spectra of an NV center at three heater temperatures T_h. The right (left) dip corresponds to the $m_s=0\leftrightarrow m_s=+1$ transition (the $m_s=0\leftrightarrow m_s=-1$ transition) between the levels of the NV ground-state spin triplet. (b) Temperature dependence of the $m_s=0\leftrightarrow m_s=+1$ transition frequency ν_{nv}; the red trace is a quadratic fit. The inset shows the diamond nanoparticle temperature T_t using the known relation with the NV resonance frequency as a function of T_h for a tip exposed to ambient. Comparison with the graph diagonal (solid blue trace) indicates that both coincide within experimental error. (c) Confocal image of the AFM cantilever in the vicinity of the tip after grafting multiple NV-hosting nanocrystals. (d) Frequency shift relative to room temperature for each of the nanocrystals imaged in c [97].

close to each other via the application of a small magnetic field. For a given applied voltage, we find identical frequency shifts Δv_{NV} in all NVs (Fig. 4.14 d), indicative of a consistent thermal contact between the tip and the spin probe.

Finally, high-resolution thermal conductivity imaging result is shown in Fig 4.15. We record the tip temperature as we scan an 18-nm-thick film pattern of gold on sapphire.
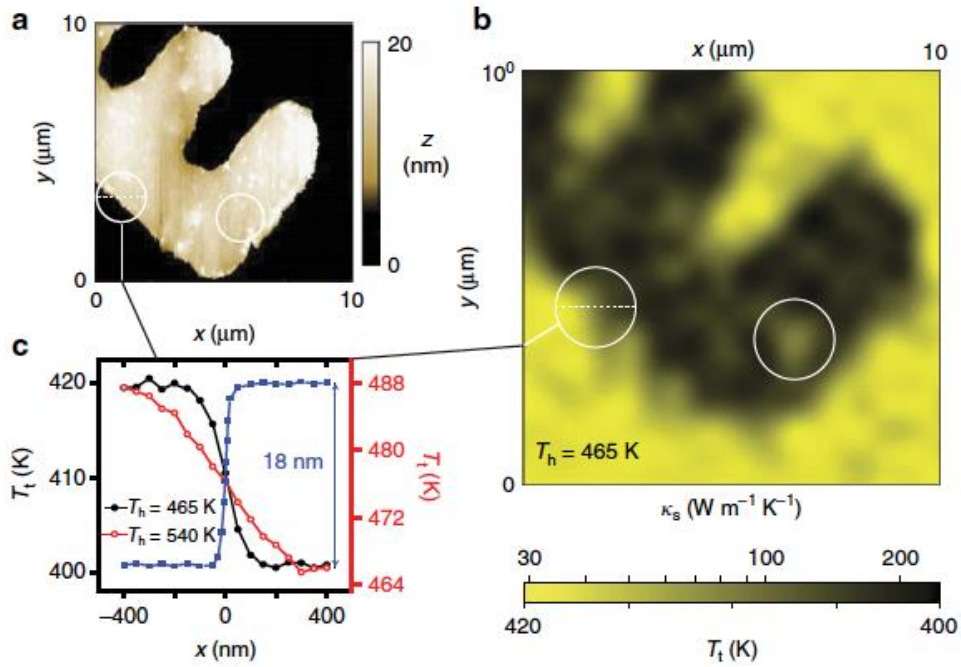
Fig. 4.15: High-resolution thermal conductivity imaging. (a) AFM topographic image of a 18-nm-thick gold pattern on sapphire. (b) NV-assisted thermal conductivity image of the same structure. The heater temperature T_h is 465 K. White circles in a and b indicate example patches of low (high) conductivity inside (outside) the gold structure that do not correlate with the substrate topography. (c) Measured tip temperature near the edge of the pattern at two heater temperatures, 465 K (full black circles, left vertical axis) and 540 K (empty red circles, right vertical axis). The topographic curve displaying the gold film edge as measured with the AFM (blue squares) is also present for reference [97].

CHAPTER 5

CONCLUSIONS AND PERSPECTIVES

We have presented the development of an advanced probe based lithography technique: thermochemical nanolithography (TCNL). We demonstrate the possibility to parallelize TCNL by creating nanoscale patterns with a tip array, containing five identical thermal cantilevers. The versatility of our technique is demonstrated by creating nanopatterns simultaneously on multiple surfaces, including graphene oxide and conjugated polymers. The main challenge to apply TCNL with a tip array is that the optical feedback can be used on only one tip. By level the tip array with the sample surface, it is possible to apply the same load on each tip, and thus creating identical patterns. The parallelization of TCNL can promisingly expand to larger arrays [98].

The second part of this thesis is about creating graphene nanoribbons from graphene fluoride. Graphene nanoribbons (GNRs) are essential building blocks for next generation electronic devices. However, there lacks an efficient and controllable method to fabricate smooth edged GNRs. Through TCNL, GNRs can be created with precision on insulating GF surfaces. To provide a solid prediction of the reduction amount, we derived the activation energy for the GF reduction reaction using the first order chemical kinetics equation.

In this thesis, we also performed local anodic oxidation (LAO) lithography on epitaxial graphene (EG) samples. Oxidized graphene patterns were created on EG samples and a GNR with a width below 30 nm was produced. To study the effect of LAO lithography on electron transport properties, we created oxidized stripes on sidewall graphene ribbons. Nonlinear IV curves were observed for the graphene-GO-graphene

junctions. With optimized parameters, it is possible to further decrease the width of the gap to study the electron tunneling effects in these sidewall graphene ribbons.

APPENDIX A

LITHOGRAPHY PROGRAM 1

```
clear all
clc
addpath('C:\Documents and Settings\Administrator\My
Documents\MATLAB\daq')
a=1;
while a   %type in suitable parameters
n=input('please type in the number of the sides of the shape: n=');
h=input('please type in the height of the shpae(um): h=');
rnum=input('please type in the number of rows:');
cnum=input('please type in the number of columns:');
rs=input('please type in the spacing between the rows (um):');
cs=input('please type in the spacing between the columns (um):');
vol=input('please enter the starting voltage (volts):');
deltav=input('please enter the voltage difference between elements
(volts):');
speed=input('please enter the tip speed (um/s):');
speed=speed/1000000; % change tip speed to the unit of m/s
spon=input('please type in the setpointwhen power is on:');
spoff=input('please type in the setpointwhen power is off:');
res0=input('please type in the resloution (256/512/1024):'); %pixel of
the scan range
R=2000;  % reference resistor

H=rnum*(h+rs); % the heigh to do TCNL
L=cnum*(h+cs); % the width to do TCNL
larger=max(H,L);
if larger<100
    a=0;
else
    'size is too large for scanner'
end
end

q=1;
while q<larger
    q=q*2;
end

larger=min(100,q);
scansize=larger/1000000;
SetScanTipSpeed(speed);
SetScanSize(scansize);
cf=res0/larger;  %pixel/micron
res0=cf*h;
res=round(res0);
x0=(larger-(cnum-1)*(h+cs))*cf/2;  %initial position
y0=(larger-(rnum-1)*(h+rs))*cf/2;
xy=xycordinates(n,h,cf);
B0=zeros(3,res*rnum*cnum);
i=1;
figure(1)
```

```
q=1;
for i=1:rnum  % i: row number
    y1=y0+(rnum-i)*(h+rs)*cf
    pause(2.0)
    j=1;
    for j=1:cnum % j: colume number

        x1=x0+(cnum-j)*(h+cs)*cf
        pause(1.5)
        '1';
        SetTipPosition(x1,y1);
        '2';
        WaitForStatusScanPixel(x1);
        WaitForStatusScanLine(y1);
        '3';
        x2=x1+xy(1,1); %left
        x2=round(x2)
        x3=x1-xy(1,1); %right
        x3=round(x3)
        y2=y1+xy(2,1);%y
        y2=round(y2)
        '4';
        SetTipPosition(x2,y2);
        '5'
        WaitForStatusScanPixel(x2);
        WaitForStatusScanLine(y2);
        '6'
        vv=(vol+deltav*((j-1)+(i-1)*cnum))/2;
        m=res*cnum*(i-1)+(j-1)*res+1;
        t=2;
        GenNUpdates('cDAQ1Mod8/ao0',0,10,1000,[vv,vv],10); %for single
tip (same circuit for tip5 from the tip array)
        pause(1)
        SetServoSetpoint(spon(q));
        for t=3:res
            x2=x1+xy(1,t); %left
            x2=round(x2);
            x3=x1-xy(1,t); %left
            x3=round(x3);
            y2=y1+xy(2,t); %y
            y2=round(y2);
SetTipPosition(x2,y2);
            WaitForStatusScanPixel(x2);
            WaitForStatusScanLine(y2);
            SetTipPosition(x3,y2);
            WaitForStatusScanPixel(x3);
            WaitForStatusScanLine(y2);
            A0=AcqNUpdates('cDAQ1Mod6/ai0',-10,10,20,5000,5);
            A0=sum(A0)/20;
            B0(1,m)=2000*(vv-A0)/A0*(A0/1000)^2;
            B0(2,m)=2*vv;
            B0(3,m)=2000*(vv-A0)/A0;
            subplot(1,2,1)
            plot(m,B0(1,m),'o')
            hold all
            subplot(1,2,2)
            plot(m,B0(3,m),'o')
```

```
        hold all
        m=m+1;

        actualheight = GetServoZDirect();
        height = actualheight+4*10^-6;
        SetServoActive(false);
        SetServoZDirect(height);
        pause(0.4);
        GenNUpdates('cDAQ1Mod8/ao0',0,10,2,[7.5,vv],10);
        SetServoActive(true);
    end
    GenNUpdates('cDAQ1Mod8/ao0',0,10,1000,[0,0],10);
    SetServoSetpoint(spoff);
    actualheight = GetServoZDirect();
    height = actualheight+4*10^-6;
    SetServoActive(false);
    SetServoZDirect(height);
    pause(0.4);
    GenNUpdates('cDAQ1Mod8/ao0',0,10,2,[7.5,0],10);
    SetServoActive(true);
    q=q+1;
  end

end
 GenNUpdates('cDAQ1Mod8/ao0',0,10,1000,[0,0],10);
```

APPENDIX B

LITHOGRAPHY PROGRAM 2

```
load voltagedata.txt
Voltage=voltagedata(:,:);
vv=zeros(290,512);
vv(:,51:447)=Voltage;

linepersec=0.5;
l=397;%in pixels
h=290;%number of lines ,in pixels
bsize=512;
pixelspersec=bsize*2*linepersec;

s=daq.createSession('ni');
AO=addAnalogOutputChannel(s,'cDAQ1Mod8','ao0','voltage');
s.Rate=512;
addTriggerConnection(s,'External','cDAQ1/PFI0','StartTrigger')

for i=1:290
    outputData=vv(i,:)';
    queueOutputData(s,outputData);
    startForeground(s);
end
```

APPENDIX C

CALIBRATION PROGRAM

```
clear all
close all
clc
addpath('C:\Documents and Settings\Administrator\My
Documents\MATLAB\daq')
Rref=2000;   %resistance of the reference resister in olms
RT=24;% ROOM TEMPERATURE
ratio=0.8; %heat conductivity
Ti=550;
Vin=0:0.05:10;
B=zeros(1,201);
Defl=zeros(1,201);
Fric=zeros(1,201);
figure (1)
pause(0.01)
vn=input('please type in the max voltage voltage for the
calibration(160=16V,180=18V,etc)');;
for i=2:vn
GenNUpdates('cDAQ1Mod8/ao0',0,10,8,[Vin(i),Vin(i)],10); % generation
frequency is 2 Hz
A=AcqNUpdates('cDAQ1Mod6/ai0',0,10,50,10000,5);
B(i)=sum(A)/50;
Defl(i)=GetStatusRawDefl();%Defl(i) is the Deflection signal
Fric(i)=GetStatusFriction();% the Friction signal
rr=2000*(Vin(i)-B(i))/B(i);
plot(2*Vin(i),rr,'bo')
hold all
pause(0.01)
end
hold on
for i=2:vn
GenNUpdates('cDAQ1Mod8/ao0',0,10,8,[Vin(vn+2-i),Vin(vn+2-i)],10); %
generation frequency is 2 Hz
A=AcqNUpdates('cDAQ1Mod6/ai0',0,10,50,10000,5);
B2(vn+2-i)=sum(A)/50;
Defl2(vn+2-i)=GetStatusRawDefl();%Defl(i) is the Deflection signal
Fric2(vn+2-i)=GetStatusFriction();% the Friction signal
rr2=2000*(Vin(vn+2-i)-B2(vn+2-i))/B2(vn+2-i);
plot(2*Vin(vn+2-i),rr2,'ro')
hold all
pause(0.01)
end
GenNUpdates('cDAQ1Mod8/ao0',0,10,100,[0,0],10);
Vin=Vin(1:i);
B=B(1:i);
Defl=Defl(1:i);
Fric=Fric(1:i);
V=2.*Vin;     %the total voltage applied to the whole circuit
Vref=2.*B;     %the voltage on the reference resister (2K olms)
Vtip=V-Vref;    %the voltage on the tip
R=Rref*Vtip./Vref;   %the resistance of the tip
I=Vref/Rref;    %the current in the circuit in the unit of A
```

```
Ptip=1000.*I.*Vtip;    %the power dissipated on the tip in mW
figure(2);
subplot(4,1,1)
plot(Defl(1,:));%,axis([0,205,-10,10]);
XLABEL('Time (s)');
YLABEL('Deflection signal(V)');
subplot(4,1,2)
plot(Fric);%,axis([0,205,-10,10]);
XLABEL('time');
YLABEL('Friction signal(V)');
subplot(4,1,3)
plot(Vtip);%,axis([0,205,0,20]);
XLABEL('time');
YLABEL('tip voltage(V)');
subplot(4,1,4)
plot(V);%,axis([0,205,0,20]);
XLABEL('time');
YLABEL('Total voltage(V)');
 Ri=max(R);       %find the maxium value of R
[m n]=find(R==Ri);
Pi=Ptip(n);      %find the value of Ptip corresponding to the climax of R
 figure(3)
subplot(2,2,1)
plot(V,R,'o');%,axis([0,20,0,5000]);
hold on
plot(V(n),Ri,'ro')
XLABEL('total voltage(V)');
YLABEL('tip Resistance(olms)');
subplot(2,2,2)
plot(Ptip,R,'o');%,axis([0,100,0,5000]);
XLABEL('tip power(mW)');
YLABEL('tip Resistance(olms)');
hold on
plot(Pi,Ri,'ro')
hold off
Ri
Ri=input('maxium resistance Ri=');
Pi
Pi=input('tip power cooresponding to the maxium resistance Pi(mW)=');
TH=RT+Ptip*(Ti-RT)/Pi; %tip temperature
Tint=ratio*TH;  %Interface temperature
figure(3)
subplot(2,2,3)
plot(V,TH,'o');%,axis([0,20,0,5000]);
XLABEL('total voltage(V)');
YLABEL('tip temperature(Celcius)');
figure(3)
subplot(2,2,4)
s=1000*round(5*ratio);
plot(V,Tint,'o');%axis([0,20,0,s]);
XLABEL('total voltage(V)');
YLABEL('interface temperature(Celcius)');
figure(4)
plot(V,Defl,'b',V,Defl2,'r')
XLABEL('total voltage(V)');
YLABEL('Deflection');
```

REFERENCES

[1] J. V. Barth, G. Costantini, and K. Kern, Engineering atomic and molecular nanostructures at surfaces. *Nature* **437**, 671-679 (2005).

[2] G. E. Moore, Cramming more components onto integrated circuits. (1965).

[3] Y. Wei and R. L. Brainard, Advanced processes for 193-nm immersion lithography. Bellingham, Washington: SPIE (2009).

[4] W. Chen and H. Ahmed, Fabrication of 5–7 nm wide etched lines in silicon using 100 keV electron-beam lithography and polymethylmethacrylate resist. *Applied physics letters*, **62**, 1499-1501 (1993).

[5] S. Y. Chou, P. R. Krauss, and P. J. Renstrom, Nanoimprint lithography. *Journal of Vacuum Science & Technology B* **14**, 4129-4133 (1996).

[6] S. Sacanna, W. T. M. Irvine, P. M. Chaikin, and D. J. Pine, Lock and key colloids. *Nature*, **464**, 575-578 (2010).

[7] G. Philipp, T. Weimann, P. Hinze, M. Burghard, and J. Weis, Shadow evaporation method for fabrication of sub 10 nm gaps between metal electrodes. *Microelectronic engineering* **46**, 157-160 (1999).

[8] M. Müller, T. Fiedler, R. Gröger, T. Koch, S. Walheim, Ch. Obermair, and T. Schimmel, Controlled structuring of mica surfaces with the tip of an atomic force microscope by mechanically induced local etching. *Surf. Interface Anal*. **36**, 189 (2004).

[9] Y. N. Xia, E. Kim, X. M. Zhao, J. A. Rogers, M. Prentiss, and G. M. Whitesides, Complex optical surfaces formed by replica molding against elastomeric masters. *Science* **273,** 347-349 (1996).

[10] A. Kumar and G. M. Whitesides, Features of gold having micrometer to centimeter dimensions can be formed through a combination of stamping with an elastomeric stamp and an alkanethiol ink followed by chemical etching. *Applied Physics Letters* **63**, 2002 (1993).

[11] E. Kim, Y. N. Xia, and G. M. Whitesides, Polymer microstructures formed by molding in capillaries. *Nature* **376**, 581 (1995).

[12] X. M. Zhao, Y. N. Xia, and G. M. Whitesides, Fabrication of three-dimensional micro-structures: Microtransfer molding. *Advanced Materials* **8**, 837 (1996).

[13] S. Y. Chou, P. R. Krauss, and P. J. Renstrom, Imprint of sub-25 nm vias and trenches in polymers. *Applied Physics Letters* **67**, 3114 (1995).

[14] E. Kim, Y. N. Xia, X. M. Zhao, and G. M. Whitesides, Solvent-assisted microcontact molding: A convenient method for fabricating three-dimensional structures on surfaces of polymers. *Advanced Materials* **9**, 651 (1997).

[15] D. Y. Petrovykh, F. J. Himpsel, and T. Jung, Width distribution of nanowires grown by step decoration. *Surface science* **407**, 189-199 (1998).

[16] T. Jung, R. Schlittler, J. K. Gimzewski, and F. J. Himpsel, One-dimensional metal structures at decorated steps. *Applied Physics A* **61**, 467-474 (1995).

[17] J. H. Chung, G. Bai, and W. H. Yeo, Shadow edge lithography for nanoscale patterning and manufacturing, U.S. Patent (2009).

[18] J. Aizenberg, A. J. Black, and G. M. Whitesides, Controlling local disorder in self-assembled monolayers by patterning the topography of their metallic supports. *Nature* **394**, 868-871 (1998).

[19] J. C. Love, K. E. Paul, and G. M. Whitesides, Fabrication of Nanometer-Scale Features by Controlled Isotropic Wet Chemical Etching. *Advanced Material* **13**, 604-607 (2001).

[20] J. A. Rogers, K. E. Paul, R. J. Jackman, and G. M. Whitesides. Using an elastomeric phase mask for sub-100 nm photolithography in the optical near field. *Applied Physics Letters* **70**, 2658-2660 (1997).

[21] M. P. Zach, K. H. Ng, and R. M. Penner, Molybdenum nanowires by electrodeposition. *Science* **290**, 2120-2123 (2000).

[22] A. Ulman, An Introduction to Ultrathin Organic Films: From Langmuir-Blodgett to Self-Assembly. Academic press (2013).

[23] G. Binnig, H. Rohrer, C. Gerber, and E. Weibel, Tunneling through a controllable vacuum gap. *Applied Physics Letters* **40**, 178 (1982).

[24] G. Binnig, C. F. Quate, and C. Gerber, Atomic force microscope. *Physical Review Letters* **56**, 930 (1986).

[25] O. C. Wells, Method and apparatus for low-energy scanning electron beam lithography, U.S. Patent (1988).

[26] J. Červenka, R. Kalousek, M. Bartošík, D. Škoda, O. Tomanec, and T. Šikola, Fabrication of nanostructures on Si (100) and GaAs (100) by local anodic oxidation. *Applied Surface Science* **253**, 2373-2378 (2006).

[27] S. Masubuchi, M. Ono, K. Yoshida, K. Hirakawa, and T. Machida, Fabrication of graphene nanoribbon by local anodic oxidation lithography using atomic force microscope, *Applied Physics Letters* **94**, 082107 (2009).

[28] R. Held, T. Heinzel, P. Studerus, and K Ensslin, Nanolithography by local anodic oxidation of metal films using an atomic force microscope. *Physica E: Low-dimensional Systems and Nanostructures* **2**, 748-752 (1998).

[29] Y. Yan, Z. Hu, X. Zhao, T. Sun, S. Dong, and X. Li, Top-Down Nanomechanical Machining of Three-Dimensional Nanostructures by Atomic Force Microscopy. *Small* **6**, 724-728 (2010).

[30] R. D. Piner, J. Zhu, F. Xu, S. Hong S, and C. A. Mirkin, "Dip-pen" nanolithography. *Science* **283**, 661-663 (1999).

[31] J. H. Lim, D. S. Ginger, K. B. Lee, J. Heo, J. M. Nam, and C. A. Mirkin, *Angew. Chem. Int. Ed.* **42**, 2309-2312 (2003).

[32] A. Noy, A. E. Miller, J. E. Klare, B. L. Weeks, B. W. Woods, and J. J. De Yoreo, Fabrication of luminescent nanostructures and polymer nanowires using dip-pen nanolithography. *Nano Lett.* **2**, 109-112 (2002).

[33] L. M. Demers, D. S. Ginger, S. J. Park, Z. Li, S. W. Chung, and C. A. Mirkin, Direct patterning of modified oligonucleotides on metals and insulators by dip-pen nanolithography. *Science* **296**, 1836-1838 (2002).

[34] Y. Li, B. W. Maynor, J. Liu, Electrochemical AFM "dip-pen" nanolithography. *J. Am. Chem. Soc.* **123**, 2105-2106 (2001).

[35] M. B. Ali, T. Ondarçuhu, M. Brust, and C. Joachim, Atomic Force Microscope Tip Nanoprinting of Gold Nanoclusters. *Langmuir* **18**, 872 (2002).

[36] C. A. Mirkin, S. Hong, and L. Demers. Dip-Pen Nanolithography: Controlling Surface Architecture on the Sub-100 Nanometer Length Scale. *ChemPhysChem* **2**, 37-39 (2001).

[37] C. R. K. Marrian, F. K. Perkins, S. L. Brandow, T. S. Koloski, E. A. Dobisz, and J. M. Calvert, Low voltage electron beam lithography in self-assembled ultrathin films with the scanning tunneling microscope. *Applied physics letters* **64**, 390-392 (1994).

[38] B. Cappella, H. Sturm, and S. Weidner, Breaking polymer chains by dynamic plowing lithography. *J Appl. Phys*. **91**, 506 (2002).

[39] T. A. Jung, A. Moser, H. J. Hug, D. Brodbeck, R. Hofer, H. R. Hidber, and U. D. Schwarz, The atomic force microscope used as a powerful tool for machining surfaces. *Ultramicroscopy* **1446** 42–44 (1992).

[40] T. H. Fang and W. J. Chang, Sensitivity Analysis of a Cracked Atomic Force Microscope Cantilever. *J. Phys. Chem. Solids* **64**, 913 (2003).

[41] C. K. Hyon, S. C. Choi, S. W. Hwang, D. Ahn, Y. Kim, and E. K. Kim, Selective Positioning of InAs Quantum Dots on a GaAs Substrate Directly Patterned by Using an Atomic Force Microscope. *Appl. Phys. Lett.* **75**, 292 (1999).

[42] S. Hong and C. A. Mirkin, A nanoplotter with both parallel and serial writing capabilities. *Science* **288**, 1808-1811 (2000).

[43] M. Zhang, D. Bullen, S. W. Chung, S. Hong, K. S. Ryu, Z. F. Fan, C. A. Mirkin, and C. Liu, A MEMS nanoplotter with high-density parallel dip-pen manolithography probe arrays. *Nanotechnology* **13**, 212 (2002).

[44] C. C. Williams and H. K. Wickramasinghe, Scanning thermal profiler. *Applied Physics Letters* **49**, 1587-1589 (1986).

[45] M. H. Li and Y. B. Gianchandani, Microcalorimetry applications of a surface micromachined bolometer-type thermal probe. *Journal of Vacuum Science & Technology B* **18**, 3600-3603 (2000).

[46] H. J. Mamin, B. D. Terris, L. S. Fan, S. Hoen, R. C. Barrett, and D. Rugar, High-density data storage using proximal probe techniques. *IBM Journal of Research and Development* **39**, 681 (1995).

[47] H. J. Mamin and D. Rugar, Thermomechanical writing with an atomic force microscope tip. *Applied Physics Letters* **61**, 1003–1005 (1992).

[48] B. W. Chui, T. D. Stowe, T. W. Kenny, H. J. Mamin, B. D. Terris, and D. Rugar, Low-stiffness silicon cantilevers for thermal writing and piezoresistive readback with the atomic force microscope. *Applied Physics Letters* **69**, 2767-2769 (1996).

[49] P. Vettiger, G. Cross, M. Despont, U. Drechsler, U. Drig, B. Gotsmann, W. Hberle, M. A. Lantz, H. E. Rothuizen, R. Stutz, and G. K. Binnig, The millipede-nanotechnology entering data storage. *Nanotechnology* **1**, 39-55 (2002).

[50] M. Despont, U. Drechsler, R. Yu, H. B. Pogge, and P. Vettiger, Wafer-scale microdevice transfer interconnect: Its application in an AFM-based data-storage system. *Journal of Microelectromechanical Systems* **13**, 895 (2004).

[51] A. Pantazi, A. Sebastian, T. A. Antonakopoulos, P. Baechtold, A. R. Bonaccio, J. Bonan, G. Cherubini, M. Despont, R. A. DiPietro, U. Drechsler, U. Duerig, B. Gotsmann,

W. Haeberle, C. Hagleitner, J. L. Hedrick, D. Jubin, A. Knoll,M. A. Lantz, J. Pentaralkis, H. Pozidis, R. C. Pratt, H. Rothuizen, R. Stutz,M. Varsamou, D. Wiesmann, and E. Eleftheriou, Probe-based ultrahighdensitystorage technology. *IBM Journal of Research and Development* **52**,493 (2008).

[52] M. Y. Han, B. Ozyilmaz, Y. B. Zhang, and P. Kim, Energy Band-Gap Engineering of Graphene Nanoribbons. *Phys. Rev. Lett*. **98**, 206805 (2007).

[53] J. W. Bai, X. F. Duan, and Y. Huang, Rational Fabrication of Graphene Nanoribbons Using a Nanowire Etch Mask. *Nano Lett*. **9**, 2083–2087 (2009).

[54] X. L. Li, X. R. Wang, L. Zhang, S. W. Lee, and H. J. Dai, Chemically Derived, Ultrasmooth Graphene Nanoribbon Semiconductors. *Science* **319**, 1229–1232 (2008).

[55] D. V. Kosynkin, A. L. Higginbotham, A. Sinitskii, J. R. Lomeda, A. Dimiev, B. K. Price, and J. M. Tour, Longitudinal Unzipping of Carbon Nanotubes to Form Graphene Nanoribbons. *Nature* **458**, 872–877 (2009).

[56] S. Ryu, J. Maultzsch, M. Y. Han, P. Kim, and L. E. Brus, Raman Spectroscopy of Lithographically Patterned Graphene Nanoribbons. *ACS Nano* **5**, 4123–4130 (2011).

[57] H. W. Kroto, J. R. Heath, S. C. O'Brien, R. F. Curl, and R. E. Smalley C_{60}: Buckminsterfullerene. *Nature* **318**:162-1633 (1985).

[58] C. Berger, Z. Song, T. Li , X. Li , A. Y. Ogbazghi , R. Feng , Z. Dai, A. N. Marchenkov , E. H. Conrad , P. N. First, and W. A. de Heer. Ultrathin epitaxial graphite: 2D electron gas properties and a route toward graphene-based nanoelectronics. *J. Phys. Chem. B* **108**, 19912–19916 (2004).

[59] K. S. Novoselov, A. K. Geim, S. V. Morozov, D. Jiang, Y. Zhang, S. V. Dubonos, I. V. Grigorieva, and A. A. Firsov, Electric field effect in atomically thin carbon films. *Science* **306**, 666-669 (2004).

[60] S. Y. Zhou, G. H. Gweon, A. V. Fedorov, P. N. First, W. A. de Heer, D. H. Lee1, F. Guinea, A. H. Castro Neto, and A. Lanzara, Substrate-induced band gap opening in epitaxial graphene. *Nature materials* **6**, 770-775 (2007).

[61] Z. Guo, R. Dong, P. S. Chakraborty, Nelson Lourenco, James Palmer, Y. Hu, Ming Ruan, John Hankinson, Jan Kunc, John D. Cressler, Claire Berger, and Walt A. de Heer, Record maximum oscillation frequency in C-face epitaxial graphene transistors. *Nano letters* **13**, 942-947 (2013).

[62] K. I. Bolotin, K. J. Sikes, Z. Jiang, M. Klima, G. Fudenberg, J. Hone, P. Kim, H. L. Stormer, Ultrahigh electron mobility in suspended graphene. *Solid State Communications* **146**, 351-355 (2008).

[63] W. S. Hummers and R. E. Offeman, Preparation of graphite oxide. *J. Am. Chem. Soc.* **80**, 1339 (1958).

[64] Z. Liu, Q. Liu, Y. Huang, Y. Ma, S. Yin, X. Zhang, W. Sun, and Y. Chen, Organic photovoltaic devices based on a novel acceptor material: graphene. *Advanced Materials* **20**, 3924-3930 (2008).

[65] J. T. Robinson, J. S. Burgess, C. E. Junkermeier, S. C. Badescu, T. L. Reinecke, F. K. Perkins, M. K. Zalalutdniov, J. W. Baldwin, J. C. Culbertson, P. E. Sheehan, and E. S. Snow, Properties of fluorinated graphene films. *Nano letters* **10**, 3001-3005 (2010).

[66] A. J. Van Bommel, J. E. Crombeen, and A. Van Tooren, LEED and Auger electron observations of the SiC(0001) surface. *Surface Science* **48,** 463-472 (1975).

[67] Y. Hu, M. Ruan, Z. Guo, R. Dong, J. Palmer, J. Hankinson, C. Berger, and W. A. de Heer, Structured epitaxial graphene: growth and properties. *Journal of Physics D: Applied Physics* **45**, 154010 (2012).

[68] Y. Shen, S. B. Yang, P. Zhou, Q. Q. Sun, P. F. Wang, L. Wan, J. Li, L. Y. Chen, X. B. Wang, S. J. Ding, and D. W. Zhang, Evolution of the band-gap and optical properties of graphene oxide with controllable reduction level. *Carbon* **62**, 157–164 (2013).

[69] Z. Wei, D. Wang, S. Kim, S.-Y. Kim, Y. Hu, M. K. Yakes, A. R. Laracuente, Z. Dai, S. R. Marder, C. Berger, W. P. King, W. A. de Heer, P. E. Sheehan1, and E. Riedo. Nanoscale Tunable Reduction of Graphene Oxide for Graphene Electronics. *Science* **328**, 1373–1376 (2000).

[70] K. Zhang, Q. Fu, N. Pan, X. Yu, J. Liu, Y. Luo, X. Wang, J. Yang, and J. Hou, Direct writing of electronic devices on graphene oxide by catalytic scanning probe lithography. *Nature communications* **3**, 1194 (2012).

[71] K. M. Carroll, X. Lu, S. Kim, Y. Gao, H.-J. Kim, S. Somnath, L. Polloni, R. Sordan, W. P. King, J. E. Curtis, and E. Riedo, Parallelization of thermochemical nanolithography. *Nanoscale* **6**, 1299-1304 (2014).

[72] W.-K .Lee, J. T. Robinson, D. Gunlycke, R. R. Stine, C. R. Tamanaha, W. P. King, and P. E. Sheehan, Chemically Isolated Graphene Nanoribbons Reversibly Formed in Fluorographene Using Polymer Nanowire Masks. *Nano Lett* **11**, 5461–5464 (2011).

[73] J. H. Burroughes, D. D. C. Bradley, A. R. Brown, R. N. Marks, K. Mackay, R. H. Friend, P. L. Burns, and A. B. Holmes, Light-emitting-diodes based on conjugated polymers. *Nature* **347**, 539-541 (1990).

[74] A. Smekal, Zur Quantentheorie der Dispersion. *Naturwissenschaften* **11**, 873–875 (1923).

[75] C. V. Raman and K. S. Krishnan, A new type of secondary radiation. *Nature* **121**, 501-502 (1928).

[76] J. Zhao and K. Uosaki, Dielectric properties of organic monolayers directly bonded on silicon probed by current sensing atomic force microscope. *Applied physics letters* **83**, 2034-2036 (2003).

[77] M. Nonnenmacher, M. P. O'Boyle, and H. K. Wickramasinghe, Kelvin probe force microscopy. *Applied physics letters* **58**, 2921-2923 (1991).

[78] B. Bhushan and A. V. Goldade, Measurements and analysis of surface potential change during wear of single-crystal silicon (100) at ultralow loads using Kelvin probe microscopy. *Applied surface science* **157**, 373-381 (2000).

[79] G. Koley and M. G. Spencer, Surface potential measurements on GaN and AlGaN/GaN heterostructures by scanning Kelvin probe microscopy. *Journal of Applied Physics* **90**, 337-344 (2001).

[80] D. Wang, S. Kim, W. D. Underwood, A. J. Giordano, C. L. Henderson, Z. Dai, W. P. King, S. R. Marder, and E. Riedo, Direct writing and characterization of poly (p-phenylene vinylene) nanostructures. *Applied Physics Letters* **95**, 233108 (2009).

[81] D. Wang, V. K. Kodali, W. D. Underwood II, J. E. Jarvholm, T. Okada, S. C. Jones, M. Rumi, Z. Dai, W. P. King, S. R. Marder, J. E. Curtis, and E. Riedo, Thermochemical Nanolithography of Multifunctional Nanotemplates for Assembling Nano-Objects. *Advanced functional materials* **19**, 3696-3702 (2009).

[82] R. Szoszkiewicz, T. Okada, S. C. Jones, T. Li, W. P. King, S. R. Marder, and E. Riedo, High-speed, sub-15 nm feature size thermochemical nanolithography. *Nano letters* **7**, 1064-1069 (2007).

[83] D. Wang, R. Szoszkiewicz, M. Lucas, E. Riedo, T. Okada, S. C. Jones, S. R. Marder, J. Lee, and W. P. King, Local wettability modification by thermochemical nanolithography with write-read-overwrite capability. *Applied Physics Letters* **91**, 243104 (2007).

[84] K. M. Carroll, A. J. Giordano, D. Wang, V. K. Kodali, J. Scrimgeour, W. P. King, S. R. Marder, E. Riedo, and J. E. Curtis, Fabricating Nanoscale Chemical Gradients with ThermoChemical NanoLithography. *Langmuir* **29**, 8675-8682 (2013).

[85] H. J. Kim, Z. Dai, and W. P. King, Thermal crosstalk in heated microcantilever arrays. *J. Micromech. and Microeng.* **23**, 025001 (2013).

[86] B. A. Nelson and W. P. King, Modeling and Simulation of the Interface Temperature Between a Heated Silicon Tip and a Substrate. *Nanoscale and Microscale Thermophysical Engineering* **12**, 98–115 (2008).

[87] B. W. Chui, M. Asheghi, Y. S. Ju, K. E. Goodson, T. W. Kenny, and H. J. Mamin, Intrinsic-carrier thermal runaway in silicon microcantilevers. *Microscale Thermophysical Engineering* **3**, 217 (1999).

[88] B. H. Stuart. Infrared spectroscopy: Fundamentals and Applications. John Wiley & Sons, Inc., 2005.

[89] M. R. Abel, T. L. Wright, W. P. King, and S. Graham, Thermal metrology of silicon microstructures using Raman spectroscopy. *IEEE Transactions on Components and Packaging Technologies* **30**, 200 (2007).

[90] D. Wang. Thermochemical nanolithography fabrication and atomic microscopy characterization of functional nanostructures. Ph.D. thesis (2010).

[91] B. Bhushan and H. Fuchs, Applied Scanning Probe Methods IV: Industrial Applications (Springer, Berlin, 2006).

[92] G. Chen, Phonon heat conduction in nanostructures. *International Journal of Thermal Sciences* **39**, 471 (2000).

[93] C. Hu, M. Kiene, and P. S. Ho, Thermal conductivity and interfacial thermal resistance of polymeric low k films, *Applied Physics Letters* **79**, 4121 (2001).

[94] M. M. Yovanovich, J. R. Culham, and P. Teertstra, Analytical modeling of spreading resistance in flux tubes, half spaces, and compound disks, *IEEE Transactions on Components Packaging and Manufacturing Technology Part A* **21**, 168 (1998).

[95] M. Levinshtein, S. Rumyantsev, and M. Shur, Properties of Advanced Semiconductor Materials GaN, AlN, SiC, BN, SiC, SiGe (John Wiley & Sons, New York, 2001).

[96] A. J. Bullen, K. E. O'Hara, D. G. Cahill, O. Monteiro, and A. von Keudell, Thermal conductivity of amorphous carbon thin films, *Journal of Applied Physics* **88**, 6317 (2000).

[97] A. Laraoui, H. Aycock-Rizzo, Y. Gao, X. Lu, E. Riedo, and C. A. Meriles, Imaging thermal conductivity with nanoscale resolution using a scanning spin probe. *Nature Communications* **6**, 8954 (2015).

[98] M. Seong, S. Somnath, H. J. Kima, and W.P. King, Parallel nanoimaging using an array of 30 heated microcantilevers. *RSC Adv.* **4**, 24747-24754 (2014).

[99] M. W. Doherty, N. B. Manson, P. Delaney, F. Jelezko, J. Wrachtrup, L. C. L. Hollenberg, The nitrogen-vacancy colour centre in diamond. *Phys. Rep.* **528**, 1–45 (2013).

[100] V. M. Acosta, E. Bauch, M. P. Ledbetter, A. Waxman, L.-S. Bouchard, and D.

Budker, Temperature dependence of the nitrogen-vacancy magnetic resonance in diamond. *Phys. Rev. Lett.* **104**, 070801 (2010).

[101] D. M. Toyli, C. F. de las Casasa, D. J. Christlea, V. V. Dobrovitskib, and D. D. Awschaloma, Fluorescence thermometry enhanced by coherence of single spins in diamond. *Proc. Natl Acad. Sci.* **110**, 8417–8421 (2013).

[102] D. M. Toyli, D. J. Christle, A. Alkauskas, B. B. Buckley, C. G. Van de Walle, and D. D. Awschalom. Measurement and control of single nitrogen-vacancy center spins above 600 K. *Phys. Rev. X* **2**, 031001 (2012).

[103] B. Bhushan and H. Fuchs, Applied Scanning Probe Methods IV: Industrial Applications (Springer, Berlin, 2006).